ANALYSIS OF CRUST AND MANTLE STRUCTURE ACROSS TURKEY USING PASSIVE SEISMIC DATA

A THESIS SUBMITTED TO
THE GRADUATE SCHOOL OF NATURAL AND APPLIED SCIENCES
OF
MIDDLE EAST TECHNICAL UNIVERSITY

BY

BIZHAN ABGARMI

IN PARTIAL FULFILLMENT OF THE REQUIREMENTS
FOR
THE DEGREE OF DOCTOR OF PHILOSOPHY
IN
GEOLOGICAL ENGINEERING

JANUARY 2019

Approval of the thesis:

ANALYSIS OF CRUST AND MANTLE STRUCTURE ACROSS TURKEY USING PASSIVE SEISMIC DATA

Submitted by **BIZHAN ABGARMI** in partial fulfillment of the requirements for the degree of **Doctor of Philosophy in geological Engineering Department, Middle East Technical University** by,

Prof. Dr. Halil Kalipcilar
Dean, Graduate School of **Natural and Applied Sciences** _____

Prof. Dr. Erdin Bozkurt
Head of Department, **Geological Engineering** _____

Assist. Prof. Dr. A. Arda Özacar
Supervisor, **Geological Engineering Dept., METU** _____

Examining Committee Members:

Prof. Dr. Nuretdin Kaymakçı
Geological Engineering Dept., METU _____

Assist. Prof. Dr. A. Arda Özacar
Geological Engineering Dept., METU _____

Prof. Dr. Bora Rojay
Geological Engineering Dept., METU _____

Assoc. Prof. Dr. Erman Özsayın
Geological Engineering Dept., Hacettepe Universıty. _____

Assist. Prof. Dr. Tuna Eken
Geophysical Engineering Dept., İstanbul Technical Uni. _____

Date: ----------

I hereby declare that all information in this document has been obtained and presented in accordance with academic rules and ethical conduct. I also declare that, as required by these rules and conduct, I have fully cited and referenced all material and results that are not original to this work.

Name, Last name: Bizhan Abgarmi

Signature :

ABSTRACT

ANALYSIS OF CRUST AND MANTLE STRUCTURE ACROSS TURKEY USING PASSIVE SEISMIC DATA

Abgarmi, Bizhan
Ph.D., Department of Geological engineering
Supervisor: Assist. Prof. Dr. A. Arda Özacar

January 2019, 121 pages

Anatolia is one of the most tectonically active regions in the world which is amalgamation of different terranes and structures. This region has a complextectonic evolution which includes various stages of subduction and collision. This complexity demands more detailed observations of the crust and upper mantle to generate a comprehensive geodynamic model. However, the knowledge related to crust and mantle structure beneath Anatolia is still very limited so the fates of the structures in deeper interiors are enigmatic. During the last decade, the number of broadband seismic stations operating in Turkey has been expanded significantly which provides a unique opportunity to analyze the crust and mantle in detail. Recently, additional temporary broadband stations are deployed with our collaboration across central Turkey in the scope of an international project funded by National Science Foundation (NSF). In this study, we analyzed the broadband seismic data recorded during earthquakes by national networks and recently deployed temporary stations including the CAT and also the NAF experiments. Our aim is to image the inner structure of crust and upper mantle, detect thicknesses of the crust and analyze the multi-layered seismic anisotropy along crust and upper mantle. At the end, our results are interpreted and modeled along with previous geological and geophysical

data to identify the factors controlling the tectonic settings and test plausible geodynamic models.

Keywords: Anatolia, Receiver Function, ShearWave Splitting.

ÖZ

PASİF SİSMİK VERİLER KULLANILARAK TÜRKİYE BOYUNCA YERKABUĞU VE MANTONUN ANALİZİ

Abgarmi,Bizhan
Doktora, Jeoloji Mühendisliği
Tez Yöneticisi:Ydoç. Prof. Dr. A.Arda Özacar

Ocak 2019, 121 sayfa

Anadolu, farklı blokların ve yapıların birleşmesinden meydana gelen dünyanın tektonik olarak en aktif bölgelerden biridir. Bölge farklı dalma ve çarpışma aşamaları içeren karmaşık bir tektonik evrime sahiptir. Bu karmaşıklık, kapsamlı bir jeodinamik model oluşturmak için kabuk ve üst mantoda daha ayrıntılı gözlemler yapılmasını gerektirir. Ancak, Anadolu'nun altındaki kabuk ve manto yapısıyla ilgili bilgi halen çok sınırlıdır ve bu nedenle yapıların daha derin iç kısımlarındaki kaderi gizemini korumaktadır. Son on yılda, Türkiye'de faaliyet gösteren geniş bantlı sismik istasyonların sayısı önemli ölçüde genişlemiştir ki bu da kabuk ve mantoyu detaylı bir şekilde analiz etmek için eşsiz bir fırsat sunmaktadır. Yakın zamanda, Ulusal Bilim Vakfı (NSF) tarafından finanse edilen uluslararası bir proje kapsamında, Türkiye genelindeki işbirliğimizle ek geçici geniş bant istasyonları konuşlandırılmıştır. Bu çalışmada, ulusal ağlar ve yakın zamanlarda CAT ve NAF deneyleri kapsamında kurulan geçici istasyonlar tarafından kaydedilen geniş bant sismik deprem verileri kullanılmıştır. Amacımız, kabuk ve üst mantonun iç yapısını görüntülemek, kabuki kalınlıklarını belirlemek ve kabuk ve üst manto boyunca çok katmanlı sismik anizotropi analizi gerçekleştirmektir. Sonunda, elde edilen sonuçlar, tektonik ortamları kontrol eden faktörleri tanımlamak ve uygun jeodinamik modelleri test etmek için önceki jeolojik ve jeofiziksel verilerle birlikte yorumlanmakta ve modellenmektedir.

Anahtar Kelimeler: Anadolu, Alıcı Fonksiyon, Kesme Dalga Ayrımlanması

To My Family

ACKNOWLEDGMENTS

The author wishes to express his deepest gratitude to his supervisor Assist. Prof. Dr. Atilla Arda Özacar for his guidance, advice, criticism, encouragements and insight throughout the research.

The author would also like to thank Jonathan Robert Delph, Susan L. Beck, George Zandt and Colton Lynnfor their suggestions and comments.

Also Eric Sandvol, Niyazi Turkelli and Cemal Berk Biryol are gratefully acknowledged. Additionally, the author would like to express his very great appreciation to Mickael Bonnin for providing the data used in tests and validation process.

This work is partially funded by Scientific and Technological Research Council of Turkey (TUBİTAK) under grant number 111Y239 and also by National Science Foundationof America (NSF) under award numbers EAR-1109762 and EAR-1109336.

TABLE OF CONTENTS

ABSTRACT v
ÖZ vii
ACKNOWLEDGMENTS x
TABLE OF CONTENTS xi
LIST OF TABLES xiii
LIST OF FIGURES xiv
INTRODUCTION 1
1-1- Purpose and Scope 1
1-2- Data 4
1-2-1- The CD-CAT experiment 5
1-2-2- The NAF experiment 7
1-3- Methodology 8
1-3-1- Receiver function 8
1-3-2- Shear wave splitting 20
1-4- Organization of thesis 25
2-1- Introduction 28
2-2- The Amalgamation of Anatolia 30
2-3- Tectonic Structures of the Anatolian Plate 32
2-4- Data and Methods 37
2-4-1- Calculation for Crustal Thickness and *Vp/Vs*: Stack Windowing Analysis 39
2-4-2- Adaptive Common Conversion Point (CCP) Stacking 42
2-5- Results 43
2-6- Discussion 47
2-6-1- Nature of Crustal Boundaries in the central Anatolia 47
2-6-2- Low Velocity Zones in the Central Anatolian Volcanic Province 48
2-6-3- Uplift of the Central Taurus Mountains 49
2-7- Conclusion 52

3-1- Introduction 56
3-2- Data and Methods 59
3-2-1- Calculation of crustal thickness and Vp/Vs ratio 61
3-3- Results 65
3-4- Discussion 69
3-5- Conclusion 73
4-1- Introduction 76
4-2- Methodology 77
4-3- Program modules 81
4-3-1- Data Conversion 82
4-3-2- Grid Search 85
4-3-3- Sensitivity analysis 88
4-4- Synthetic test 90
4-5- Analysis of Real Data 92
4-6- Conclusion 94
4-7- Data and resources 95
DISCUSSION 97
REFERRENCES 103
CURRICULUM VITAE 118

LIST OF TABLES

TABLES

Table 4-1: Input and output model parameters extracted using different misfit calculation procedures and signal to noise ratios (SNR) 91

LIST OF FIGURES

FIGURES

figure 1-1 General tectonic settings of the Anatolian plate and surrounding neighbors. 2

Figure 1-2: Distribution of seismic stations along Turkey. 5

Figure 1-3: The relation between no net rotation absolute plate motion and fast polarization direction resulted from shear wave splitting analysis.. 7

Figure 1-4: Principals of teleseismic P wave receiver function. A) exhibits the importance of using the teleseismic events to have the incidence angles close to vertical. B) conversion of the incident P wave at the interface with impedance contrast. C) the necessity of full backazimuthal coverage to sample underneath the station from all sides and detect possible variation/anisotropy and D) response of the receiver function analysis to a sharp, transitional boundary and low velocity zone. 9

Figure 1-5: Different phases in receiver function analysis. Ps is the main receiver function and PpPs nnd PsPs+PpSs are the first and second reverberations respectively. The principal of the H-K stacking method in which at one definite depth with definite Vp/Vs ratio all three phases intersect at a single point. 13

Figure 1-6: Stack Windowing Analysis (SWA), blue lines represent all the traces put togeather, red line is the average of all traces and yellow lines are average (red line) plus and minus standar deviation.. 16

Figure 1-7: Interactive phase picking CCP stacking. black stars represent the picked depth for the Ps (above) or PpPs (below) phases. 19

Figure 1-8: Basics of shear wave splitting which shows how an incident shear wave splits into two slow and fast phases due to propagation through an anisotropic medium. 21

Figure 1-9: Left, schematic configuration of two layered anisotropy in upper mantle and crust. relation of the fast polarization direction with the mantle flow and

absolute plate motion in upper mantle and paleo stress in the crust. Right, the variation of the apparent anisotropic parameters with respect to backazimuth . 22
Figure 2-1:Tectonic map of Turkey and near vicinity showing active faults, terranes/blocks and bounding sutures (after Okay & Tuysuz 1999). 29
Figure 2-2: The topographic map of the study area showing key tectonic features (young volcanism, faults and suture zones) along with the location of seismic stations used in this study. 34
Figure 2-3: Global distribution of events used in our receiver function analysis. 38
Figure 2-4: Comparison between H-K stacking analysis and stack windowing analysis (SWA) for two stations.. 41
Figure 2-5: Results of stack windowing analysis for (A) crustal thickness and, (B) bulk crustal Vp/Vs. 43
Figure 2-6: Negative receiver function amplitudes between 10 and 30 km below surface normalized to coherence peak from CCP stacking. 45
Figure 2-7: (A-E): CCP stacks throughout central anatolia with 150% vertical exaggeration and location map of these sections (on the right). 46
Figure 2-8: CCP stack cutting through Taurus Mountains and CAVP (Transect F-F' shown in the location map of Figure 2-7) and its interpreted section. 52
Figure 3-1: A) Terrane map showing major sutures and faults modified from Okay Et Al. (1994). Location of seismic stations are shown by inverted triangles B) Pre-Black sea basin opening tectonic structure restoration of Nikishin et al. (2015). 58
Figure 3-2: Tectonic map of the study area showing major faults, sutures, terranes and neogene volcanism along with used broadband seismic stations 60
Figure 3-3: A) The azimuthal distribution of the earthquakes used in this study.. 62
Figure 3-4: Moho depth and Vp/Vs maps calculated by CCP bin picking and H-K stacking. 66
Figure 3-5: CCP cross sections of binned p teleseismic receiver functions plotted below 3D surface topography. 68
Figure 4-1: Workflow of the M-Split program 82
Figure 4-2: A) program start window and B) data conversion interface 84

Figure 4-3: Misfit calculation interface,.....86
Figure 4-4: Results interface that also provides options for sensitivity analysis and model comparison modules.....87
Figure 4-5: A) Interface to compare various models with different splitting parameters and also different dominant frequencies B) resultant model plots of splitting parameters as a function of backazimuth along with observations.....88
Figure 4-6: Sensitivity analysis interface which generates scatter and contour plots of best solutions in model space using the selecte parameter vaues 89
Figure 4-7: Unweighted synthetic test for noisy data with signal to noise ratios (SNR) of A) 5, B) 10 and C) 20.....91
Figure 4-8: A) Multilayered anisotropy models obtained for station BKS using weighted approach B) resultant model plots of splitting parameters as a function of backazimuth along with observations. 93
Figure 4-9: Contour plots of model space for both fast polarization directions (A and C) and delay times (B and D) based on two different calculated parameters using weighted approach for the splitting observations of station BKS. 94
Figure 5-1: The general diagram of major strike slip fault zones along the study area. A) Lithospheric scale fault zones with offset in moho and B) Crustal scale fault zones with offset in mid crustal features. 98

CHAPTER 1

INTRODUCTION

1-1- Purpose and Scope

The complex geological settings with unique ongoing processes, make Turkey one of the most attractive regions by scientists with various backgrounds. The vast veriety of studies are conducted which are all aimed to disclose the complex tectonic evolution of this region. The interaction of the Anatolian plate with the surrounding plates show significant variety through time and space as the past deformation before Miocene converted to continental collision to the east and slab retreat to the west (Şengör et al. 1985; Reilinger et al. 2006). Thus, the initiation of the tectonic escape causing westward extruding Anatolian plate and the role of the surrounding plates (and their remnants) are still under much debate. In other words the driving force of this process is not clearly known and needs to be studied in more details.

This spatial variation from east to west also creates a transition zone which changes from compressional regime in the east to extensional in the west. This tiny plate has withnessed several sequences of opening and closure of oceans with subsequent subduction and collision events which make this plate a complex amalgamation of different terranes. The occurrence of Central Anatolian Volcanic Province (CAVP), rapid uplift in southern Turkey (Cosentino et al. 2012; Schildgen et al. 2014; Radeff et al. 2015) and localization of strain in Central Anatolia, existence of very low basin elevations in southeast are examples of the phenomena which are yet to be clarified. Adding to these, existence of an anomalously hot asthenosphere underneath the

Anatolian plateau (e.g. Gök et al. 2003; Piromallo & Morelli 2003; Al-Lazki et al. 2004) is another observed regional phenomenon which requires attention.

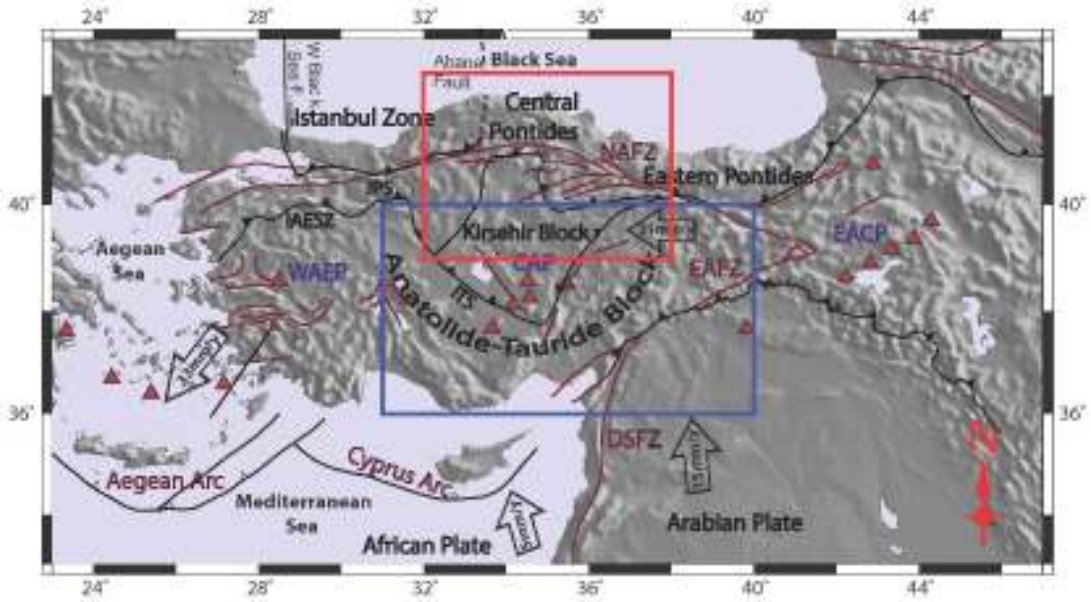

Figure 1-1 General tectonic settings of the Anatolian plate and surrounding neighbors. The Blue rectangle represents the CAT experiment region and the red rectangle represents the NAF experiment zone.

To shed light on the processes which are responsible in formation of these phenomenas, global seismology plays a key role. One major step in understanding these deep processes is to image the current configuration of the concealed subsurface structures. To achieve this, receiver function analysis can be considered as a suitable methodology since it is sensitive to seismic changes at the discontinuities that are formed or deformed in relation with the controlling tectonic

processes. To elucidate the crustal structure of the Anatolian plate, receiver function analysis conducted in two different regions which are in fact the missing pieces to create a general image of crustal structure of the entire Anatolian plate. These regions are South Central Anatolia and North Central Anatolia across the curved segment of the North Anatolian Fault Zone (Figure 1.1).

South Central Anatolia has experienced several sequences of deformation which shaped the current morphologic image of this region. High-rise mountains to the south which terminates to the southwest and converts to a very low elevation basin and numerous surface expressions of different sequences of volcanic activities, existence of severl fault zones and sutures are of these features. According to previous studies, both East Anatolian Fault Zone (EAFZ) forming the plate boundary between Anatolian and Arabian plates and Central Anatolian Fault Zone (CAFZ) are lithospheric scale structures (Ates et al., 1999; Gans et al., 2009; Mutlu and Karabulut, 2011). The mentioned phenomenas alltogether indicate a very complex deformation sequence which still is under much debate.

On the other hand, North Central Anatolia contains the central segment of the world-famous transform plate boundary, the North Anatolian Fault Zone (NAFZ). Although the surface evidences of this fault zone are well known, the knowledge about the subsurface structure of this major plate boundary is very limited. This fault zone, in some regions, displays a good correlation with older suture zones (Şengör and Yılmaz, 1981) and geophysical properties change sharply in either side of the fault (Pn and Sn velocities; Gok et al. 2000, Sandvol et al. 2012, Bouguer gravity anomalies; Al-Lazki et al. 2002). At this point, the source of these changes observed on lithospheric scale can be associated to both NAF and the paleotectonic suture and thus not resolved. In this respect, the geometry and deep structure of the NAF as well as the other structures shaping the crust of this region are still under much debate. Okay et al. (1994) described the Istanbul zone as a terrane which was formed due to

southward motion along two large transform faults (Figure 1-1). Recently, Nikishin et al. (2015) suggested existence of another major wrench fault between Central Pontides and Eastern Pontides. Actual position of so-called Abana Fault is still enigmatic but assumed to be bounding the Central Pontide Supercomplex from east.

In order to understand associated deformation in great depths, seismic anisotropy can also be used as an important proxy. Present and/or preserved rock fabric and cracks forms seismic anisotropy and it can be modeled to reveal possibble fabric and/or crack orientations linked to geodynamic processes that the region had faced through its tectonic evolution. Thus, we developed a computer program to model multi-layered seismic anisotropy from shear wave splitting observations and in a parallel study (Pamir et al. 2014) applied it to the region in South Central Anatolia where the edge of Cyprus slab is located (Figure 1-1).

1-2- Data

National seismic networks of Turkey display very good coverage in the west and southwest which make it possible to generate images of fairly high resolution for that region. However, the coverage in central and northern Anatolia becomes sparser which causes degradation in quality of the created images. Especially the lack of stations on the critical locations, particularly on the suture zones or plate boundaries is manifest. Hence, there was a need for increment of the seismic station density in the central and northern Anatolia which was solved by installation of numerous interim seismic networks in different regions of the Anatolian plate. The aim was to temporarily increase the seismic station density of that region. From these experiments, CD-CAT, NAF and ETSE experiments are of higher importance related to their region of coverage (Figure 1-2).

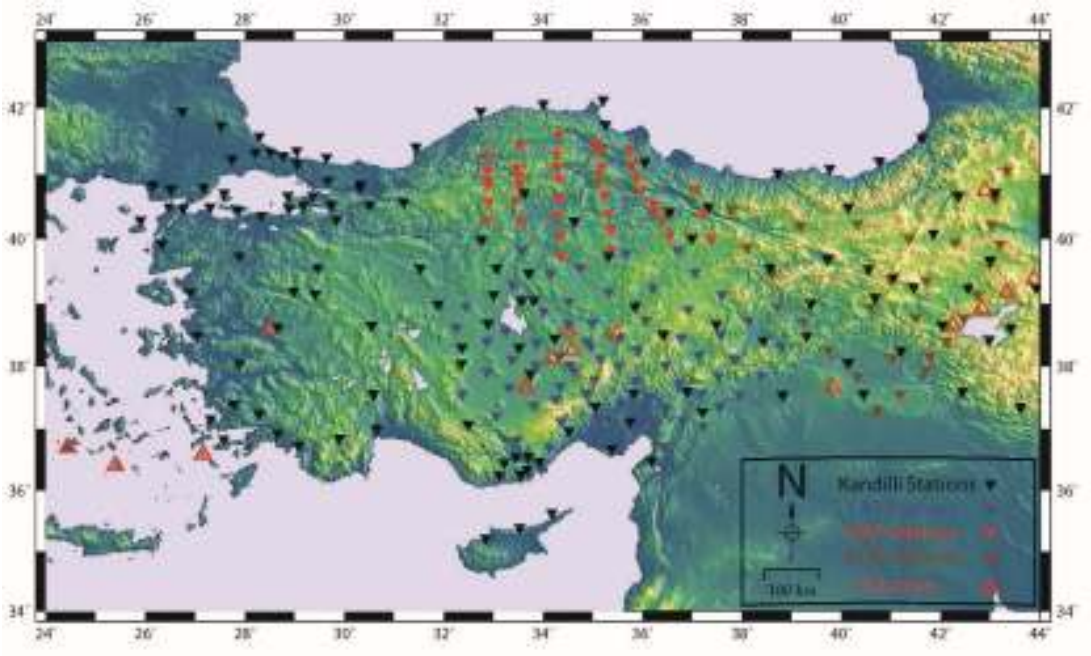

Figure 1-2: Distribution of seismic stations along Turkey. Black inverse triangles represent the Kandilli national network permanent stations. Blue inverse triangles represent the temporary CAT stations. Red inverse triangles represent the NAF experiment temporary stations and brown inverse triangles represents the ETSE temporary network. Red unfiiled triangles represent the recent volcanos.

1-2-1- The CD-CAT experiment

This project was an integrated program of geophysical experiments (2-year passive seismic experiment plus magnetotelluric profiling); geochemical analysis of Cenozoic volcanic rocks; structural analysis of rocks and sediments across the Anatolian interior; geo/thermochronology of volcanic rocks and terrestrial basin deposits; geomorphic analysis of the Cenozoic evolution of the Anatolian landscape; and numerical modeling of lithosphere dynamics. These data will characterize the present-day thermal-physicochemical state of the lithosphere from mantle to surface and will allow us to reconstruct a record of lithosphere dynamics, with a particular focus on the past 20 million years.

As part of geophysical investigations, passive seismology was utilized in this project benefiting from 72 temporarily installed seismic stations and national network stations within the region (Figure 1-2). During the project, various seismic methods were used to reveal the crust and mantle structures including receiver functions analysis (Abgarmi et al. 2017), teleseismic body wave tomography (Portner et al. 2018), surface and ambient noise tomography (Delph et al. 2015a). Seismicity is analyzed to identify the active tectonic structures and ongoing deformation in the region (Özacar et al. 2015, Birsoy 2018).

Moreover, seismic anisotropy along crust and mantle was studied using shear wave splitting analysis to discover the effect of tectonic escape and mantle flow at the edge of Cyprus slab (Pamir et al. 2014, Soysal et al. 1981) looking at the absolute plate motion direction an general trends of fast polarization direction along the region reveals the mantle flow directions of this region. Comparing this directions with the surficial motions (the GPS velocities) reveals the decoupled characteristics of the deformations which implies the existence of complex seismic anisotropy (Figure 1-3). The assumption of a simple anisotropy will be over simplification and will lead to unrealistic tectonic interpretation.

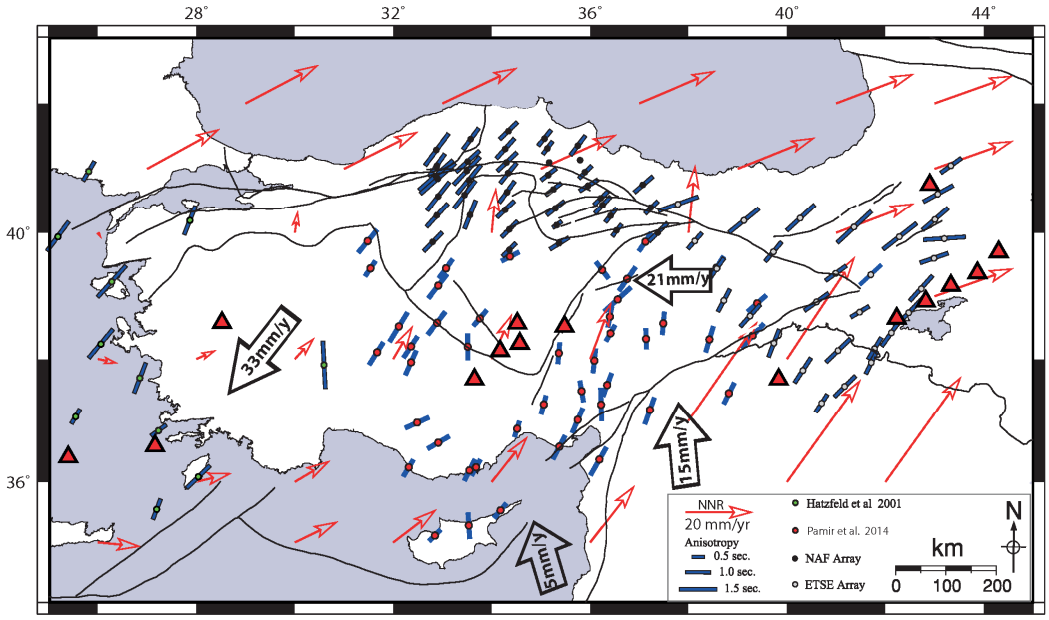

Figure 1-3: The relation between no net rotation absolute plate motion and fast polarization direction resulted from shear wave splitting analysis. Absolute plate motions taken from UNAVCO project represented as red vectors. Fast polarization directions are taken from various references (the NAF experiment, Biryol et al., 2009, the ETSE experiment, Sandvol et al., 2003, western Turkey, Hatzfeld et al., 2001, central Turkey, Pamir et al., 2014). Relative plate motions shown in black vectors are relative to fixed Eurasian plate (Reilinger 2006). Solid black lines represent the major faults and sutures and red triangles represent the famous Holocene volcanos.

1-2-2- The NAF experiment

The project was a passive seismic experiment in which 39 broadband seismic stations were deployed and functioned for two years (Figure 1-2). To improve the resolution, stations from national seismic network (Kandilli observatory) which are within the study area were also added to the analysis. The recorded data is used to identify the seismicity and present subsurface structure in the vicinity of the central curved segment of NAF. For this purpose, teleseismic body wave seismic tomography (Biryol et al. 2011) ambient noise tomography (Warren et al. 2013), Pn tomography (Gans et al. 2009), receiver function (Özacar et al. 2010) and shear-

wave splitting (Biryol et al. 2010) analyses were conducted. Moreover, the first motion solutions of relocated earthquakes were computed and active stress field was mapped out in the region (Karasözen et al. 2014).

1-3- Methodology

This dissertation consists of two major passive seismic methods which differ in terms of data, processing procedures and results. For regional studies of the subsurface structures, the teleseismic P-wave receiver function method is utilized using different approaches in data processing and analysis. On the other hand, the analysis of complex seismic anisotropy is unified in a comprehensive computer program which comprises various tools that are dedicated to accomplish different tasks.

1-3-1- Receiver function

Receiver function is a widely used technique to image the subsurface discontinuities. This method is based on conversion of the incident wave in an interface and recording the original and converted phases at the surface stations. This method is sensitive to impedance contrast and therefore image seismic discontinuities underneath the station (Figure 1-4). The amount of contrast will be reflected in the amplitude of the RF signal so that the high amplitude sharp RF signals represent high impedance contrasts whereas small amplitude and wide RF signals indicate transitional velocity changes along that interface. Advantage of this method is the ability of detecting low velocity layers (downward decrement of the velocity) which

will emerge as a negative pulse on the receiver function graph. In the thesis, the teleseismic P-wave Receiver function has been utilized in imaging the subsurface discontinuities. It is also worth to note that the CAT data also contains PP receiver functions to enlarge the azimutal coverage.

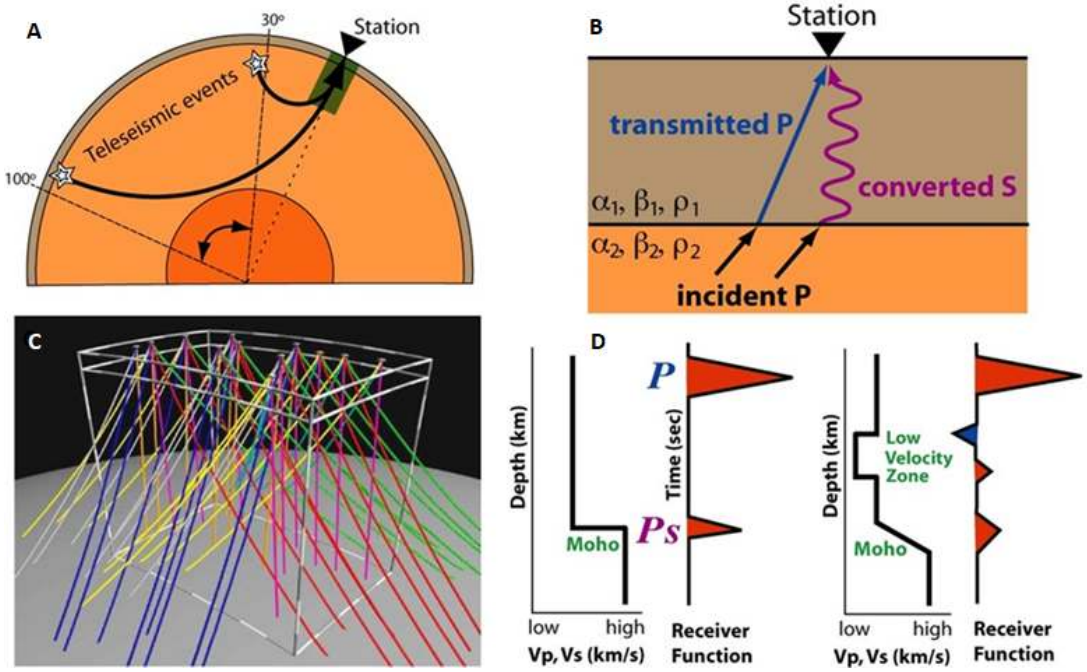

Figure 1-4: Principals of Teleseismic P wave receiver function. A) Exhibits the importance of using the teleseismic events to have the incidence angles close to vertical. B) Conversion of the incident P wave at the interface with impedance contrast. C) The necessity of full backazimuthal coverage to sample underneath the station from all sides and detect possible variation/anisotropy and D) response of the receiver function analysis to a sharp, transitional boundary and low velocity zone.

The concept of calculating the P-wave receiver function is based on deconvolution of the horizontal waveform from the vertical one. There are two different procedures to handle this process which comprise the time domain and frequency domain deconvolution. In frequency domain, deconvolution is transformed into normal division as in equation 1 shown below,

$$H_r(\omega) = \frac{D_R(\omega)\overline{D_V}(\omega)}{\phi(\omega)} G(\omega) \qquad (1)$$

where $\phi(\omega) = \max[D_R(\omega)\overline{D_V}(\omega), c.\max\{D_V(\omega)\overline{D_V}(\omega)\}]$

In which $H_r(\omega)$ is Fourier transformation of radial receiver function, $D_R(\omega), D_V(\omega)$ are Fourier transformations of radial and vertical components of seismic trace. $\overline{D_V}(\omega)$is the complex conjugate of the $D_V(\omega)$. "*c*" is the water level parameter and $G(\omega)$ is Gaussian filter where:

$$G(\omega) = \xi e^{-\omega^2/4a^2} \qquad (2)$$

where "*a*" is the Gaussian filter width.

Width of the Gaussian filter will define the resolution of the RF, so the filter width which has direct relation to the frequency, should be adjusted with some care (equation 2). Large filter widths can cause overfitting or artificially generating unrealistic anomalies whereas low filter numbers (low frequencies) can cause aliasing in the anomaly.

However, in any division if the denominator converges to zero, the function will become unstable (or in other words that function will converge to infinity) so to avoid the instability, water level filtering will also have introduced in the calculation processes. Incorporating the water level filter, will resolve the unstable division solutions, still adds another problem to the frequency domain procedure. The problem originates from removing very weak signals due to using water level filtering for the traces with low SNR which will lead to lose the concealed weak signal within the noise. The *PWaveQN* program is dedicated to perform Frequency domain deconvolution (Ammon 1997).

The other procedure consists of iterative time domain deconvolution which for the high SNR traces, results are slightly poor compared to the frequency domain deconvolution method but for very noisy data with low SNR this method leads to significantly better results. Thus we have utilized this technique in this study and used the program called Iterdecon (Ligorria and Ammon, 1999).

The reason behind using the teleseismic events can be described in two different cases; the geometric and mathematic reasons. The mathematic reason behind the usage of teleseismic events is manifested in equation 1. Focusing in the formula, reveals that if we want to have the resulted RF to be at reasonable energy, the most of the vertical P wave should be concentrated in the vertical component whereas the converted P to S component should be in the radial one. This will lead to prefer near to vertical incidence angles which means usage of the teleseismic events will be demanded. The geometric reason is the further the inclination of the waves from vertical, the farther the waves will apart from the station which means the resulted stacked RF will be average of very vast area and cannot be representative to that location. To check the conditions of the deconvolution process, the quality control is necessary. This process is performed in sequence of steps which, the initial step, comprises the visual inspection of all three components of all events which are

recorded by a seismic station. Noisy traces or traces with unclear P wave arrivals will be omitted at this step. The next step is carried on after deconvolution process which all deconvolved RF traces are allocated with a number representing the quality of the deconvolution. This number, or so called the reduction value should pass a threshold for a receiver function trace to be acceptable. The final step, will be the visually examination of the final RF traces for unusual traces which already passed the two former steps.

Proceeding the deconvolution processes and quality control of the output receiver functions, this output time histories need be inverted to migrate from time domain to depth domain. However, while the number of unknowns in this problem, although the Vp will be assumed to be fixed, is more than one (including depth and the Vs or Vp/Vs ratio), to accomplish the migration task, special algorithms should be utilized. There are several algorithms to perform the migration task and assess the resulted receiver functions which include the H-K stacking, Stack windowing and different algorithms of CCP stacking method.

1-3-1-1- The H-K Stacking method:

H-K stacking is a simple and automated way to measure crustal thickness (H) and Vp/Vs ratios (κ) through the summation of the primary conversion (Ps) from the Moho and its associated multiples (PpPs and PsPs + PpSs), assuming flat-lying homogeneous layers. This method is based on the fact that the primary conversion and its first and second multiples will intersect at a point on the depth Vs the Vp/Vs ratio plot which represents the depth of the interface and the average Vp/Vs ratio of the entire column (Figure 1-5). This method first introduced by Zhu and Kanamori, (2000), which in general is an algorithm to sum up the amplitudes of the mentioned

phases at their predict arrival time. This process is based on a grid search over H and K and finally find the proper solution in a point that all phases add up coherently.

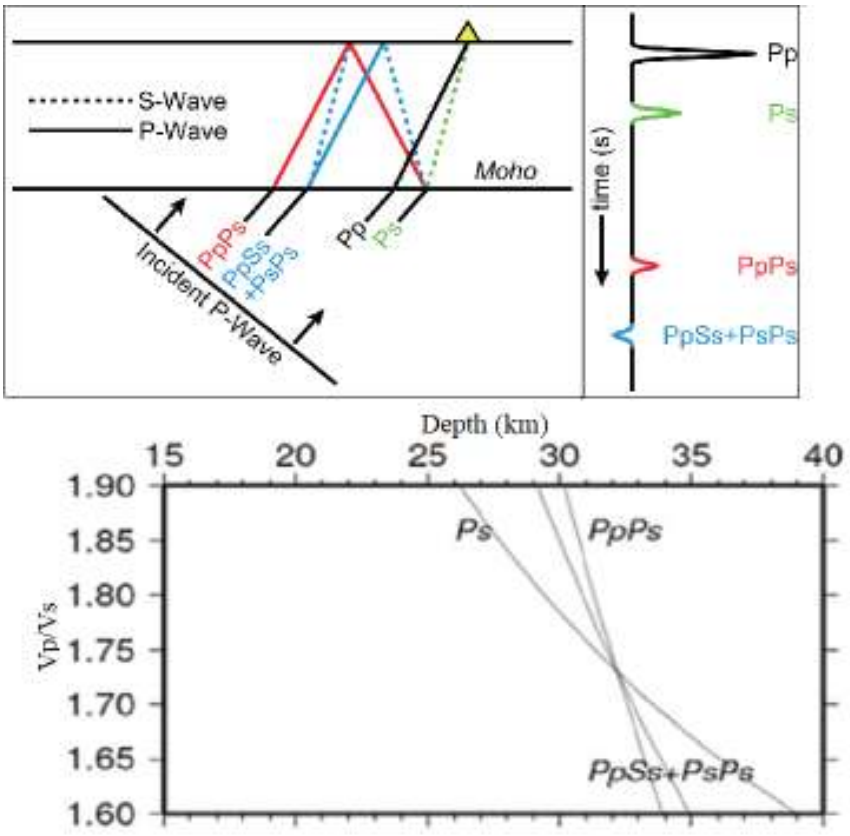

Figure 1-5: Up shows different phases in receiver function analysis. Ps is the main receiver function and PpPs and PsPs+PpSs are the first and second reverberations respectively. Down shows the principal of the H-K stacking method in which at one definite depth with definite Vp/Vs ratio all three phases intersect at a single point. (Zhu and Kanamori, 2000)

Time difference (t_{Ps}) between direct P and primary conversion (Ps) from the Moho is a function of crustal thickness (H) and average P and S wave velocities (V_p, V_s) in the crust which is expressed as in equation 3 given below

$$H = \frac{t_{Ps}}{\sqrt{V_s^{-2} - P^2} - \sqrt{V_p^{-2} - P^2}} \qquad (3)$$

where P is the ray parameter.

Since the teleseismic events are used and P wave incidence angle is near to vertical, the horizontal deviation of the piercing point from the station will be no more than 10 Km (Zhu and Kanamori, 2000) so the deviation of ray parameter will not have significant effect on the calculated depth. Similarly, it is proven that the P wave velocity (Vp) has negligible effect on the calculated depth as well (Zhu and Kanamori, 2000). So in the equation *3* there are two unknowns whereas just one observation will be performed which will lead to non-uniqueness of the model. To avoid this problem, two other phases will also be used that the arrival time of these phases are expressed in equations *4* and *5*.

$$H = \frac{t_{PpPs}}{\sqrt{V_s^{-2} - P^2} + \sqrt{V_p^{-2} - P^2}} \qquad (4)$$

$$H = \frac{t_{PpSs+PsPs}}{2\sqrt{V_s^{-2} - P^2}} \qquad (5)$$

where $t_{PpPs}$and $t_{PpSs+PsPs}$, represent the differential travel times of the first and second multiples of the direct conversion respectively. Therefore adding these three phases will lead to the final solution of the problem (Zandt and Ammon 1995).

1-3-1-2- Stack windowing Analysis

In tectonically complex areas, a more manual method for identifying the multiples from the Moho discontinuity which we call stack windowing analysis (SWA) is preferable. SWA builds on previous approaches in estimating κ through the manual picking of the Ps conversion and the PpPs multiple (Zandt and Ammon, 1995). Because single earthquake traces can be contaminated with noise, we stack all receiver functions at an individual station to increase the signal to noise ratio of the data after normalizing the amplitude of a trace and correcting for moveout. We then choose a time window around the Ps and PpPs arrivals on the stacked trace, with the maximum amplitude in the time window being automatically chosen as the conversion of interest (Figure 1-6).

From these times, we can calculate κ and *H* as illustrated in equations 6 and 7 given below (Zandt and Ammon, 1995).

$$H = \frac{t_{Ps} \times V_P}{k \times \sqrt{1 - P^2 \left(\frac{V_P}{k}\right)^2} - \sqrt{1 - P^2 V_P^2}} \qquad (6)$$

$$k = (1 - P^2 V_P^2)\left(\frac{2t_{Ps}}{t_{PpPs} - t_{Ps}} + 1\right) + P^2 V_P^2 \qquad (7)$$

where *Vp* is an assumed value for average P-wave velocity in the crust (6.1 km/s in this study) that generally has a neglicable effect on overall crustal thickness estimates (Zhu and Kanamori, 2000), P is the ray parameter which is also used to correct for moveout in the stacking routine, and t_{PS} and t_{PpPs} are the time picks from the stacked receiver function at a station of interest.

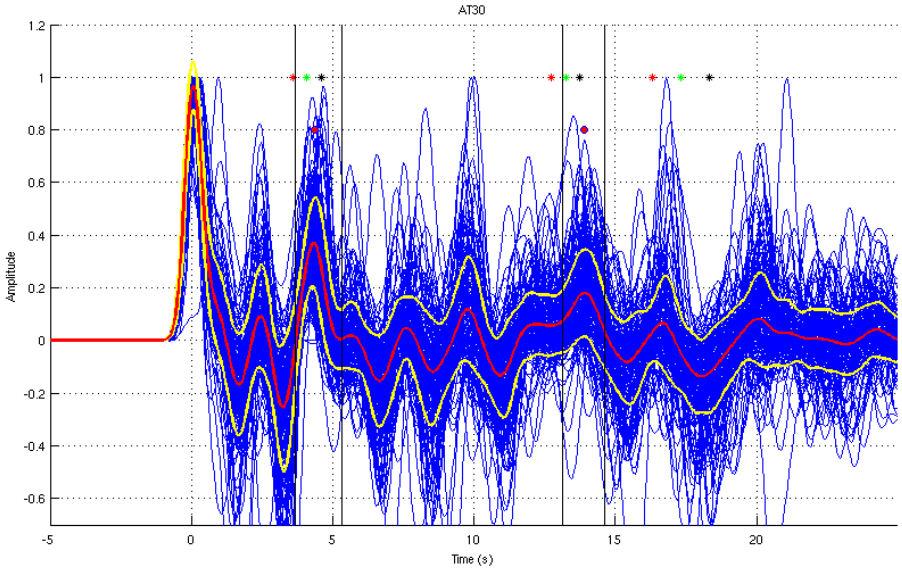

Figure 1-6: Stack windowing analysis (SWA), blue lines represent all the traces put togeather, red line is the average of all traces and yellow lines are average (red line) plus and minus standar deviation. Red dot is the maximum point within the picked window and red, green and black astericksses are expected arrival time of Ps, PpPs and PpSs+PsPs phases for crustal thickness of 35 km and Vp/Vs ratios of 1.7, 1.8 and 1.9 respectively. Solid vertical lines represent the selected windows for Ps and its first moltiple.

Errors are then estimated by comparing the chosen arrivals from the stacked trace with time of the maximum amplitudes in the chosen time window on individual traces by taking the standard deviation of the time differences. As shown in equations 8 and 9, by using this uncertainty in a standard propagation of errors calculation, we can estimate errors in κ and H:

$$\Delta k = \sqrt{\left(\frac{\partial k}{\partial t_{Ps}}\Delta t_{Ps}\right)^2 + \left(\frac{\partial k}{\partial t_{PpPs}}\Delta t_{PpPs}\right)^2} \quad (8)$$

$$\Delta H = \sqrt{\left(\frac{\partial H}{\partial t_{Ps}}\Delta t_{Ps}\right)^2 + \left(\frac{\partial H}{\partial k}\Delta k\right)^2} \quad (9)$$

where Δ is the standard deviation of the measurement.

This technique, while requiring more interaction than H-κ stacking, allows for an improved recovery of both crustal thickness and Vp/Vs ratios where traditional H-κ stacking analysis may struggle, while obtaining very similar results in areas of simple crustal structure.

1-3-1-3- CCP stacking

Common conversion point (CCP) stacking analysis (Dueker and Sheehan, 1997) is another method to resolve spatial variability in the crust and uppermost mantle to create a three-dimensional (3D) volume of receiver function amplitude. In this analysis, the region of interest is gridded into bins based on user-defined width and spacing. Receiver functions are migrated to depth and ray traced back to their theoretical locations in the Earth, and receiver function amplitudes that plot within the same bin are averaged to represent the structure in that bin. There are two

different approaches to calculate the crustal thickness with variable Vp/Vs ratio, first method which is interactive involves picking of Ps and PpPs phases manually from the cross-sections generated by the CCP stacking using constant Vp/Vs ratio (Figure1-7).

Consequently these two picks will be used to recalculate the correct depth and Vp/Vs ratio for each bin by using the following equations (10 and 11) suggested by Zandt and Ammon (1995).

$$VpVs = \sqrt{\left(\frac{H_{Ps} \times \left(\sqrt{\left(\frac{VpVs_{cons}}{Vp}\right)^2 - P^2} - \sqrt{Vp^{-2} - P^2} \right)}{H_{PpPs} \times \sqrt{Vp^{-2} - P^2}} + 1 \right)^2 \times (1 - P^2 Vp^2)} + P^2 Vp^2 \qquad (10)$$

$$H = \frac{t_{Ps}}{\sqrt{\left(\frac{VpVs}{Vp}\right)^2 - P^2} - \sqrt{V_p^{-2} - P^2}} \qquad (11)$$

where H_{Ps} and H_{PpPs} are the calculated depths for Ps and PpPs phases respectively using the constant Vp/Vs ratio which illustrated as $VpVs_{cons}$.

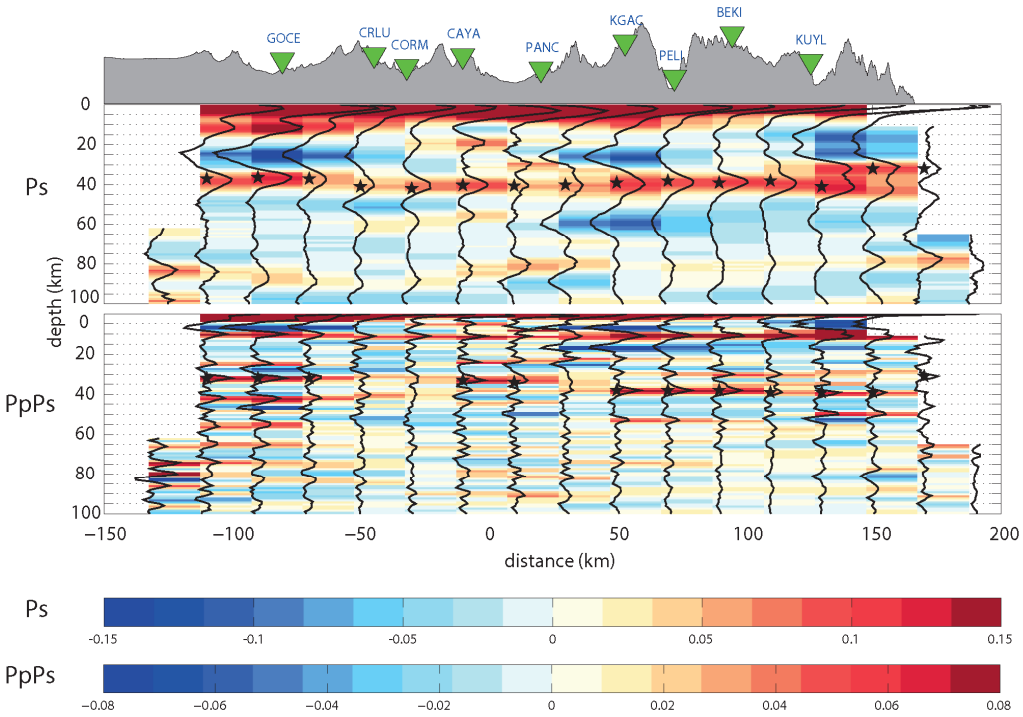

Figure 1-7: Interactive phase picking CCP stacking. Black stars represent the picked depth for the Ps (above) or PpPs (below) phases.

Second method is the adaptive common conversion point approach described in Delph and Porter (2015), which allows our bin width to dilate from 0.3° to 1° until each bin has at least 10 rays. This method gives smoother models that are more realistic because the individual traces will not create bullseyes in the resultant model. This approach is embedded in the Funclab (Eagar and Fouch. 2012) program and has the capability of receiving the variable Vp/Vs ratio as a 3D bulk which this ratio is obtained from previous steps.

1-3-2- Shear wave splitting

Due to variation of velocity in an anisotropic volume in different directions, shear waves passing through this medium will experience splitting into two orthogonal phases which are parallel and perpendicular to the polarization direction (Figure 1-8). In crust, splitting is related to the crack alignment related to the stress directions (Crampin, 1994, 1999) and the density of the cracks and their direction are expressed as the delay time and polarization direction respectively. One may ask about the observations which show no splitting or in other words the Null observations. There are two possibilities that one measurement can show no anisotropy or splitting; first there is no anisotropy contained in that medium which in this case all observations from all directions will show no splitting and second the backazimuth of the event is parallel or perpendicular to the polarization direction (Wüstefeld and Bokelmann, 2006).

Shear-wave splitting analysis of teleseismic data is widely used to image the anisotropy in the Earth's interior. Splitting observations are used to infer crust and mantle fabric beneath recording stations related to past and current deformations. Normally, shear-wave splitting analyses are performed under the assumption of a simple model composed of just one horizontal layer with a horizontal axis of symmetry. But in some complex cases, the splitting parameters show strong backazimuthal dependency. Previous researchers had identified anisotropic complexities at different tectonic settings and applied various approaches to model them. Most commonly, such complexities are modelled using multiple anisotropic layers with priori constraints from geologic data

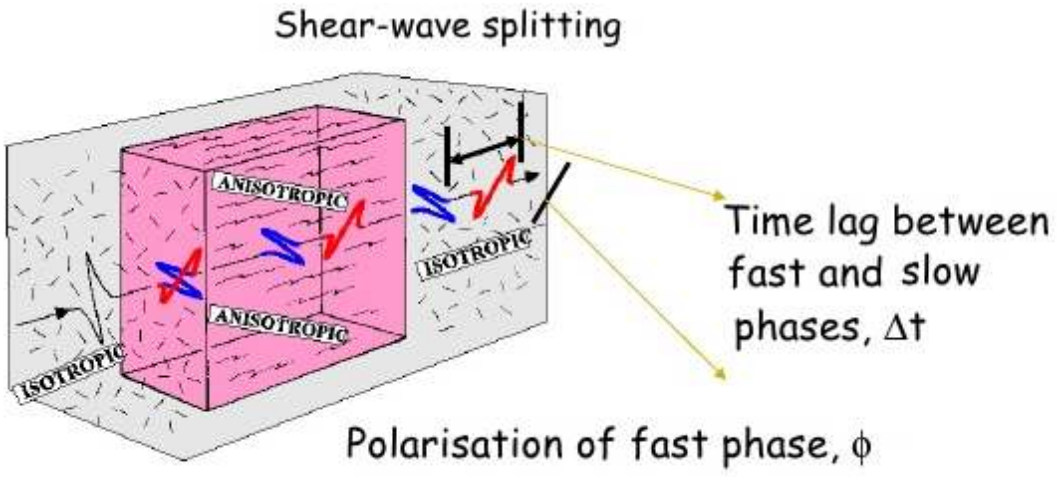

Figure 1-8: Basics of shear wave splitting which shows how an incident shear wave splits into two slow and fast phases due to propagation through an anisotropic medium (Crampin 1981).

There are three different interpretations for variation of splitting parameters with respect to backazimuth: (1) two-layered horizontal anisotropy (Savage and Silver, 1993; Silver and Savage, 1994) or three or more anisotropic layers (e.g., Yang et al., 2014) can generate backazimuthal dependencies with 90° of periodicity, (2) laterally varying anisotropy (Alsina and Snieder, 1995), and (3) inclined symmetry axis in the lithosphere (Babuška et al., 1984, 1993; Plomerová et al., 1996; Šílený and Plomerová, 1996). In the complex tectonic settings, presence of two horizontal layers of anisotropy is the most commonly proposed model (Figure 1-9). Thus, we introduce our user-friendly graphical program M-Split that uses the same forward formulas introduced by Silver and Savage (1994) to model the anisotropic parameters showing strong backazimuthal dependencies but enhanced misfit calculation algorithms for different observation conditions and limitations.

Analysis of complex anisotropy suffers from the presence of high level of non-uniqueness in the forward problem; hence, in this program a sensitivity analysis tool is also included to find all possible solutions in model space by plotting all local extremums. This program is a tool that calculates the misfit between the observations and all models resulted from grid search over model space. Misfit calculation procedure follows the formula first introduced by Silver and Savage (1994). There are several enhancements performed on the misfit calculation formulas related to the observation condition.

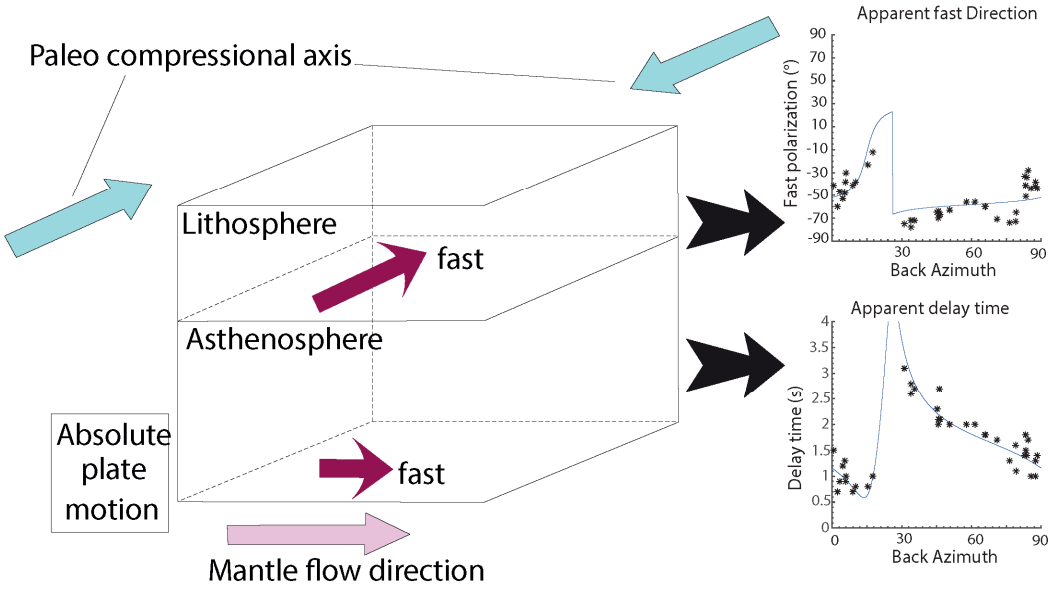

Figure 1-9: Left, schematic configuration of two layered anisotropy in upper mantle and crust. Relation of the fast polarization direction with the mantle flow and absolute plate motion in upper mantle and paleo stress in the crust. Right, The variation of the apparent anisotropic parameters with respect to backazimuth (modified after Kano et al., 2011).

The main misfit formula utilized in this program is as in equation 12 given below,

$$misfit_{uw} = \sum_{i=1}^{n} \left[\frac{\left(\emptyset_{obs,i} - \emptyset_{calc,i}\right)^2}{(mean_{\emptyset})^2} + \frac{\left(\delta t_{obs,i} - \delta t_{calc,i}\right)^2}{(mean_{\delta t})^2} \right] \qquad (12)$$

where $\emptyset_{obs,i}$, $\emptyset_{calc,i}$, $\delta t_{obs,i}$ and $\delta t_{calc,i}$ are *i*'th observed and calculated fast polarization direction and observed and calculated delay times, respectively, and $mean_{\emptyset}$ and $mean_{\delta t}$ are mathematical mean values of fast polarization directions and delay times for all observations, respectively. In this formulation, both $\emptyset$ and δt segments are normalized by the corresponding mean value of all observations.

Second algorithm is the weighted method that gives weights according to measurement errors so that observations with small errors will have greater effect in the misfit calculation. This method is suitable for the observations that have solitary points with small errors that are a critical part of the model diagram and therefore it is important that these points have more effect on the final calculated model (equation *13*).

$$misfit_{w} = \sum_{i=1}^{n} \left[\frac{\left(\emptyset_{obs,i} - \emptyset_{calc,i}\right)^2}{\left(E_{\emptyset,i}\right)^2} + \frac{\left(\delta t_{obs,i} - \delta t_{calc,i}\right)^2}{\left(E_{\delta t,i}\right)^2} \right] \qquad (13)$$

$$E_{\emptyset,i} = (\emptyset_{max,i} - \emptyset_{min,i})/2$$

$$E_{\delta t,i} = (\delta t_{max,i} - \delta t_{min,i})/2$$

where $\emptyset_{obs,i}$, $\emptyset_{calc,i}$, $\delta t_{obs,i}$ and $\delta t_{calc,i}$ are *i*'th observed and calculated fast polarization direction and observed and calculated delay times, respectively. $E_{\emptyset,i}$and$E_{\delta t,i}$are errors on fast polarization direction and delay time for *i*'th observation.

Finally, the third method is a band-fit method that is developed to reduce the effect of individual observations with small errors that dominate the final model. This method is proper for the input with the individual observations that have negative effect on the extracted model (equation 14).

$$misfit_{bf} = \sum_{i=1}^{n} \left[\frac{\left(\emptyset_{dif,i}\right)^2}{(mean_{\emptyset})^2} + \frac{\left(\delta t_{dif,i}\right)^2}{(mean_{\delta t})^2} \right] \qquad (14)$$

$$\emptyset_{dif,i} = \begin{cases} 0 & if \quad \left(\emptyset_{obs,i} - \emptyset_{calc,i}\right) \leq E_{\emptyset,i} \\ \left(\emptyset_{obs,i} - \emptyset_{calc,i}\right) - E_{\emptyset,i} & if \quad \left(\emptyset_{obs,i} - \emptyset_{calc,i}\right) > E_{\emptyset,i} \end{cases}$$

$$\delta t_{dif,i} = \begin{cases} 0 & if \quad \left(\delta t_{obs,i} - \delta t_{calc,i}\right) \leq E_{\delta t,i} \\ \left(\delta t_{obs,i} - \delta t_{calc,i}\right) - E_{\delta t,i} & if \quad \left(\delta t_{obs,i} - \delta t_{calc,i}\right) > E_{\delta t,i} \end{cases}$$

where $\emptyset_{obs,i}$, $\emptyset_{calc,i}$, $\delta t_{obs,i}$ and $\delta t_{calc,i}$ are *i*'th observed and calculated fast polarization direction and observed and calculated delay times, respectively. $E_{\emptyset,i}$ and $E_{\delta t,i}$ are errors on fast polarization direction and delay time for *i*'th observation. $mean_{\emptyset}$ and $mean_{\delta t}$ are mean values of fast polarization direction and delay time for all observations, respectively.

1-4- Organization of thesis

The thesis is composed of five chapters counting the introduction chapter, the following three chapters are designed as separate papers followed by final chaper where all of our results and derived conclusions are listed and discussed. In the first study, which will be covered in the second chapter, focus will be on the south central Anatolia with an aim to understand the ongoing tectonic processes in this region by analyzing the crustal discontinuity structure in the sub-surface. This is accomplished by using the teleseismic P wave receiver function analysis for the data collected by national network of Turkey as well as the data collected by the temporarily deployed seismic network. The temporary seismic network was deployed along central Anatolia as part of CD-CAT project which I have participated in installation, servicing, data collection and dismantling of this network. In this chapter, receiver function analysis which was conducted by me as part of my PhD work is presented. It is worth to note that this study is recently published as a scienctific paper under my correspondence as first leading author (Abgarmi et al. 2017). The major observations include but not limited to the thickness of the crust, the traces of the profound faulting in the deep interior of the earth, the existence of low velocity layers underneath the young volcanos and also the presence of the slab and its possible geometry.

In the third chapter, the focus will be on the curved central segment of the NAF which overlaps in part with the Paleo-Tethyan suture. In order to reveal the deep geometry of NAF and identify signatures of past tectonic processes on the crustal deformation, teleseismic receiver function analysis is conducted to generate a model of crustal structures based on the seismic impedance contrast. Most of the dada which are used in this study were collected by the temporary seismic network of NAF passive seismic experiment with the NSF grant number EAR0309838. In this study, newly developed interactive Ps and PpPs phase picking on CCP stacking plots

is utilized to identify MOHO depths and corresponding Vp/Vs ratios. The resultant crustal thickness variations are later used to locate preserved paleotectonic boundaries in the subsurface and interpret the depth extent and geometry of NAF. This receiver function study which was conducted by me as part of my PhD work is presented in a scientific meeting (Ozacar and Abgarmi, 2017) but not yet published and currently under preparation for journal submission.

In the fourth chapter, the M-split program which is developed to assess complex seismic anisotropy will be discussed. Up to now, there was no open access program providing tools to analyse multi-layered seismic anisotropy which gave rise to the M-split program. This program is dedicated to analyse two-layered anisotropy with horizontal symmetry axis. Additionally there are several tools embedded in the program to facilitate the analysing process and enhance program to map out the non-uniqueness present in the complex anisotropic models by conducting systematic grid searches on model parameter space. This program and all modulus and codes within are developed by myself and also all the tests and validation of the program using synthetic and real data are performed by me as well. This study is recently published as a scienctific paper under my correspondence as first leading author (Abgarmi and Ozacar 2017). In another study, the program is also tested on actual data recorded at permanent national seismic stations located in the south central Anatolia where the edge of Cyprus slab is expected to produce complex seismic anisotropy associated to mantle flow and tectonic escape (Pamir et al. 2014).

CHAPTER 2

STRUCTURE OF THE CRUST AND AFRICAN SLAB BENEATH THE CENTRAL ANATOLIAN PLATEAU FROM RECEIVER FUNCTIONS: NEW INSIGHTS ON ISOSTATIC COMPENSATION AND SLAB DYNAMICS[1]

The Central Anatolian Plateau in Turkey is a region with a long history of subduction, continental collision, accretion of continental fragments and finally slab tearing/break-off and tectonic escape. Central Anatolia is presently characterized as a nascent plateau with widespread Neogene volcanism and predominantly transtensional deformation. To elucidate the present-day crustal and upper mantle structure of this region, teleseismic receiver functions are calculated from 500 seismic events recorded on 92 temporary and permanent broadband seismic stations. Overall, we see a good correlation between crustal thickness and elevation throughout central Anatolia, indicating that the crust may be well-compensated throughout the region. We observe the thickest crust beneath the Taurus Mountains (>40 km), which thins rapidly to the south in the Adana Basin and Arabian Plate and to the northwest across the Inner Tauride Suture beneath the Tuz Gölü Basin and Kırşehir Block. Within the Central Anatolian Volcanic Province, we observe several low seismic velocity layers ranging from 15 to 25 km depth that spatially correlate with the Neogene volcanism in the region, and may represent crustal magma reservoirs. Beneath the Central Taurus Mountains, we observe a positive amplitude,

[1] This chapter is published as the following paper: Abgarmi, B., Delph, J.R., Ozacar, A.A., Beck, S.L., Zandt, G., Sandvol, E., Turkelli, N., and Biryol, C.B., 2017, Structure of the crust and African slab beneath the central Anatolian plateau from receiver functions: New insights on isostatic compensation and slab dynamics: Geosphere, v. 13, no. 6, p. 1–14, doi:10.1130/GES01509.1.

subhorizontal receiver function arrival below the Anatolian continental Moho around 50 – 80 km that we interpret as the gently dipping Moho of the subducting African lithosphere abruptly ending near the northernmost extent of the Central Taurus Mountains. We suggest that the uplift of the Central Taurus Mountains (~2 km since 8 Ma), which are capped by flat-lying carbonates of late Miocene marine units, can be explained by an isostatic uplift during late Miocene-Pliocene followed by slab break-off and subsequent rebound coeval with the onset of faster uplift rates during late Pliocene-early Pleistocene. The Moho signature of the subducting African lithosphere terminates near the southernmost extent of the Central Anatolian Volcanic Province, where geochemical signatures in the Quaternary volcanics indicate asthenospheric material is rising to shallow mantle depths.

2-1- Introduction

Central Anatolia displays a typical plateau-like morphology that appears similar to other collision-related plateaus but on a smaller scale (Figure2-1). The crustal architecture of the Central Anatolian Plateau comprises the amalgamation of continental fragments that coalesced during the closure of the Neo-Tethyan Ocean system between Africa-Arabia and Eurasia and records both subduction and collisional-related processes (Şengör & Yılmaz 1981). To the east of the Central Anatolian Plateau, compression related to the Arabia-Eurasia continental collision dominates the formation and development of tectonic structures, while regional extension due to the rollback of the African slab has dominated the west since the Miocene (Bozkurt 2001; Ring et al., 2010). These processes have led to the development of the Anatolian Plate, which has been extruding westwards since the Miocene as a result of African slab rollback and Arabia-Eurasia collision (Şengör et al. 1985; Reilinger et al. 2006).

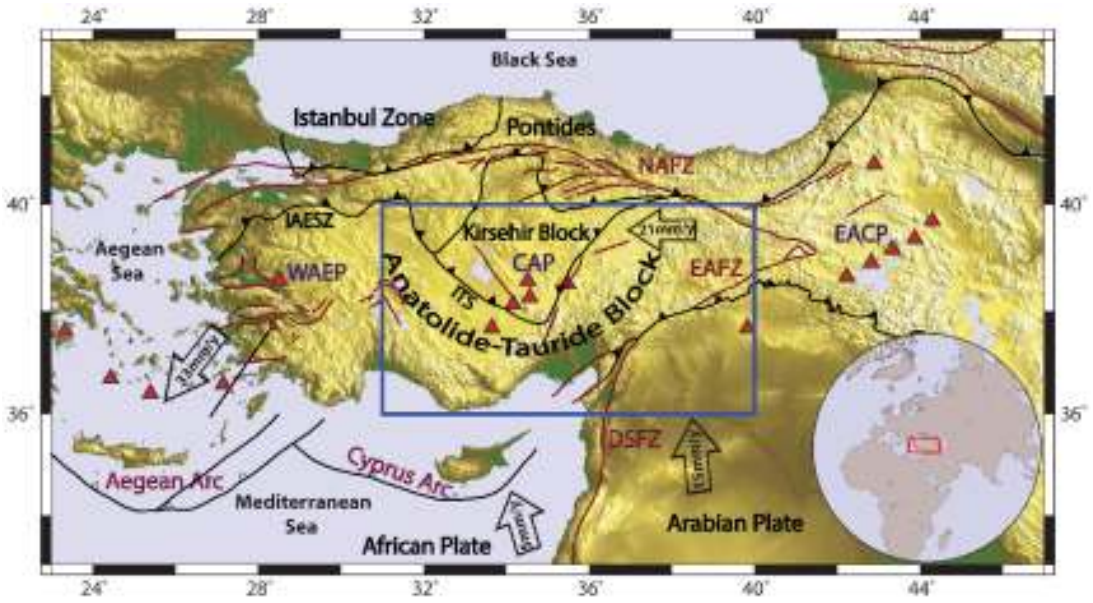

Figure 2-1:Tectonic map of Turkey and near vicinity showing active faults, terranes/blocks and bounding sutures (after Okay & Tuysuz 1999). Unfilled arrows show the plate motions relative to the Eurasian Plate taken from Reilinger et al. (2006). The study area is outlined by the blue rectangle. Red triangles are Holocene volcanoes; black lines with filled triangles are suture zones; black lines with unfilled triangles are present day trenches; red lines are active structures and fault zones. CAP: Central Anatolian Province, DSFZ: Dead Sea Fault Zone, EAFZ: East Anatolian Fault Zone, EACP: East Anatolian Contractional Province, IAESZ: Izmir- Ankara- Erzincan Suture Zone, ITS: Inner Tauride Suture, NAFZ: North Anatolian Fault Zone, WAEP: West Anatolian Extensional Province.

Thanks to the expansion of seismic station coverage in Turkey, a number of regional-scale studies of the eastern Mediterranean have provided researchers with a broad understanding of the seismic structure of the Anatolian system (e.g. Biryol et al. 2011; Mutlu & Karabulut 2011; Salaun et al. 2012; Fichtner et al. 2013; Vanacore et al. 2013; Delph et al. 2015a; Govers & Fichtner 2016). Smaller-scale, regional studies have also been performed using temporary seismic deployments to investigate the seismic structure of this system in higher detail, such as the North Anatolian Fault Experiment (Beck & Zandt, 2005) and the Eastern Turkey Seismic Experiment (Sandvol et al. 2003). This has resulted in dense seismic station coverage

throughout most of Turkey when combined with the extensive backbone network of the Kandilli Observatory and Earthquake Research Institute (KOERI). However, until recently, seismic station coverage and associated studies investigating central Anatolia have been largely neglected due to its relative stability and assumed low potential of large-magnitude earthquakes.

This study represents the first analysis of a large dataset collected as part of the Continental Dynamics – Central Anatolian Tectonics (CD-CAT) project that combines interdisciplinary expertise to investigate the structure and evolution of central Anatolia. As part of this project, 65 Streckeisen STS2 and Guralp CMG-3T broadband seismic stations were deployed in 72 locations throughout central Anatolia, which operated for two years between May 2013 and May 2015. The goals of the CD-CAT seismic deployment are multifaceted, but generally focus on better understanding the interplay between the complex Cenozoic evolution of the Central Anatolian Plateau and how it is reflected in the modern seismic structure of the region. In this study, we use P-wave receiver function images to investigate the crustal and uppermost mantle discontinuity structure beneath central Anatolia, and find links between crustal and upper mantle variations and Miocene-recent uplift and volcanism.

2-2- The Amalgamation of Anatolia

Anatolia has a long tectonic history of subduction and accretion of continental fragments that ends with the present-day westward extrusion and escape of the Anatolian plate. We briefly summarize the tectonics of central Anatolia by first describing the subduction/collision history followed by a brief description of the

present day structures that dominate deformation in Anatolia during its more recent history.

The crustal architecture of Anatolia is the result of the collision and accretion of continental fragments as crustal-scale nappes during the closure of the Neo-Tethys Ocean in the Cretaceous. These accreted crustal fragments are separated by sutures zones marked by ophiolite complexes and mélanges (Figure2-1). In the north, the Izmir-Ankara-Erzincan Suture Zone (IAESZ) demarcates the closure of the northern branch of the Neo-Tethys Ocean that separates the Pontides in the north from the Anatolide-Tauride and Kırşehir Blocks to the south (Şengör & Yılmaz 1981), while the Inner-Tauride Suture (ITS) separates the Kırşehir Block from the Anatolide-Tauride Block in central Anatolia. In general, the Anatolide-Tauride Block represents a Gondwanan-derived continental fragment comprising deformed and variably metamorphosed subduction-related rocks with higher-degrees of metamorphism in the north and west along the IAESZ and ITS. Away from the suture zones, deformation is characterized by fold and thrust belt formation and a lower degree of metamorphism, which occurred during the collision and accretion of this block during the Cretaceous to Eocene (Okay & Tüysüz, 1999). The Kırşehir block, composed of mainly Cretaceous-age high temperature metamorphic rocks and igneous intrusions (Göncüoğlu et al. 1991), is separated from the Anatolide-Tauride block along the more controversial ITS (Figure2-1). This suture zone is thought to represent the closure of a smaller ocean basin formed from rifting of the Gondwanan continental margin (Okay & Tüysüz, 1999; Whitney and Davis. 2006; Gürer et al., 2016), however, more recent work pointed out the lack of geologic evidence for late-Cretaceous subduction initiation along Inner-Tauride Suture (van Hinsbergen et al., 2016, Gürer et al., 2016). The triangular shaped Kırşehir Block (Figure2-1) which is also known as the Central Anatolian Crystaline Complex, is composed of mainly Cretaceous age high temperature metamorphic rocks and igneous intrusions (Whitney et al. 2003, Whitney and Hamilton 2004). The Anatolide-Tauride Block is composed of non-metamorphosed platform carbonates forming Tauride Mountains

in the south and metamorphosed passive margin sequences in the north (Okay 1984). In the Tauride Mountains at the southern margin of Anatolia, the older deformed rocks of the Anatolide-Tauride Block are overlain by late-Miocene platform carbonates. Further to the east, the Bitlis-Zagros Suture Zone represents the closure of the southern branch of the Neotethyan Ocean (Şengör and Yilmaz, 1981) that separated the Eurasian margin from the incoming Arabian Plate in the Oligocene. The structures imposed by the collision and accretion of these continental fragments play a significant role in controlling the more recent deformation of Anatolia by acting as zones of weakness that have in part been reactivated in response to a major change in the deformational character of the Anatolian region initiating in the Miocene.

2-3- Tectonic Structures of the Anatolian Plate

Today, the processes occurring along its southern margin mainly control the stress state of the Anatolian Plate. Despite the similar tectonic evolution of the Anatolian region prior to the Miocene, large lateral variations in crustal thickness, gravity, volcanism and geophysical properties in the Anatolian plate are observed (Vanacore et al., 2013; Ates et al., 1999; Mutlu & Karabulut 2011; Govers and Fichtner 2016). In the east, the collision of Arabia and Eurasia initiating in the Oligocene lead to largely compression-related deformational structures and seismicity (Şengör et al., 2008), while in the west, the southward migration of the Aegean trench presumably caused by slab rollback has led to regional-scale large magnitude extension and the exhumation of metamorphic core complexes since the early Miocene (Ring et al., 2010). Thus, the Miocene to recent evolution of Anatolia, and the structures along which deformation is localized, may exert an important control on the present-day seismic structure of the region.

Presently, the Anatolian Plate is defined by two conjugate strike-slip fault zones: the roughly W-E striking North Anatolian Fault Zone (NAFZ) that separates the Anatolian and Eurasian plates, which formed in the mid-Miocene in eastern Anatolia (Şengör et al., 2005), and the late Miocene - Pliocene NE-SW striking East Anatolian Fault Zone (EAFZ) that separates the Anatolian and Arabian or Eurasian plates (e.g. Şengör et al., 1985) (Figure2-1). These major neotectonic structures appear to exploit the lithospheric weaknesses created during the amalgamation of Anatolia, with the NAFZ roughly following the trace of the Izmir-Ankara-Erzincan Suture Zone (Şengör et al., 2005) and the EAFZ following the western portion of the Bitlis-Zagros Suture. Further to the south, the Dead Sea Fault Zone accommodates the differential motions of the Arabian Plate (~15 mm/yr northerly motion) and African Plate (~5 mm/yr northerly motion) with respect to Eurasia (Reilinger et al. 2006).

Central Anatolia represents the transition between the compressional deformation in the east and the highly extensional deformation of the Aegean in the west. Central Anatolia includes the Taurus Mountains, a high (>1.5 km) elevation mountain range that comprises most of the southern part of the Anatolide-Tauride Block in this region, and the Kırşehir Block (Figure2-2) (Şengör et al. 1985). Taken together this region has more recently been termed the Central Anatolian Plateau.

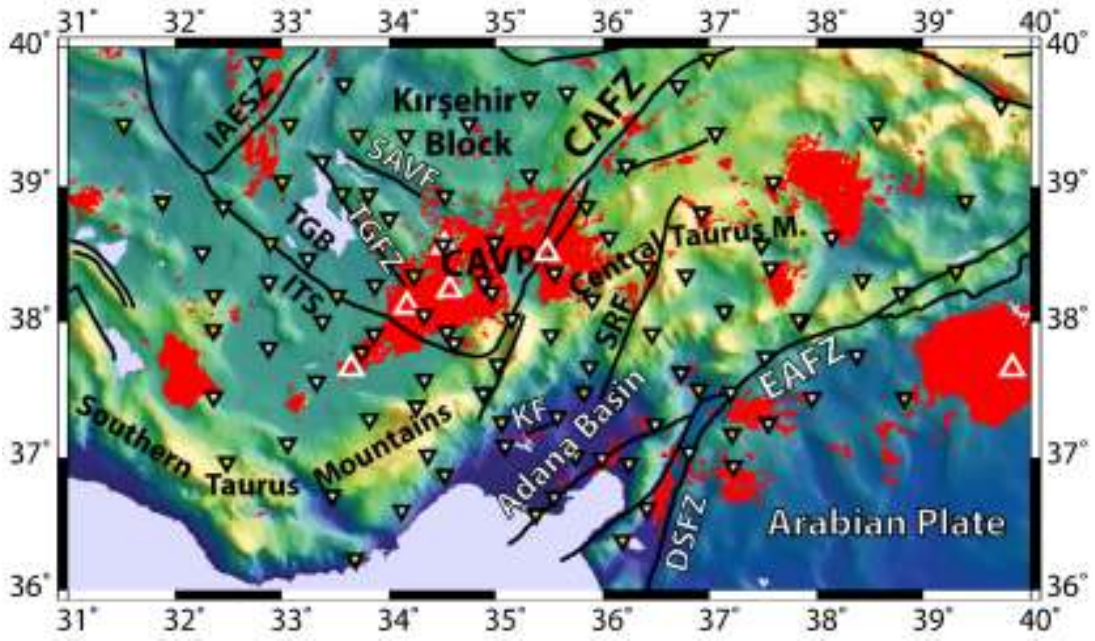

Figure 2-2: The topographic map of the study area showing key tectonic features (young volcanism, faults and suture zones) along with the location of seismic stations used in this study. White inverted triangles are, CD-CAT stations; yellow inverted triangles are KOERI stations; red polygons are Neogene-recent volcanic deposits; solid black lines are major structures and suture zones; white unfilled triangles are Holocene volcanoes. CAFZ: Central Anatolian Fault Zone; CAVP: Central Anatolian Volcanic Province; DSFZ: Dead Sea Fault Zone; EAFZ: East Anatolian Fault Zone; KF: Kozan Fault; SAVF: Savcılı Fault; SRF: Sarız Fault; TGB: Tuz Gölü Basin; TGFZ: Tuz Gölü Fault Zone.

The Central Anatolian Fault Zone (CAFZ) which in part appears to exploit the lithospheric-scale weakness of the Inner-Tauride Suture, separates the carbonate nappes of the Anatolide-Tauride Block from the highly deformed and metamorphosed rocks in the Kırşehir block (Figure2-2). The CAFZ is mainly a transtensional fault structure with low magnitude left-lateral offsets during the Miocene (Koçyığıt & Beyhan 1998); however, robust changes in Pn velocities and Bouguer gravity across the CAFZ between the Kırşehir and Anatolide-Tauride Blocks show distinctly different crust/upper mantle structures on either side of the CAFZ (Ates et al. 1999; Gans et al. 2009; Mutlu & Karabulut 2011). While up to 75

km total lateral displacement can be observed on some portions of the CAFZ, a recent geomorphological study shows a transition to W-E extension along the CAFZ near Mt. Erciyes since late Pliocene times (Higgins et al. 2015) leading to the development of a pull-apart basin that has been exploited by Miocene-recent volcanism of the Central Anatolian Volcanic Province (CAVP) (Toprak & Göncüoğlu 1993; Toprak 1998).

The Central Anatolian Volcanic Province can be characterized as a NE-SW trending (Figure2-2), middle-late Miocene to Holocene calc-alkaline to alkaline volcanic complex (Innocenti et al., 1975; Toprak, 1998; Toprak and Göncüoğlu, 1993; Piper et al. 2002; Aydın et al. 2012) that consists of pyroclastic deposits and lava flows, which apparently young from northeast to southwest (Scheiffarth et al., 2015). Recently, Aydın et al. (2014) identified Pleistocene bimodal volcanic activity in the southwestern part of the CAVP suggesting a transition from calc-alkaline to Na-alkaline composition at the latest phase of volcanism in agreement with recent contribution of asthenospheric mantle, as further verified by geochemical signatures in young (<2 My) primitive basalts intruded into the Anatolide-Tauride Block (Reid et al., 2017).

The Tuz Gölü Fault Zone (TGFZ) which is one of the major active transtensional structures in the region, is a right-lateral strike-slip fault zone with large normal component (Özsayın et al. 2013). This NW-SE trending fault zone juxtaposes the crystalline rocks of the Kırşehir Block and the thick sedimentary deposits of the Tuz Gölü Basin (Cemen et al. 1999), which obscures the surface trace of the Inner-Tauride Suture in the southwest (Figure 2-2). The Savcılı Fault, which is oriented in a WNW-ESE direction, developed during the Paleogene as a left-lateral transpressional structure accommodating vertical axis rotations; this has led to ~20 km lateral offset between the Mesozoic intrusive bodies of the Kırşehir Block (Lefebvre et al. 2013).

The East Anatolian Fault Zone (EAFZ) can be characterized as a broad (~20 km) left-lateral fault zone with a slip rate ~6 to 10 mm that bounds the westward-escaping Anatolian plate in the southeast (Bulut et al., 2012; Reilinger et al. 2006; Bozkurt 2001) (Figure 2-1). The East Anatolian Fault Zone initiated in the late Miocene-Pliocene and links to the North Anatolian Fault Zone at the Karlıova Triple Junction (Bozkurt 2001). To the south, the East Anatolian Fault Zone roughly follows the Bitlis-Zagros Suture between the Eurasian and Arabian plates and connects with the Dead Sea Fault, forming a triple junction between the Anatolian, Arabian and African plates (Figure 2-2). Further south, the East Anatolian Fault Zone branches into different faults towards the Adana Basin (Muehlberger and Gordon 1987). The Sarız fault, which is located between the CAFZ and EAFZ, is characterized by ongoing left-lateral strike-slip motion accommodating internal deformation across the Central Taurus Mountains (Kaymakçı et al. 2010).

The Adana Basin is a large, extensional Neogene basin along the southern margin of the Taurus Mountains (Figure 2-1). The transtensional Kozan Fault, which bounds the basin from north, is characterized by ~5 mm/yr left-lateral slip estimated from delta lobes (Aksu et al. 2014) and is considered the northernmost branch of the EAFZ that may have contributed some of the differential uplift between the Central Taurus Mountains and the Adana Basin (Aksu et al. 2005; Aksu et al. 2014; Radeff et.al, 2015).

Although much of the Anatolide-Tauride Block underwent folding and faulting and associated its accretion, recent results from the Topo-Europe indicate that along the southern margin of Anatolia, the Central Taurus Mountains have undergone two episodes of uplift since the late Miocene, leading to ~2 km of cumulative uplift based on biostratigraphic data from undeformed carbonate sequences (Cosentino et al. 2012; Schildgen et al. 2014; Radeff et al. 2015). This rapid uplift without evidence for Miocene shortening in the region has been interpreted as a result of

mantle processes including lithospheric delamination (Cosentino et al. 2012; Bartol & Govers 2014; Radeff et al. 2015) and/or processes associated with the breaking up of the downgoing African lithosphere (Schildgen et al. 2012; Schildgen et al. 2014). Based on teleseismic tomography, Biryol et al. (2011) suggested that the subducting Arabian oceanic lithosphere that was attached to the northern edge of the Arabian Plate has completely broken off, while the African/Tethyan lithosphere to the west is in the process of tearing and breaking apart as the African Plate moves northward and collides with the Anatolian margin.

2-4- Data and Methods

A total of 310 teleseismic events (distances between 30° and 95°) with magnitudes >5.5, recorded between May 2013 and May 2015 are used in our P-wave receiver function analysis (Figure 2-3). We used data from 72 broadband seismic stations that were part of the CD-CAT experiment and 26 Kandilli Observatory and Earthquake Research Institute (KOERI) stations in our analysis. The teleseismic earthquake distribution is dominated by events with backazimuths between 30° and 95° corresponding to Japan, Mariana, Ryukyu, Philippine, and Kuril trenches (Figure 2-3). In order to increase our backazimuthal coverage to ensure results are not spatially biased, we incorporate PP receiver functions (e.g. Frassetto et al. 2011) from 190 events > 6 M with epicentral distances of 95° – 180° from our network. As South America falls in this distance range, it allows us to densely sample the southwestern backazimuth of our study area. In order to avoid any interference from the arrival of PKS phases on the radial component, events with distances between 137° to 152° (distances where the PKS phase will arrive within 50 seconds of PP) are omitted.

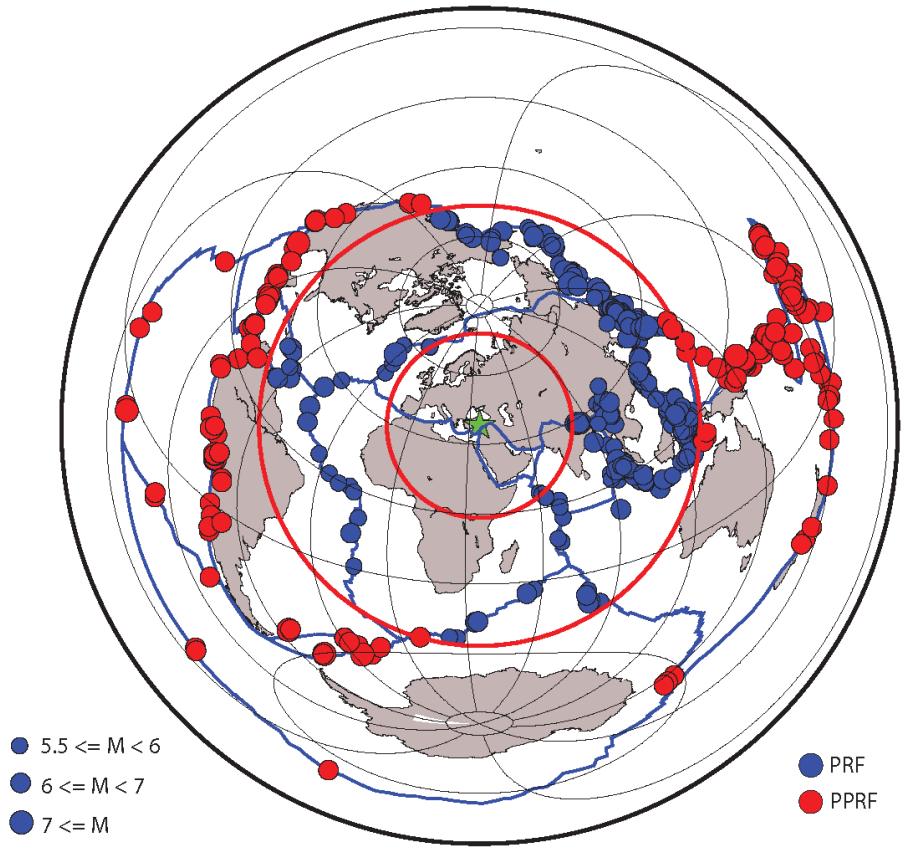

Figure 2-3: Global distribution of events used in our receiver function analysis. Blue circles represent events used for P-wave receiver functions (30 – 95 degree epicentral distances) and red circles represent events used for PP receiver functions (>95 degree epicentral distances). Red circles show 30 and 95 degrees distance from the center of the network shown by green star.

Receiver functions are very sensitive to impedance contrasts beneath a station, allowing us to gain insight into the magnitude of velocity changes across discontinuities. Large impedance contrasts over a short depth interval will be expressed as a high amplitude Gaussian pulse over a short time interval; conversely low amplitudes pulses over long time intervals correspond to velocity gradients. For both P and PP events, we perform a time-domain iterative deconvolution (Ligorria &

Ammon 1999) on vertical and radial component data filtered between 0.07 and 3 Hz to compute P-s receiver functions with a 2.5 Gaussian pulse width corresponding to 1.2 Hz center frequency (~1 km vertical resolution with considering average crustal shear velocities). For quality control, we first inspect each event-station pair, and those without a clear P or PP arrival are discarded. Then, calculated receiver functions with a low variance reduction (less than 0.7) are discarded along with anomalous receiver functions. For the final QC step, we use the Funclab software (Eagar & Fouch, 2012) to visually inspect the calculated receiver functions.

2-4-1- Calculation for Crustal Thickness and *Vp/Vs*: Stack Windowing Analysis

The migration of receiver function to depth requires information on the *Vp/Vs* ratio of the crust and uppermost mantle. By identifying multiples from the Moho Ps conversion in receiver functions, the *Vp/Vs* ratio of the crust beneath a station can be determined. *H-κ* stacking (Zhu & Kanamori, 2000) is a simple and automated way to measure crustal thickness (H) and *Vp/Vs* ratios (κ) through the summation of the primary (Ps) conversion from the Moho and its associated multiples (PpPs and PsPs + PpSs, respectively) assuming flat-lying homogeneous layers, However, the effectiveness of *H-κ* stacking diminishes in tectonically complex regions, when the assumption of flat, homogeneous layering breaks down, leading to difficulty in identifying the correct crustal thickness and *Vp/Vs* (Figure 2-4). Thus, we prefer a more manual method for identifying the multiples from the Moho discontinuity in tectonically complex areas, which we call Stack Windowing Analysis (SWA).

SWA builds on previous approaches in estimating κ through the manual picking of the Ps conversion and the PpPs multiple (Zandt and Ammon, 1995). Since single

earthquake traces can be contaminated with noise, we stack all receiver functions at an individual station to increase the signal-to-noise ratio of the data after normalizing the amplitude of a trace and correcting for moveout. We then choose a time window around the Ps and PpPs arrivals on the stacked trace, with the maximum amplitude in the time window being automatically chosen as the conversion of interest. From these times, we can calculate κ and H as follows (Zandt and Ammon, 1995):

$$\kappa = \sqrt{\left(1 - \rho^2 {V_p}^2\right)\left(\frac{2T_{Ps}}{T_{PpPs} - T_{Ps}} + 1\right)^2 + \rho^2 {V_p}^2}$$

$$H = \frac{T_{Ps} * Vp}{\kappa * \sqrt{1 - \rho^2 \left(\frac{V_p}{\kappa}\right)^2} - \sqrt{1 - \rho^2 {V_p}^2}}$$

where V_p is an assumed value for average P-wave velocity in the crust (6.1 km/sec in this study) that generally has a small effect on overall crustal thickness estimates (Zhu & Kanamori, 2000), ρ is an arbitrary ray parameter, but should be the same as the ray parameter used to correct for moveout in the stacking routine, and T_{ps} and $T_{PpPs}$are the time picks from the stacked receiver function at a station of interest. Errors are then estimated by comparing the chosen arrivals from the stacked trace with time of the maximum amplitudes in the chosen time window on individual traces by taking the standard deviation of the time differences. Using this uncertainty in a standard propagation of errors calculation, we can estimate errors in κ and H as follows:

$$\Delta\kappa = \sqrt{\left(\frac{\partial\kappa}{\partial T_{Ps}}\Delta T_{Ps}\right)^2 + \left(\frac{\partial\kappa}{\partial T_{PpPs}}\Delta T_{PpPs}\right)^2}$$

$$\Delta H = \sqrt{\left(\frac{\partial H}{\partial T_{Ps}}\Delta T_{Ps}\right)^2 + \left(\frac{\partial H}{\partial\kappa}\Delta\kappa\right)^2}$$

Where Δ is the standard deviation of the measurement. This technique, while requiring more interaction than H-κ stacking, allows for an improved recovery of both crustal thickness and *Vp/Vs* ratios where traditional *H-κ* stacking analysis may struggle, while obtaining very similar results in areas of simple crustal structure (Figure 2-4).

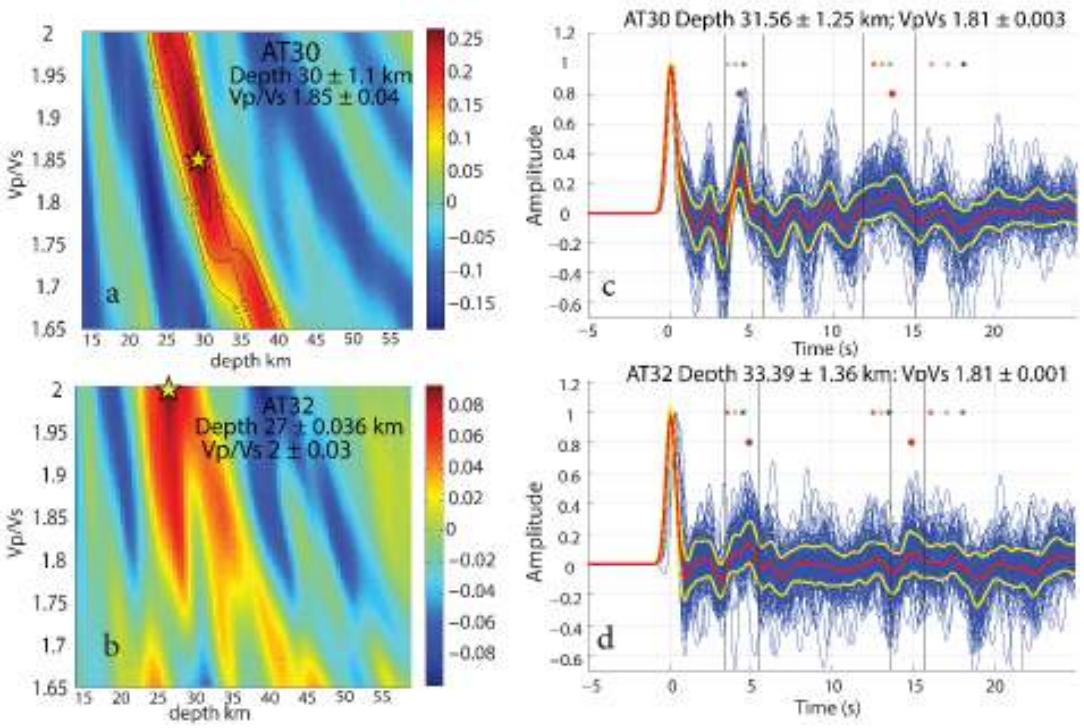

Figure 2-4: Comparison between H-k Stacking Analysis and Stack Windowing Analysis (SWA) for two stations. A) H-k result for station AT30 representing a good H-k solution. B) H-k results for station AT32 representing poor H-k solution. C) SWA result for station AT30 showing good agreement with H-k method. D) SWA result for station AT32 showing that a good result can be found without having to modify H-k parameter search space. Red, green and black asterisks represent the expected times of Ps and its first and second multiples with 35km crustal thickness and 1.7, 1.8 and 1.9 Vp/Vs ratios respectively. Red dot shows the time of the maximum amplitude of the stacked receiver function in selected time window.

2-4-2- Adaptive Common Conversion Point (CCP) Stacking

In order to resolve spatial variability in the crust and uppermost mantle, we utilize CCP Stacking Analysis (Dueker & Sheehan 1997) to create a 3D volume of receiver function amplitude. In this analysis, the region of interest is gridded into bins based on user defined width and spacing. Receiver functions are migrated to depth and ray-traced back to their theoretical locations in the Earth, and receiver function amplitudes that fall within the same bin are averaged to represent the structure in that bin. To compute the theoretical ray paths in our dataset, we use a regional 1D velocity model derived from the shear wave velocity model of Delph et al. (2015a), which comprises a Vs = 3.4 km/s crust and Vs = 4.2 km/s mantle with a constant *Vp/Vs* ratio of 1.78 and crustal thickness of 38 km. Although this 1D velocity model doesn't account for the variability in crustal thicknesses and velocities throughout our region, the differences that arise in ray tracing receiver functions to obtain piercing points based on a 1D model as opposed to a 3D model are very minor, especially in the crust. However, variability in *Vp/Vs* can have a significant effect on the depth to discontinuities (Zhu & Kanamori 2000). We account for these lateral variations in velocity structure by creating a 3D velocity model that applies timing corrections to the ray-traced receiver functions so that conversions are mapped to their proper locations at depth (Eagar et al. 2010). Boundaries in this 3D velocity model are derived from the crustal thickness and *Vp/Vs* results from SWA in this study (Figure2-4) and the average shear wave velocities in the crust from Delph et al. (2015a). For the mantle, a Vs of 4.2 km/s was assumed based on the results of Delph et al. (2015a) and Fichtner et al. (2013) with a constant *Vp/Vs* of 1.78. In order to maximize spatial resolution in this study, we follow the adaptive common conversion point approach of Delph et al. (2015b), which allows our bin width to dilate from 0.3 to 1 degree until each bin has at least 10 rays.

2-5- Results

By investigating the crustal thickness and *Vp/Vs* results from SWA (Figure 2-5), conversion amplitudes (Figure 2-6), and cross-sections generated from adaptive CCP stacking analysis (Figure 2-7), we can gain insight into the characteristics of the crust and crust-mantle boundary throughout central Anatolia.

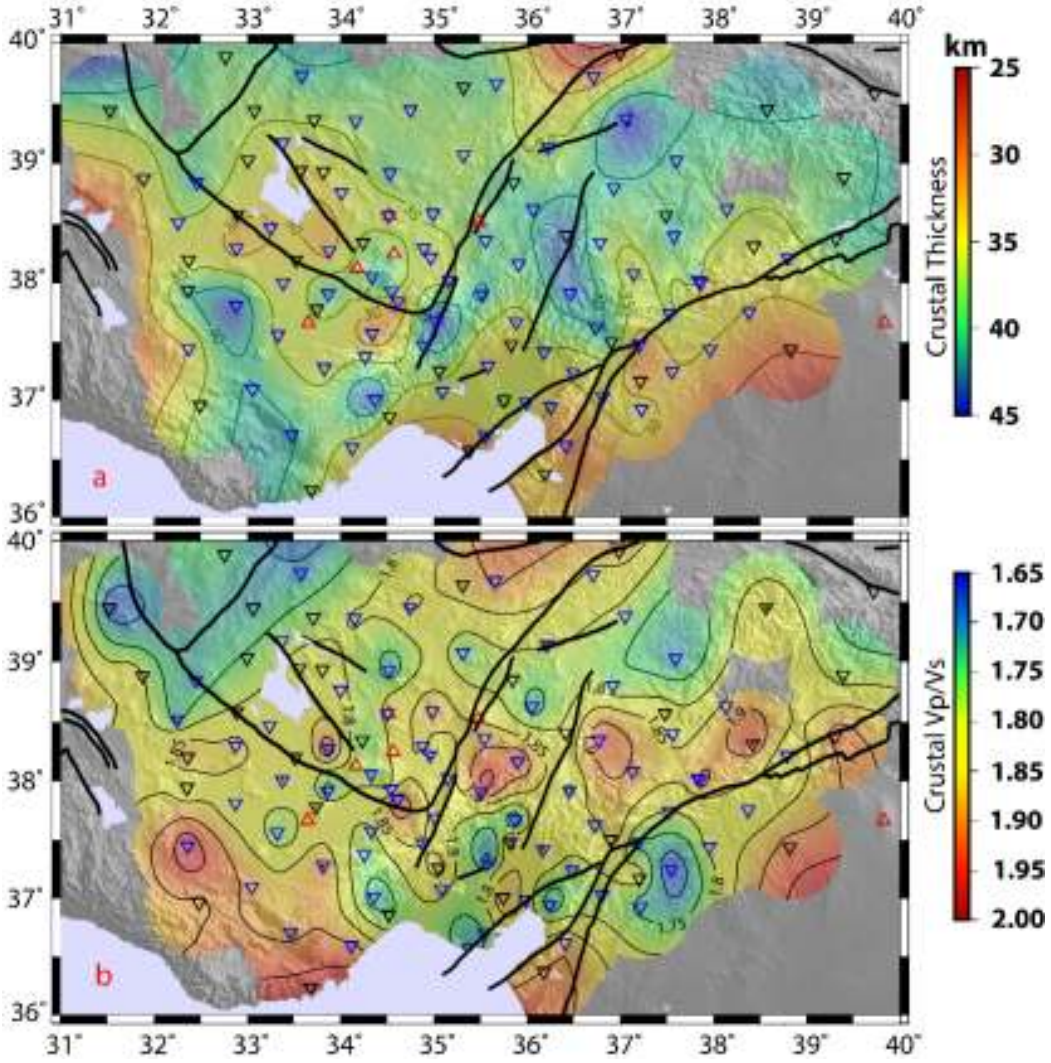

Figure 2-5: Results of Stack Windowing Analysis for (a) Crustal thickness and, (b) bulk crustal Vp/Vs. Red triangles are Holocene volcanoes; blue and black triangles are seismic stations; black bold lines are major tectonic structures; solid thin lines are contour intervals

Crustal thickness estimates throughout the region are variable and correlate well with tectonic structures (Figures. 2-5a and 2-7). The thickest crust in the region corresponds with the eastern Taurus Mountains, where crustal thickness estimates are generally high (>40 km) with values reaching up to 45 km (Figures. 2-5a and 2-7c). The Adana Basin to the south of the Taurus Mountains is characterized by thin crust (<35 km) with measurements as low as 25 km, indicating crustal thickness changes of up to 15 km over ~60 km lateral distance (Figures. 2-5a and 2-7d). A similar relationship is seen on the southwestern margin of the Kırşehir block, where crustal thicknesses are as low as 30 km (Figure 2-5a) in the Tuz Gölü Basin. Thin crust (~30 km) also characterizes the Anatolian Plate near the EAFZ and the Arabian plate. In the Central Anatolian Volcanic Province and much of the Kırşehir Block, crustal thickness ranges from 35-40 km (Figure 2-7e).

The estimates of bulk crustal *Vp/Vs* values are variable but show some apparent trends (Figure 2-5b). To first order, the thick crust (>40 km) beneath the Taurus Mountains are associated with elevated *Vp/Vs* ratios (>1.85) (Figure 2-5b). In contrast, the CAVP exhibits slightly lower *Vp/Vs* (1.75-1.8) values (Figure 2-5b) suggesting that the effect of Neogene volcanism to bulk *Vp/Vs* of the crust is rather limited. The Adana basin is also characterized by low *Vp/Vs* (<1.8) values except in the east near the young mafic volcanics, which coincides with a high *Vp/Vs* (>1.85) anomaly, (Figure 2-5b). The lowest *Vp/Vs* ratios (~1.7) are found along the IAESZ near the northwestern Kırşehir Block (Figure 2-5b), possibly reflecting higher SiO_2 content as silica inversely correlates with *Vp/Vs* ratio (Christensen 1996).

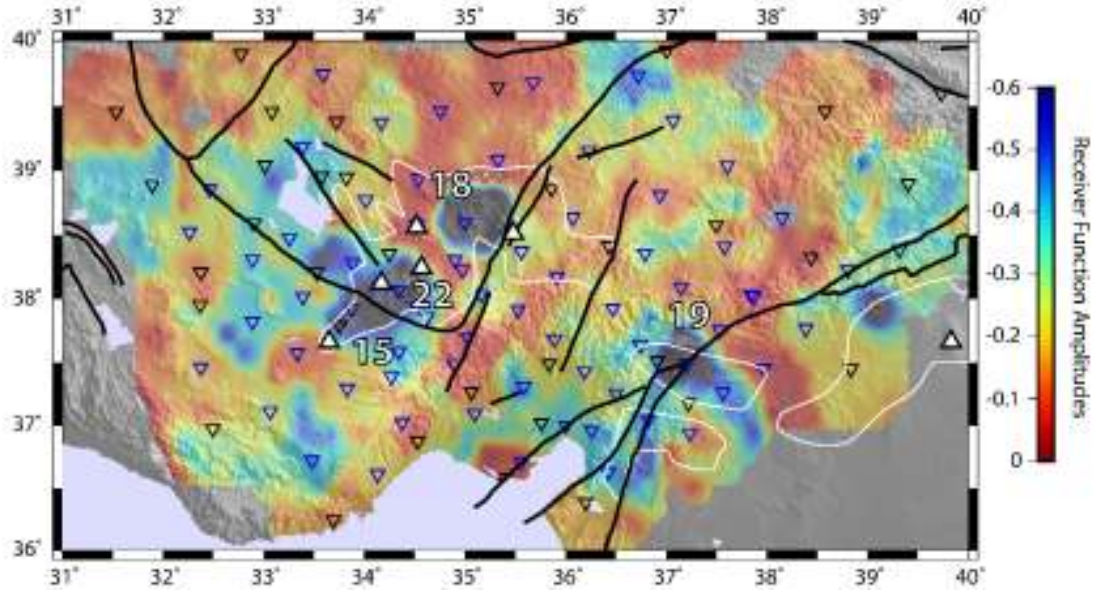

Figure 2-6: Negative receiver function amplitudes between 10 and 30 km below surface normalized to coherence peak from CCP stacking. Cold colors indicate regions with large magnitude negative arrivals, possibly indicative of the presence of fluids/melts in the crust. Depth to maximum negative amplitude shown by white numbers. Black lines show major tectonic structures and sutures; white lines indicate outlines of the Neogene to recent volcanic deposits; blue/black inverted triangles are CD-CAT and KOERI stations; white triangles are Holocene volcanoes.

Through the investigation of conversion amplitudes in receiver functions, we can gain insight into the relative impedance contrast in the crust. We observe high negative conversions in the mid-crust in 2 distinct regions: 1) near the boundary of the Anatolian and Arabian plates near the EAFZ (Figures. 2-6, 2-7c and 2-7d), 2) along the Central Anatolian Volcanic Province, where the southern anomalies show an apparent offset across Tuz Gölü Fault Zone (from 22 to 15 km; Figures. 2-6, 2-7a and 2-7b). These anomalies are further discussed below.

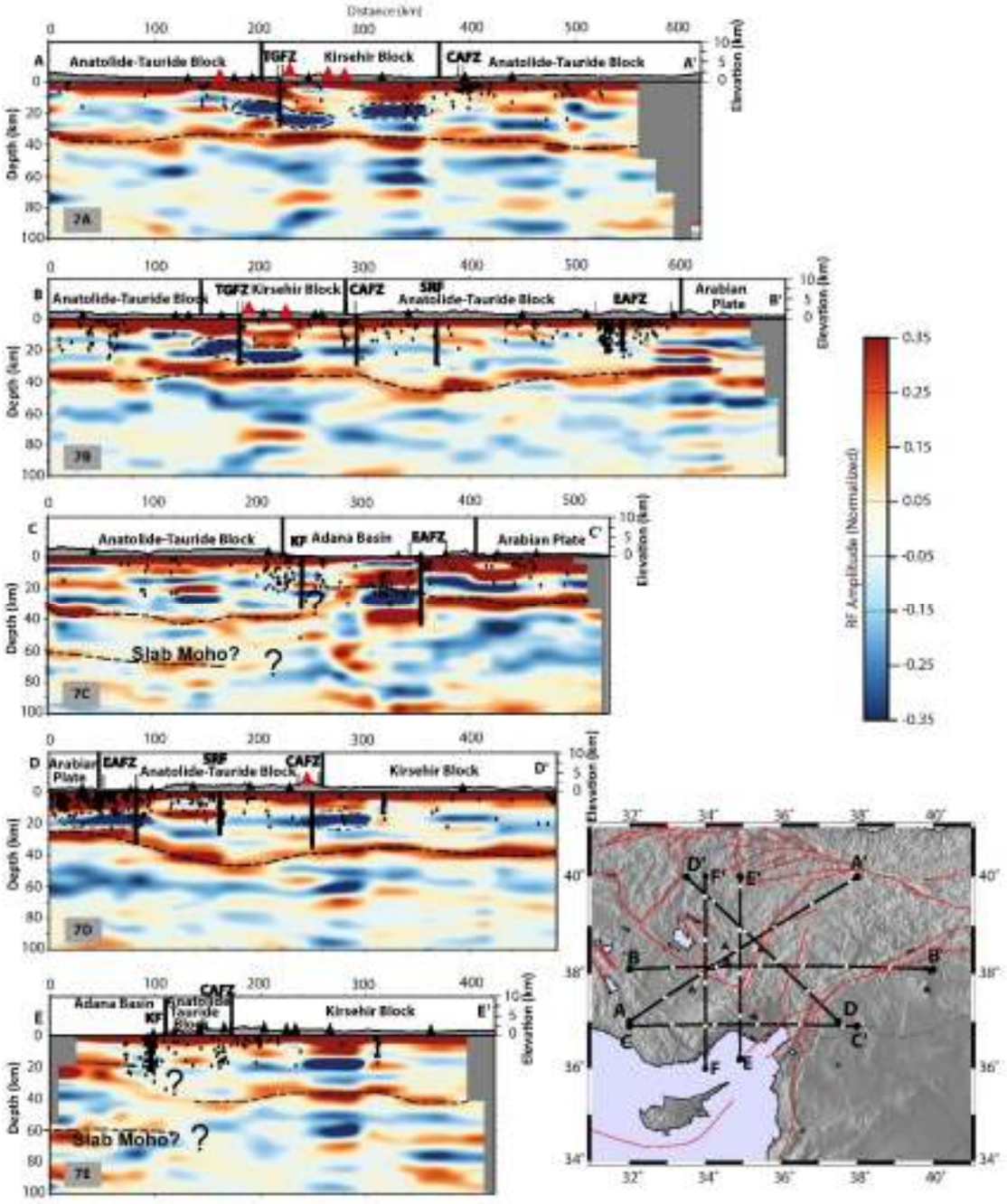

Figure 2-7: (a-e): CCP stacks throughout central Anatolia with 150% vertical exaggeration and location map of these sections (on the right). On the cross-sections, black lines represent the terrane/plate boundaries or major faults; dashed lines represent the continental Mohorovičić (Moho) discontinuity; black dots represent the relocated earthquakes across the region taken from Turkelli et al. (2015). TGFZ, Tuz Gölü Fault Zone; CAFZ, Central Anatolian Fault Zone; EAFZ, East Anatolian Fault Zone; KF, Kozan Fault; SRF, Sarız Fault. Note that the cross-section FF' is shown in Figure2-8

2-6- Discussion

2-6-1- Nature of Crustal Boundaries in the central Anatolia

A rapid change in crustal thickness corresponds to the location of the East Anatolian Fault Zone and Bitlis-Zagros Suture (Figures. 2-7c and 2-7d). While it is difficult to know whether this crustal thickness variation is due to the evolution of the East Anatolian Fault Zone or reflects the juxtaposition of the Arabian lithosphere against more deformed and thickened Anatolian lithosphere, these variations extend further east than the East Anatolian Fault Zone along the Bitlis-Zagros Suture (e.g., Özacar et al., 2010). Thus, it is likely that these variations are due to the collision of Arabia with Eurasia, generating thicker crust north of the suture zone, rather than transform movement along the East Anatolian Fault Zone. However, as convergence between Arabia and Eurasia proceeded, this variation in crustal thickness may have served as a boundary along which stress could be localized, leading to the development of the East Anatolian Fault Zone in Pliocene times as a lithospheric-scale transform fault controlling tectonic escape of the Anatolian Plate. In central Anatolia, the Moho beneath the Tuz Gölü Fault Zone seems to be continuous, while the low velocity layers at mid-crustal depths are offset, indicating that the Tuz Gölü Fault represents a tectonic structure limited to the upper-mid crust (Figures 2-7a and 2-7b).

A large decrease in crustal thickness also occurs at the transition from the Taurus Mountains (>40 km) into the Adana Basin (~30 km) over a relatively short lateral distance (~60 km). This pronounced crustal thinning corresponds to the Kozan Fault, which is thought to be a transtensional splay fault of the EAFZ (Aksu et al. 2014). However, the identified motion on the Kozan Fault is not sufficient to accommodate the 2 km uplift of the Taurus Mountains since the late Miocene. According to the depth contours of subducting African lithosphere extracted from teleseismic tomography (Biryol et al. 2011), the Adana basin is located east of the Cyprus slab in

an area where no subducting lithosphere is imaged, suggesting minimal sensitivity to processes related to slab dynamics. In addition, the Adana basin was located at the leading edge of the fold and thrust belt, experiencing limited crustal thickening compared to the over thickened crust of the Anatolide-Tauride Block. We interpret the Adana Basin as a diffuse transtensional plate boundary between the Anatolian and African plates which was likely formed as a piggy back basin.

Across the eastern segment of the Inner-Tauride Suture that spatially coincides with a portion of the Central Anatolian Fault Zone, a thinning of the crust in the Kırşehir Block/Tuz Gölü Basin is observed (Figures2-5a, 2-7b, 2-7d and 2-7e). Many previous geophysical studies have found drastic changes in various geophysical properties (e.g. Bouguer gravity anomaly, Ates et al. 1999; Pn velocities, Gans et al. 2009; shear wave velocities, Warren et al. 2013 and Delph et al. 2015a). We interpret the differences in geophysical characteristics on either side of the suture to reflect these observed differences in crustal thickness rather than previous interpretations that the upper mantle is slower to east of the Inner-Tauride Suture than to the west (Gans et al., 2009). To the west, the crust of the Tuz Gölü Basin and the southern Kırşehir Block is relatively thin (~30 km), thickening gradually to the northeast. As this thin crust crosses the inferred location of the Inner-Tauride Suture, it indicates that the true location of the Inner-Tauride Suture, at least in the lower crust, may be located further to the northeast near the surface trace of the Tuz Gölü Fault.

2-6-2- Low Velocity Zones in the Central Anatolian Volcanic Province

We observe multiple large, negative amplitude conversions beneath most of the Central Anatolian Volcanic Province indicative of the presence of a velocity decrease with depth (Figure2-6). The top of the velocity decrease is shallower

beneath the Anatolide-Tauride Block (15 km) than it is beneath the Kırşehir Block (22 km) (Figures2-6, 2-7a and 2-7b). The northern anomaly beneath the Central Anatolian Volcanic Province at 18 km depth is the largest negative amplitude anomaly (Figures2-6 and 2-7a), and correlates well with the inferred centers that fed the eruptions of large ignimbrite deposits throughout central Turkey (Aydın et al. 2012). If these low velocity layers are associated with crustal melt that is sourcing the Central Anatolian Volcanic Province, we might expect high *Vp/Vs* ratios in the region. However, the bulk crustal *Vp/Vs* ratios are not consistent with a substantial amount of melt in this area (~1.75), suggesting that if these velocity decreases represent the presence of partial melts, they must be confined to relatively thin layers (Figure2-5b). The negative anomaly located near the boundary of the Anatolian and Arabian plates at a depth of 19 km (Figure2-6) also correlates well with the recent small-volume mafic volcanic activity (Rojay et al. 2001), and may represent a mafic sill that has stalled in the crust.

2-6-3- Uplift of the Central Taurus Mountains

Schildgen et al. (2014) identified multiple episodes of uplift of the Central Taurus Mountains along the southern margin of the Central Anatolian Plateau initiating in the late Miocene-Pliocene and followed by a late Pliocene-early Pleistocene episode of faster uplift that may be related to the arrival of the Eratosthenes Seamount along the subduction margin near Cyprus (Schildgen et al. 2012a). These events are consistent with uplift observed in Cyprus, which shows uplift similar in magnitude and timing to what has occurred in the Central Taurus Mountains (~2 km of uplift in the last ~6 Ma; Morag et al., 2016). The proposed mechanisms for this uplift are generally related to slab break-off. Originally, Cosentino et al., (2012) proposed that the upwelling of asthenosphere after slab break-off was responsible for the uplift, while Schildgen et al., (2012, 2014) later interpreted that some of the uplift could be

attributed to the topographic response of slab break-off (e.g., Duretz et al., 2011) without requiring the influx of asthenosphere to support the elevations of the Central Taurus Mountains.

Our results show a good correlation of crustal thickness and elevation in the Taurus Mountains (Figure2-5a). The Central Taurus Mountains have average elevations of ~1.5-2.0 km and a crustal thickness of ~40 km. While Airy isostasy depends on assumptions made about crustal and upper mantle density that are generally not well constrained, these crustal thicknesses and elevations are consistent with an isostatically compensated crust. Also, the presence of a fast seismic velocity anomaly in the uppermost mantle beneath the Central Taurus Mountains, interpreted as representing the subducting African lithosphere (Bakırcı et al., 2012) indicates that the presence of asthenosphere beneath the Central Taurus Mountains is unlikely. Consistent with this fast velocity anomaly, we observe a weak positive amplitude conversion at depths ~65 – 80 km beneath the Central Taurus Mountains that spatially corresponds to the top of the slab imaged by Bakırcı et al. (2012) (Figures2-7c, 2-7e and 2-8). This discontinuity can be traced to the northern edge of the Central Taurus Mountains, and disappears abruptly near the southernmost extension of the Central Anatolian Volcanic Province, which displays young volcanism with geochemical characteristics consistent with asthenospheric input (Reid et al., 2017) (Figure2-8). The dip of this discontinuity is subhorizontal, indicating the shallow, aseismic underthrusting of the African lithosphere. At greater depth, the Cyprus slab appears segmented in the teleseismic P wave tomography images, suggesting that the slab is currently in the process of detachment beneath central Anatolia (Biryol et al. 2011).

Based on these results, the fast shear velocities imaged beneath the Central Taurus Mountains (Bakırcı et al., 2012), and the geochemical signatures indicating an input of asthenospheric material immediately to the north in the CAVP (Reid et al., 2017),

we propose that rollback of the Cyprus slab initiated by at least mid-Miocene times as indicated by extensional exhumation in the Kırşehir Block (Whitney and Dilek 1997, Whitney et al. 2003, Fayon and Whitney 2007) and the initiation of volcanism in the Central Anatolian Volcanic Province (Le Pennec et al., 1994; Aydar et al., 2012), Because of this rollback, the Central Taurus Mountains subsided due to the increased load of a vertically dipping slab, allowing for the deposition of Late Miocene marine sediments. In the late Miocene-Pliocene, the Central Taurus Mountains were characterized by thick crust most likely uplifted to attain isostatic balance. The segmentation of the Cyprus slab accelerated probably just after the collision of Eratosthenes Seamount with the ongoing African subduction and resulted in recent slab break-off, followed by slab rebound and subsequent rapid late Pliocene-early Pleistocene uplift in the overriding plate (Buiter et al. 2002, Duretz et al. 2011) which has formed the modern topography of the southern margin of the Central Anatolian Plateau (Figure2-8). This slab roll back and final break-off would create space for the upwelling of asthenospheric material to reach the base of the lithosphere beneath central Anatolia, leading to the geochemical signatures volcanism found in the CAVP (Reid et al., 2017).

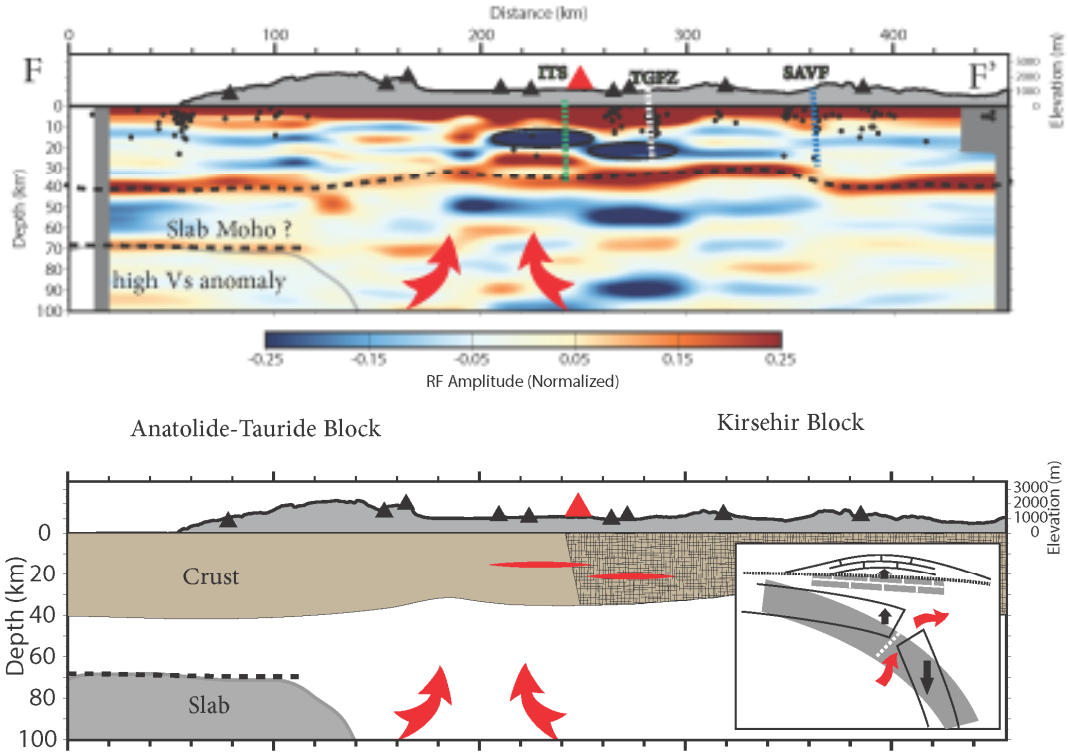

Figure 2-8: CCP stack cutting through Taurus Mountains and CAVP (transect F-F' shown in the location map of Figure2-7) and its interpreted section. Volcanism and high elevations of the Central Anatolian Plateau could be associated with the influx of asthenosphere around the edge of the African lithosphere. ITS, Inner Taurid Suture; SAVF, Savcılı Fault; TGFZ, Tuz Gölü Fault Zone. Red and black triangles are the projection of nearby Holocene volcanoes and seismic stations onto the cross-section respectively. Red lines indicate the top of the low velocity zones in the crust. Red curved arrows show the upwelling asthenospheric material. The slab is taken from surface wave tomography (after Bakırcı et al. 2012). Inset: Grey colors represent the position of the slab and Taurus marine carbonates before the slab break-off and black lines outline their positions after the slab break-off.

2-7- Conclusion

This study uses recently acquired seismic data from the CD-CAT seismic deployment to produce the highest-resolution images of crustal variability in central Anatolia to date. Overall, we data from 500 teleseismic events recorded by 92

broadband seismic stations for the calculation of P and PP receiver functions. We analyze crustal thickness and *Vp/Vs* ratios for this dataset using Stack Windowing Analysis (SWA), which represents an interactive alternative to *H-k* Stacking Analysis in tectonically complex regions. Additionally, we utilize adaptive CCP Stacking Analysis to generate an amplitude volume representing depths to impedance contrasts that allows us to gain insight into the lateral seismic variations of the crust and upper mantle in central Anatolia.

Our main findings are summarized as follows:

1) Crustal thickness measurements correlate well with high elevations supporting isostatically compensated crust. The thickest crust is found in the Taurus Mountains (>40 km), and crustal thicknesses decreased rapidly to the south in the Adana Basin (<35 km) and Arabian Plate (~30 km), and to the northwest beneath the Tuz Gölü Basin (~30 km) and the Kırşehir Block (35-40 km).

2) Bulk Vp/Vs estimates are highly variable in the region. Generally, high Vp/Vs ratios (>1.85) are observed across the Taurus Mountains, while lower Vp/Vs ratios (~1.7) are observed along the IAESZ that bounds the Kırşehir Block to the northwest.

3) Multiple low velocities zones displaying large negative impedance contrasts are observed between 15 and 25 km depth near the EAFZ and beneath the CAVP and may correspond to mid-crustal magma reservoirs feeding surface volcanism.

4) A gently-dipping positive amplitude anomaly interpreted as the Moho of the underthrusting African lithosphere lies between 65 and 80 km depth

beneath the Central Taurus Mountains. This anomaly abruptly ends just south of the CAVP, where young volcanism shows geochemical indicators for asthenospheric input in agreement with slab break-off and subsequent rebound coeval with the onset of late Pliocene-early Pleistocene rapid uplift rising the late Miocene marine sequences ~2 km above the present day sea level.

CHAPTER 3

CRUSTAL STRUCTURE ACROSS THE CENTRAL SEGMENT OF THE NORTH ANATOLIAN FAULT ZONE AND ITS RELATION WITH OLD SUTURES: NEW CONSTRAINTS FROM RECEIVER FUNCTIONS

The North Anatolian Fault Zone (NAFZ) is an active continental transform plate boundary that accommodates the westward extrusion of the Anatolian plate. The central segment of NAFZ displays northward convex surface trace which coincides partly with the old suture zones. The depth extent of NAFZ and detailed structure of the actively deforming crust in the region is still under much debate. Moreover, the locations of existing terrane boundaries in the subsurface and processes responsible from rapid uplift are yet to be addressed. In this study, over five thousand high quality P receiver functions are computed using teleseismic earthquakes recorded by permanent stations of national agencies and temporary North Anatolian Fault Passive Seismic experiment (2005-2008). According to our results, nature of discontinuities and crustal thickness display sharp changes across the main strand of NAFZ supporting a lithospheric scale faulting that offsets Moho discontinuity. In the southern block, crust is relatively thin in the west (~35 km) and becomes thicker gradually towards east (~40 km). In contrast, the northern block displays a sharp crustal thinning reaching up to 10 km towards east across a narrow roughly N-S oriented zone which is interpreted as the subsurface signature of the ambiguous terrane boundary most likely separating Central and Eastern Pontides.

3-1- Introduction

North Anatolian Fault Zone (NAFZ) is one of the most famous strike-slip plate boundaries which is analogues in some features to the San Andreas fault zone in western US, however, is much younger. It is developed due extrusion of the Anatolian plate resulting from northward progression of the Arabian/ African plates (e.g. Şengör et al. 2005) and alongside with the East Anatolian Fault zone (EAFZ) are the major boundaries accommodating the escape of the Anatolian plate. West-northwest is the dominant trend of this fault zone in the east which turns toward west-southwest in the western segments and shows northward convex in the central part (Figure 3-1a). This curved fault trend correlates well with the rotational motion between Anatolian and Eurasian plates with Euler pole located near the coastal region of Egypt (Le Pichon & Kreemer 2010) which fits the dense GPS measurements (McClusky et al., 2000,Reilinger et al. 2006). NAFZ extends for about roughly 1500 km from Karliova junction in the east to Gulf of Saros in the Aegean Sea in the west (Yolsal et al. 2011). Several devastating earthquakes are recorded in this zone in different periods of time which show a westward propagation pattern and recurrence time of ~200-400 years (Barka 1996, Stein et al. 1997, Ambraseys 2002). The scattered earthquake activity along the NAF and the abundance of off-fault seismicity might be an indication of its young age and geological and structural complexity.

NAFZ alongside with old sutures formed during the closure of Neotethys ocean are shaping the seismotectonic setting of the region which is affected in the past by amalgamation of several terranes (Şengör 1984, 1989, 1990a; Şengör & Natal'in 1996). Pontides which is the main component of northern Turkey has a long and complex evolution history including multiple orogenic events, the Cimmerides and Alpides. The Cimmerides, in fact is the closure of the Paleo-tethys which caused the

collision of the Cimmerian continent to the southern Laurasia. In the back arc, the Neotethys started to develop and finally the closure of this ocean resulted in the collision of Pontides and Anatolide-Tauride block (Yılmaz et al. 1997). The Central Pontides is located around the northward convex central segment of NAFZ and in fact act as a knot connecting the Western and Eastern Pontides.

Western Pontides composed of different zones including Sakarya continent, Istanbul-Zonguldak and Armutlu-Almacık zones and Istranca massif. Eastern Pontides is composed of several parallel belts which have east-west extensions (Yılmaz et al. 1997). The Istanbul-Zonguldak zone which was a south facing passive margin of Laurasia continent is an exception in the Pontides (Yılmaz et al. 1997). This zone is bounded from the south by the Intra Pontide Suture (IPS) which coincides with the NAFZ in the west. Okay et al. (1994) defined this zone as the İstanbul terrane that moved south along two large transform faults (West Black Sea and West Criminean faults) opening the West Black Sea Basin (Figure 3-1a). Recently, Nikishin et al. (2015) suggested existence of another major wrench fault between the Central Pontides and the Eastern Pontides (Figures 3-1b). Actual position of so called Abana Fault is still enigmatic but assumed to be bounding the Central Pontides from east.

In this study, seismic data acquired by the temporary seismic network, the NAF experiment (Beck and Zandt 2005, Biryol et al 2010) and permanent stations of national agencies are used for teleseismic P receiver function analysis to elucidate the current configuration of crust beneath the central segment of NAFZ. Using the common conversion point (CCP) bin picking method which developed during this study, crustal thickness and Vp/Vs variations are identified and high resolution images of the crustal discontinuities are constructed for interpretation.

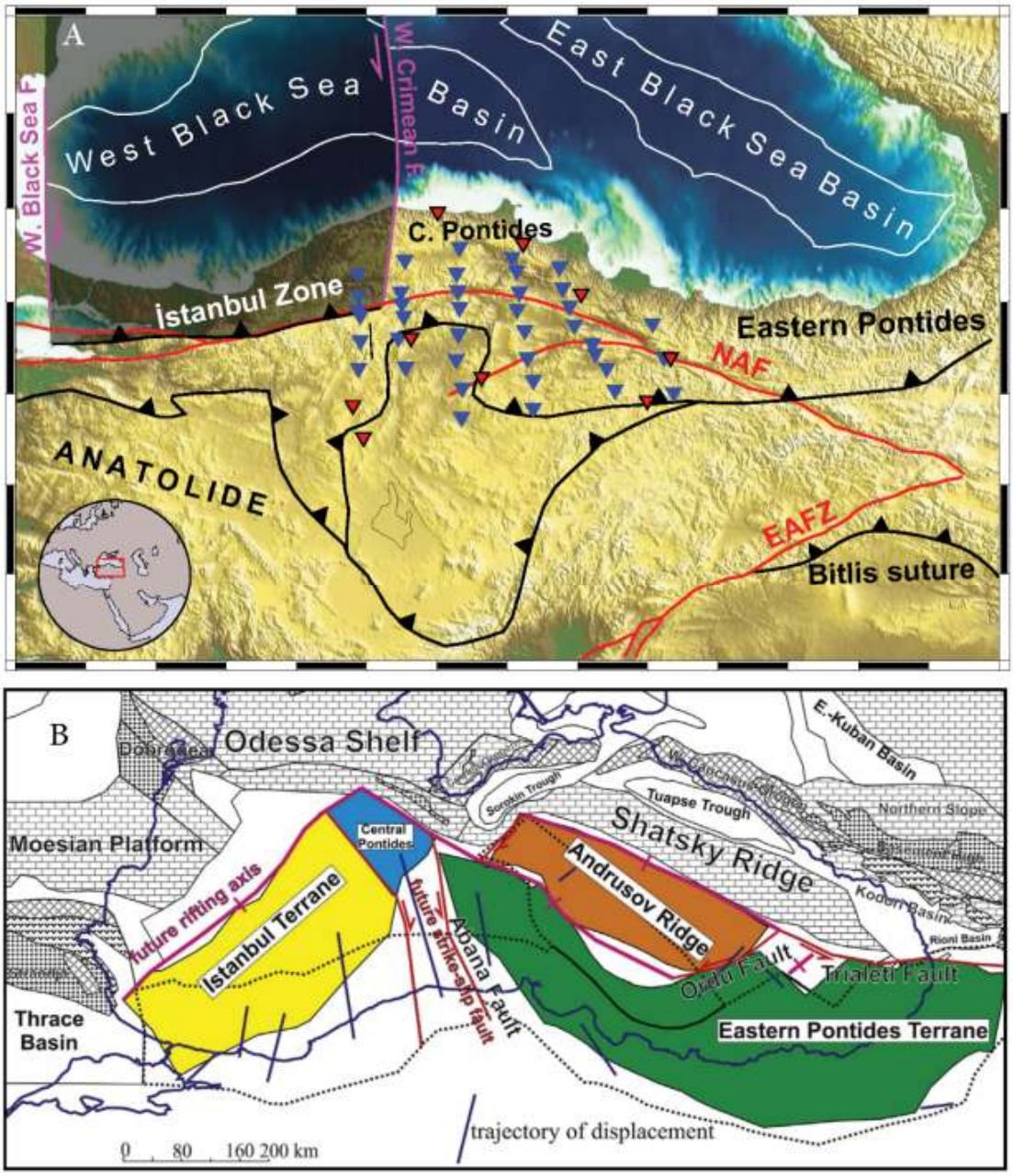

Figure 3-1: a) Terrane map showing major sutures and faults modified from Okay et al. (1994). Location of seismic stations are shown by inverted triangles b) Pre-Black Sea Basin opening tectonic structure restoration of Nikishin et al. (2015).

3-2- Data and Methods

Utilizing teleseismic P wave receiver function, demands the use of earthquakes with the focal distances between 30 and 95 degrees which are large enough to provide the required signal to noise ratios. In this study, total of 323 events with magnitudes larger than 5.5, recorded by the 39 broadband seismic stations deployed between 2005 and 2008 as part of the NAF experiment, are used to compute P receiver functions. Additionally, total of 9 KOERI station lying within the region are also included in the analysis to decrease the spatial distance between stations and increase the resolution (Figure 3-2).

The distribution of the used earthquakes are shown in figure 3-3a which demonstrates the dominance of the events sourcing from north and north east of the network, however, there are enough events sourcing from other directions to provide acceptable back-azimuthal coverage. The advantage of the receiver function analysis is its sensitivity to impedance contrast in an interface which makes this method suitable to image both negative and positive seismic discontinuities. This will be beneficial especially in regions with recent volcanic activity which are likely to have low velocity layers underneath the volcanos.

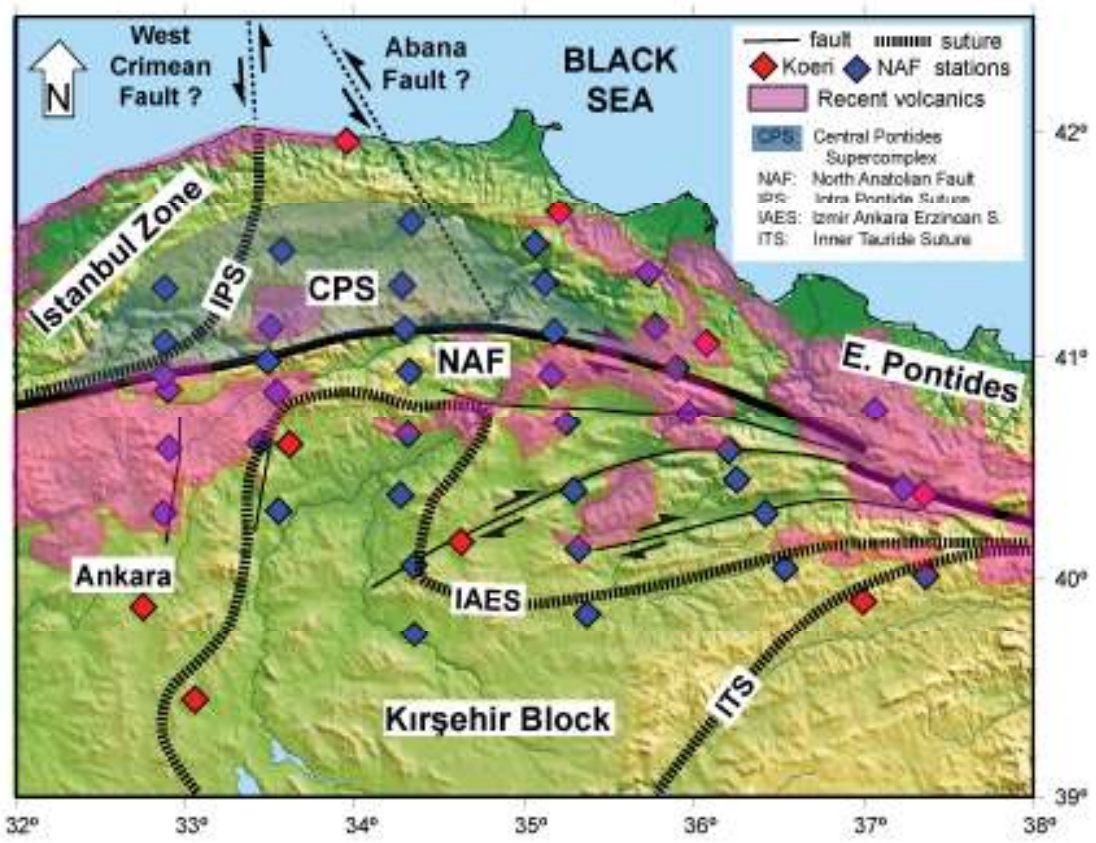

Figure 3-2: Tectonic map of the study area showing major faults, sutures, terranes and Neogene volcanism along with used broadband seismic stations (Modified after Okay and Tuysuz 1999).

Prior to any process on the data, the quality of the recorded data was visually inspected and traces without a clear P wave in all three components were omitted. After first step of quality control, data have been filtered between 0.05 and 3 Hz and consequently, the iterative time domain deconvolution (Iterdecon) method which is developed by Ligorria and Ammon (1999) is performed to obtain the teleseismic P receiver function for each record pair. Deconvolution process took place with the Gaussian filter width of 2.5 which corresponds to ~1 Hz center frequency (providing roughly 1 km vertical resolution). Subsequently, the second step of quality control were performed which includes the inspection of the resulted receiver function traces

and all unusual traces or traces with low variance reduction values (below 0.7, 0.8 or 0.9) were discarded.

3-2-1- Calculation of crustal thickness and Vp/Vs ratio

The calculated receiver function traces are in fact a series of time histories, therefore, a migration from time to depth domain is necessary. However, besides the depth of interface, there is another parameter (the Vp/Vs ratio) which has great impact on calculation of former. Hence, there is need for methods that resolve for both of these parameters simultaneously. Additionally, the known methods will not resolve for vertical variation of Vp/Vs ratio, therefore, the average Vp/Vs ratio of the entire column will be resolved.

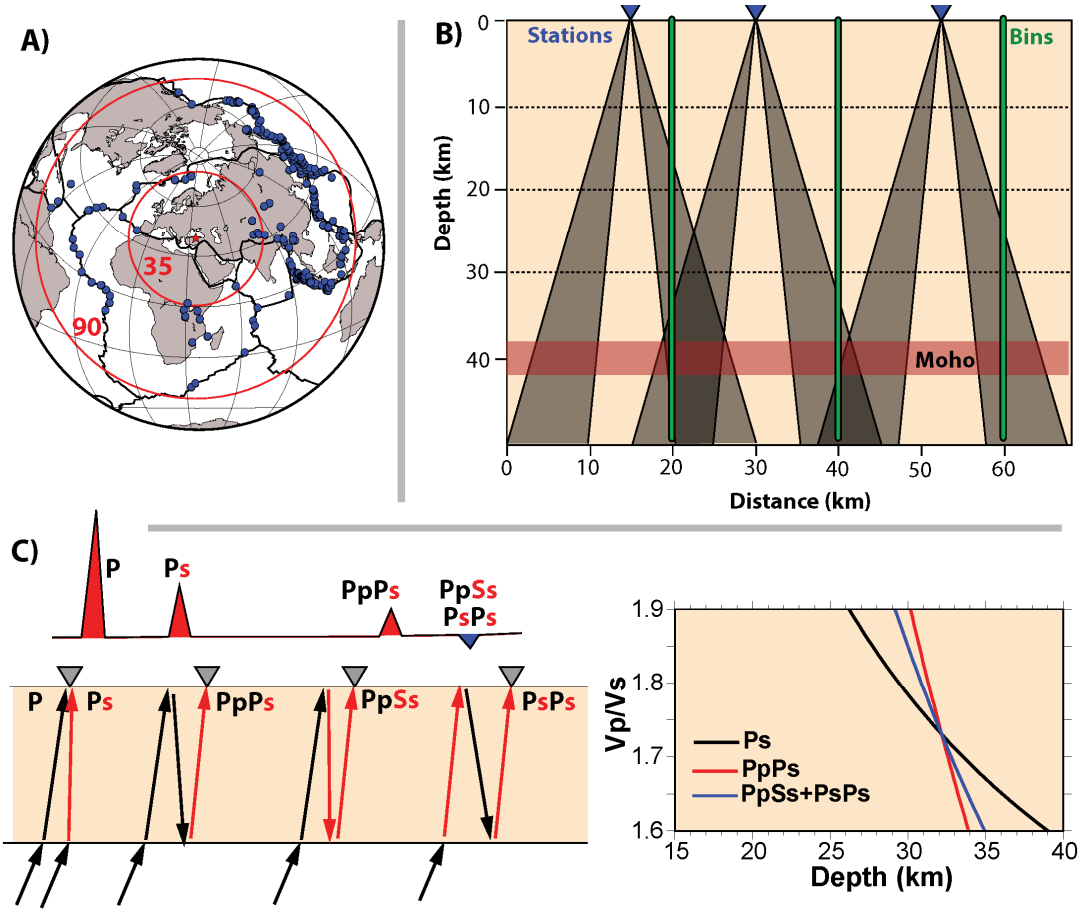

Figure 3-3: a) the azimuthal distribution of the earthquakes used in this study. Red asterisk represents the center of the network, the red circles show the 35 and 90 degree distances from the center of the network, b) subsurface sampling in the CCP stacking, c) used converted phases and maximum summed amplitude location in H-K stacking (Zhu and Kanamori, 2000).

3-2-1-1- The interactive phase picking CCP stacking method

The Common Conversion Point stacking method (Dueker and Sheehan, 1997) is based on the stacking all traces which are allocated in the same 3 dimensional grid cell (bin). To achive this, after quality control and moveout corrections, all receiver function traces tracked back to their path and stacked together for each bin. The output trace is considered as the representative of that 3 dimensional grid cell.

During this process, a constant Vp/Vs ratio is assumed which in this study Vp/Vs ratio of 1.75 is used to generate primary CCP stacking sections (figure 3-3b and c). These sections are generated for both Moho conversion phase (Ps) and its first multiple (PpPs). Then these sections are used for interactive picking of the Moho depth for both of the mentioned phases. Afterwards, the picked values from previous step is used to calculate real Vp/Vs ratios and MOHO depth of each bin. Finally the calculated Vp/Vs ratios will be utilized to generate new CCP stack sections using the variable Vp/Vs values. The bin size used in this study is 30*30 km (surface area) with the bin spacing of 20 km which leads to 10 km of overlap between two adjacent bins.

After picking the depths on both Ps and PpPs CCP plots (figure 3-3b), the crustal thicknesses of both phases will be used to recalculate the real Vp/Vs ratio for each bin as well as the MOHO depth (formulas *I* and *II*).

$$VpVs = \sqrt{\left(\frac{H_{Ps} \times \left(\sqrt{\left(\frac{VpVs_{cons}}{Vp}\right)^2 - P^2} - \sqrt{Vp^{-2} - P^2}\right)}{H_{PpPs} \times \sqrt{Vp^{-2} - P^2}} + 1\right)^2 \times (1 - P^2Vp^2) + P^2Vp^2} \quad (I)$$

$$H = \frac{t_{Ps}}{\sqrt{\left(\frac{VpVs}{Vp}\right)^2 - P^2} - \sqrt{V_p^{-2} - P^2}} \quad (II)$$

In which, H_{Ps} and H_{PpPs} are depths from Ps and *PpPs* phases respectively. P is ray parameter, $VpVs_{cons}$ is the constant Vp/Vs used to generate the initial cross sections.

Vp and *Vs* are compressional and shear wave Velocities respectively. *H* is corrected Moho depth and *Vp/Vs* is calculated true *Vp/Vs*.

It worth to mention that if the picked depths for both phases are close the calculated Vp/Vs ratio and depth will not change from those of the constant Vp/Vs plots. However in case of different depth picks for Ps and PpPs phases, significant changes in both parameters would be expected. However, in general the final depth will be very close if not the same to the depth picked on PpPs phase (this phase shows less sensitivity to Vp/Vs ratio changes and the depth shows slight variation, figure 3-3c)

3-2-1-2- The H-K stacking method

The H-K method is an automated migration procedure which uses the MOHO conversion (Ps) and its reverberations (PpPs and PpSs+PsPs phases) to calculate the demanded parameters (Zhu & Kanamori 2000). This method sums the amplitude of the MOHO conversion and its multiples for different values of Vp/Vs ratio. It is based on the fact that these three phases intersect at a point which corresponds to the real Vp/Vs ratio and MOHO depth and only at that point the summation will be constructive (figure 3-3c). Hence, theoretically, stacking these three phases with different Vp/Vs ratios and MOHO depths will have one maximum which is the demanded solution for that individual station. We have used unequal weighting in our calculations which are 0.6, 0.3 and 0.1 for Ps, PpPs and PsPs+PpSs phases respectively. These weights were suitable for most of the stations, however, needed to be adjusted in some stations with lower signal to noise ratio to find an acceptable solution.

The crustal thickness can be calculated using arrival time of each of the aforementioned phases. As expressed in formula *I,* the number of known parameters is one (the arrival time of that phase) whereas the number of unknowns is two which includes the MOHO depth and the shear wave velocity. However there is compressional wave velocity as well but we are assuming an average constant value for this parameter and it can be shown that the effect of changes in this parameter on the calculated MOHO depth is insignificant (Zhu and Kanamori, 2000)

3-3- Results

Our findings reveal that the crustal thickness changes sharply across the main strand of NAFZ indicating possible offsets in the Moho discontinuity. In the southern block, crust is relatively thin in the west (35 km) and becomes gradually thicker towards east (40 km) where multiple splays of NAF are present (Figure 3-4). In contrast, the northern block displays a sharp crustal thinning reaching up to 10 km across a narrow roughly N-S (NW-SE) oriented zone supporting the presence of a major terrain boundary (Figure 3-4).

In Vp/Vs ratio maps, there is no clear pattern at first glimpse especially in the map generated using H-K stacking method which is based on individual station analysis (Figure 3-4). On the other hand, in the Vp/Vs ratio map of CCP bin picking a more robust pattern is evident. On this map, in general it is apparent that eastern parts of the study area have relatively lower Vp/Vs ratios compared to western zones. Additionally, there are two clear high Vp/Vs ratio zones at the center of the region and in the west (Figure 3-4). The western anomaly correlates spatially well with the Galatian volcanic zone. The central anomaly shows a north-south alignment which has higher magnitudes in the south but the magnitude subsides after crossing the

NAFZ toward north (Figure 3-4). The north south alignment of the anomalies can also be interpreted as an artifact of the seismic network geometry which has less station spacing in north south direction.

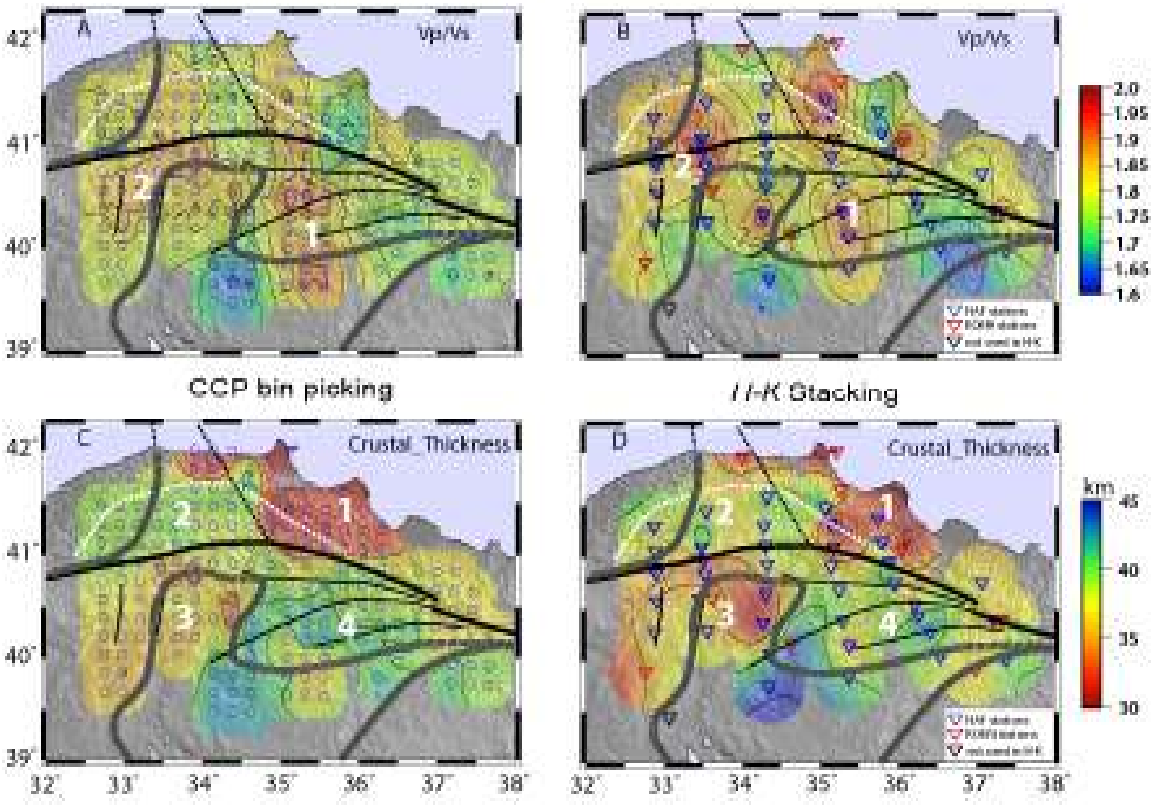

Figure 3-4: Moho depth and Vp/Vs maps calculated by CCP bin picking and H-K stacking. Circles and invert triangles represent the bins and stations respectively. Solid lines represent the faults, thick dashed lines represent the sutures. White numbers show the location of different anomalies.

At the east west trending depth migrated CCP profile, the MOHO depth seems to be invariant for first 200 km of the profile length. The crustal thickness is 35-40 km and shows slight change in 140th km but it is a minor variation. However, farther east in 200th km of the profile there is a considerable change in the crustal thickness which appears as a step with the thinner crust to the east (Figure 3-5a). This zone spatially correlates well with so called Abana fault (Nikishin et al. 2015) and northeastern boundary of CPS (Akdogan et al. 2017), thus interpreted as the terrane boundary between Central Pontides and Eastern Pontides. The Vp/Vs ratio of this profile has unusual pattern and shows higher values than average for almost entire profile with two large anomalies at the beginning of the profile and in the region which the step is observed.

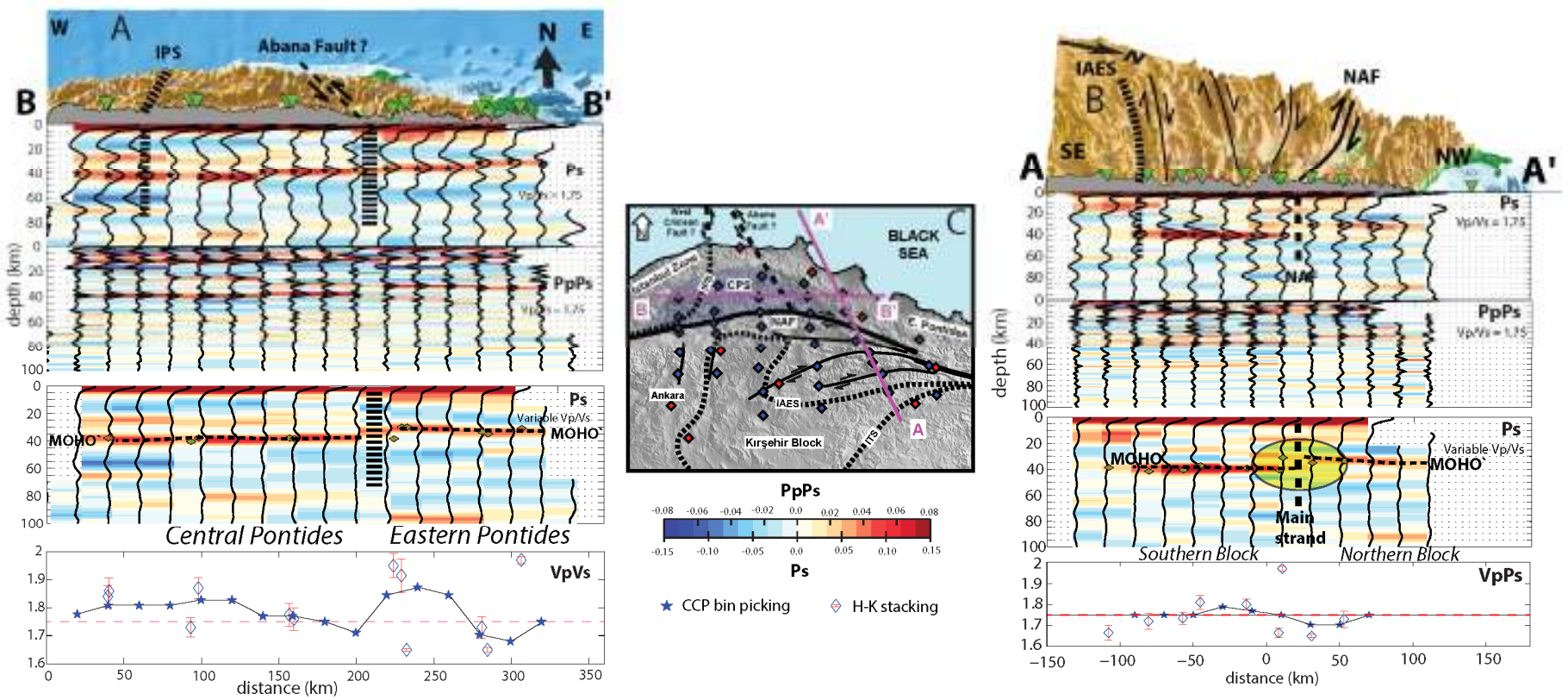

Figure 3-5: CCP cross sections of binned P teleseismic receiver functions plotted below 3D surface topography. Sections of Ps and PpPs phases are migrated to depth using constant Vp/Vs (1.75) and Moho discontinuity is picked (stars) at every bin for both phases which resulted in estimation of actual Vp/Vs across the profile. Depth migrated sections using variable Vp/Vs reflecting true positions of subsurface discontinuities and interpolated Vp/Vs values are shown at the bottom with related interpretations. For comparison, H-K stacking results for individual stations (blue diamonds) are also shown over the plots. Note that the profile locations are indicated at the location map given in the center

At the northwest southeast trending depth migrated CCP profile which cuts across the NAFZ (figure 3-5b), the crustal thickness is high in the first 140 km of the profile (in the southeast) and becomes thinner toward northwest. Also, there are dual MOHO traces at the part of profile which the transition from thick crust of the southeast to thinner crust of the northwest occurs. This transition does not exhibit a gradual variation and instead shows a sharp change in the form of a step in the MOHO. This transition also has very good correlation with surface trace of the NAFZ supporting a lithospheric scale faulting that offsets Moho discontinuity (figure 3-5b). The Vp/Vs ratio unlike the previous profile does not exhibit very large variations and for entire profile is close to the average value of 1.75. This profile has slightly higher ratio in the central part of the profile and slightly low values at the end.

3-4- Discussion

Both CCP bin picking and H-K stacking results are comparable (Figure 3-4). There are minor differences which can be sourced from the inherent characteristics of the methods which emphasis the lower spatial sampling of the H-K method compared to CCP bin picking. Therefore the results of the latter will be smoother and higher in resolution although the same data set are used for both methods. The bullseyes observed on the H-K stacking maps especially on the Vp/Vs ratio map is due to fact that this method is trying to simplify any tectonic geometry under the station to produce just one representative simple model for each station and its vicinity. This method is proper for simple structural settings for each station and whenever the station is close to any tectonic complexity (i.e. boundaries, suture zones of major structures), it will become unstable. The reason behind can be explained as the sampling various structural settings at different back-azimuths and trying to simplify with stacking these different traces together. Whereas, in the CCP bin picking

method while the traces for each cell (bin) is picked and analyzed independently, the effect of the complexity that will be minimized is related to the bin width and bin spacing. However, there will be a tradeoff between the bin size and degree of smoothing and manifestation of artefacts on the maps and cross-sections. Also the complex tectonic geometry will be reflected on the map more clearly up to some degree and resultant map will be smoother without having any sharp variation. Thus, CCP analysis is more ideal to uncover high frequency Moho topography.

The major findings of this research are the sharp or in some cases transitional changes of the crustal thickness along the region. In general, these changes are correlate well with the surface trace of the NAFZ and reflect the effect of this fault zone on the crustal structure (figure 3-4, Northward transition between anomalies 1 and 4, 2 and 3). This variation can be due to the juxtaposition of different material in either side by motion along the NAFZ or alternatively by the old suture zone. Şengör and Yılmaz (1981) shown that the development of the NAFZ in most of its length follows an old suture zone resulted from the closure of northern branch of Neotethys. This suture played a preexisting weak zone for development of the fault. On the other hand, due to the collision, two different continental materials will be juxtaposed which can make such anomalies. However the crustal thickness variation can be traced along entire length of the fault which supports the effect of the faulting in generation of such offsets. Accepting the fact that faulting is responsible for such anomalies, two competing geodynamic models which describe the subsurface geometry of strike-slip plate boundaries will rise. In the first model the transition from brittle to ductile deformation occurs within the crust meaning that the fault is in crustal scale. According to this model the induced stress from the upper crust will be accommodated in ductile form in lower crust and upper mantle, therefore, in this model the MOHO offset in not predicted. In the second model, lower crust and mantle lithosphere are rigid and strike-slip faults cut the entire crust as narrow shear zones. In other word, the fault is in lithospheric scale which will lead to creation of Moho offset. The second model best fits our findings however, the observed seismic

anisotropy (Biryol et al. 2010) contradicts the predictions of this model, which claims it should be parallel to the fault trend (Molnar et al, 1999). The reason might be due to local effect of this motion on mantle anisotropy and also insufficient resolution of the analysis. These crustal thickness changes can be followed across the main strand of the NAFZ which displays considerable variations (up to 10 km) from south to north. The variation perpendicular to the general extend of the NAFZ is predictable. However, crustal thickness changes also in east-west direction parallel to the NAFZ (figure 3-4, eastward variations of crustal thickness between anomalies 1 and 2, 3 and 4) and should be taken into account.

Izmir-Ankara-Erzincan suture zone (IAESZ) exhibits a very irregular shape (Figure 3-2) and shows a reverse U shape boundary just north of the Kırşehir massif. One of the aforementioned east west crustal thickness variations between anomaly 3 and 4 in figure 3-4 shows a relatively good spatial correlation with this suture zone in eastern boundary, however in the western part there is no noticeable crustal thickness changes. While this suture zone is a result of the closure of Neotethys ocean which to its north there are different terranes with different development histories (Okay and Tüysüz, 1999), it is possible to have lateral variations in the juxtaposed material and therefore in the seismic properties.

Another east-west variation in the crustal thickness can be traced south of the Sinop, north of the main NAFZ strand and in the central Pontides zone (between anomaly 1 and 2 in figure 3-4). The sharp crustal thinning towards east occurs within a few kilometers of width. This zone stands sub-perpendicular to the main extend of the NAFZ and does not spatially correlate with both IPS and IAES. There is significant dislocation of the MOHO (~10-15 km) which unveiled in both maps indicating the existence of a lithospheric scale structure offsetting MOHO in this location. In order to model the opening of the western Black Sea, Nikishin et al. (2015) suggested the existence of a wrench fault (namely Abana fault) at this place. Thus, we have

interpreted this zone as the subsurface signature of the Abana fault bounding Central Pontides from east.

The high Vp/Vs ratios are another phenomena which observed in two different regions. The first region (Figure 3-4) is the western part of the study area which well correlates with the Tertiary volcanism recorded in that region. However looking at the east west trending CCP profile (Figure 3-5) there is no evidences of low velocity layers at any depths in the crust. One reason can be the low thickness of the LVLs which is below our vertical resolution (the width of Gaussian pulse) so they did not appear in the results. Another alternative of having high Vp/Vs ratios without existence of fluids in the region (in this case the expected partial melts) is the presence of mafic or ultramafic rocks in the crust while these rocks can generate relatively higher Vp/Vs ratios compared to other rock types. Another possibility is the presence of seismic anisotropy which can be in the form of preferred cracks or lattice orientations (Wang et al. 2012). It is proven that the seismic anisotropy (especially in the subduction zones or their remnants) can increase the Vp/Vs ratio and in presence of the pore pressure the effect of the fluid will be amplified by the anisotropy which makes it possible to observe very high (> 2.2) Vp/Vs ratios. However, the observed high Vp/Vs ratios are not comparable to this value and are much lower which decrease the possibility of anisotropy effect in this region. Additionally, looking at the anisotropy map of the region, (Vinnik et al. 2016, Licciardi et al. 2018), there are no considerable seismic anisotropies at depths larger than 15 km but at shallower depths almost entire southern part (south of the main strand of the NAF) exhibits high anisotropy which shows good correlation with active structures or sutures in the region and can be related to active deformations taking place in this zone. Also there is no systematic variations of the anisotropy observed in the southern zone (Licciardi et al. 2018). The other high Vp/Vs anomaly is farther east (figure 3-4-A-1), which looking at the geological map of the region, the correlation of this anomaly with the Eocene volcanic rocks is evident. Additionally, Yolsal et al. 2012, modeled the velocity structure of the north Anatolia

for both P and S waves and developed the Vp/Vs maps of the region. In this study the maximum reliable resolution depth is 25 km so they have just modeled the velocity structure of upper crust. This anomaly displays a good spatial correlation with the relatively high depth to Vp=6.2 values. This correlation can be followed for the first anomaly as well.

Another finding can be revealed from comparison between crustal thickness and the elevation which can lead to address the isostatic equilibrium state of the region especially the high raised mountains. This comparison reveals that there is no correlation between these two which means the crust is not compensated or there is no isostatic equilibrium in the area. The high altitudes does not seem to have thick root which, while they are the results of the compression along the fault zone (see Vertical Anatolia Movement Project, part R2) , it can be concluded that the process which keeps them under (or over) compensated still continues. Another possible answer for this observation can be related to the age of the processes which are or were active in the region which if they are young there will not be enough time for the high altitudes to subside.

3-5- Conclusion

The data acquired by the temporary seismic experiment of NAF is used to generate the crustal and upper mantle seismic structure. Totally 327 teleseismic events with magnitudes larger than 5.5 are utilized in this study. To migrate from time to depth domain, two different methods used to increase the reliability of the results. The H-K stacking as well as newly developed CCP bin picking method which provides smoother results are employed to generate the crustal thickness maps as well as the Vp/Vs ratio variations. Additionally, The CCP stacking method also used to generate

a 3D bulk model of crustal thickness variations along the region which is used to generate the cross sections to reveal the lateral variations of the impedance for entire region. Our findings are itemized as below.

- The nature of discontinuities and crustal thickness display sharp changes across the main strand of NAFZ supporting a lithospheric scale faulting that offsets Moho discontinuity.
- In the southern block, crust is relatively thin in the west (35 km) and becomes gradually thicker towards east (40 km) where multiple splays of NAF are present.
- The northern block displays a sharp crustal thinning (from 40 km to 30 km) towards east across a narrow roughly N-S (NW-SE) oriented zone which is interpreted as the subsurface signature of the ambiguous terrane boundary between Central Pontides and Eastern Pontides.
- High Vp/Vs ratios are identified along the western and central parts of the study area which are partly coincide with the Tertiary volcanism.

CHAPTER 4

M-SPLIT: A GRAPHICAL USER INTERFACE TO ANALYZE MULTILAYERED ANISOTROPY FROM SHEAR WAVE SPLITTING[2]

Shear wave splitting analysis are commonly used to infer deep anisotropic structure. For simple cases, obtained delay times and fast-axis orientations are averaged from reliable results to define anisotropy beneath recording seismic stations. However, splitting parameters show systematic variations with back azimuth in the presence of complex anisotropy and cannot be represented by average time delay and fast axis orientation. Previous researchers had identified anisotropic complexities at different tectonic settings and applied various approaches to model them. Most commonly, such complexities are modeled by using multiple anisotropic layers with priori constraints from geologic data. In this study, a graphical user interface called M-Split is developed to easily process and model multilayered anisotropy with capabilities to properly address the inherited non-uniqueness. M-Split program runs user defined grid searches through the model parameter space for two-layer anisotropy using formulation of Silver and Savage (1994) and creates sensitivity contour plots to locate the local maxima and analyze all possible models with parameter tradeoffs. In order to minimize model ambiguity and identify the robust model parameters, various misfit calculation procedures are also developed and embedded to M-Split which can be used depending on the quality of the observations and their back-azimuthal coverage. M-Split is an open source program and can be extended by users for additional capabilities or for other applications.

[2] This chapter is published as the following paper: Abgarmi, B., Özacar A.A., 2017, M-Split: A Graphical User Interface to Analyze Multilayered Anisotropy from Shear-Wave Splitting, Seismological Research Letters, Volume 88, Number 4, doi: 10.1785/0220170020

4-1- Introduction

Shear wave splitting analysis of teleseismic data is widely used to image the anisotropy in the earth's interior. Splitting observations are used to infer crust and mantle fabric beneath recording stations related to past and current deformations. Normally shear wave splitting analyses are performed under the assumption of a simple model composed of just one horizontal layer with a horizontal axis of symmetry. But in some complex cases the splitting parameters show strong back azimuthal dependency. There are three different interpretations for variation of splitting parameters with respect to backazimuth. 1) two layered horizontal anisotropy (Savage and Silver 1993 , Silver and Savage 1994) or three or more anisotropic layers (e.g. Yang et al. 2014), can generate back azimuthal dependencies with 90 degrees of periodicity, 2) laterally varying anisotropy (Alsina and Snider 1995) and 3) inclined symmetry axis in the lithosphere (Babuska et al. 1984 , 1993- Silleny and Plomerova 1996- Plomerova et al. 1996).

Through time, numerous codes are developed to model splitting observations using simple one-layered anisotropy. Three techniques are commonly used to estimate the splitting parameters (i.e. fast polarization direction and delay time). These techniques are Minimum Energy "SC" (Silver and Chan, 1991), Rotation Correlation "RC" (Bowman and Ando, 1987) and Eigenvalue "EU" (Silver and Chan, 1991). Recently, Wüstefeld et al. (2007) developed Splitlab program to implement all three techniques along with a workflow set up to identify null measurement. An interactive forward modeling tool to have a preliminary insight about the two-layered anisotropy is also set in the Splitlab program. Unfortunately, this tool neither has proper grid search nor sensitivity analysis capabilities and thus is not commonly used. Until now forward codes are developed and used in individual cases and there was no comprehensive tool covering all those methods and also offering tools to analyze multi-layered anisotropy. We introduce our user friendly graphical program M-Split

that uses the same forward formulas introduced by Silver and Savage (1994) and enhanced misfit calculation algorithms for different observation conditions and limitations. Analysis of complex anisotropy suffers from presence of high level of non-uniqueness in the forward problem, hence, in this program a sensitivity analysis tool is also included to find all possible solutions in model space by plotting all local extremums.

4-2- Methodology

M-Split performs a grid search over the model parameter space that contains in this case fast polarization directions and delay times of two horizontal layers. It is also worth to mention that in grid search procedure; there is a tradeoff between the accuracy of the final output model and processing time. If a very fine grid search is carried out, the number of models that will be tested and therefore the time of the calculations will be highly increased but the final result will be more accurate. After performing the grid search, formulas introduced by Silver and Savage (1994) are used to calculate the theoretical splitting parameters for each set of model parameters. Finally, the theoretical / calculated splitting parameters are compared to the observations and model with the most resemblance to the observations is extracted. To compare the observations with calculated parameters, a misfit function calculated from residuals similar to Fontain et al. (2007)is utilized, and the model with the smallest residual is extracted as the best-fitting solution.

To test two horizontal-layered anisotropy assumption properly, same procedures including the grid search is also performed for one layered models. This enabled us to assess how much better a two-layered model fits the observations compared to the one-layered simple model and it is quantified by calculating the coefficient of

determination, R^2 (Walker et al. 2004) and the $R^2_{adjusted}$ (Walker et al. 2005a). In M-Split, various misfit calculation algorithms are developed and utilized which, depending on the quality and back azimuthal coverage of the observations, can be used for better results. The first algorithm is the *Unweighted* method that gives the same weight to all observations. In other words, all observations will have same effect in the misfit calculation and therefore same role in the final model extraction. If there is no measurement representing the observation quality or the calculated errors are not reliable, this method will be appropriate. As shown in formula (*I*), in misfit calculation, both *phi* and *dt* segments are normalized by the corresponding mean value of all observations.

$$misfit_{uw} = \sum_{i=1}^{n} \left[\frac{\left(\emptyset_{obs,i} - \emptyset_{calc,i}\right)^2}{(mean_{\emptyset})^2} + \frac{\left(\delta t_{obs,i} - \delta t_{calc,i}\right)^2}{(mean_{\delta t})^2} \right] \qquad (I)$$

In which, $\emptyset_{obs,i}$, $\emptyset_{calc,i}$, $\delta t_{obs,i}$ and $\delta t_{calc,i}$ are *i*'th observed and calculated fast polarization direction and observed and calculated delay times respectively and $mean_{\emptyset}$ and $mean_{\delta t}$ are mathematical mean values of fast polarization directions and delay times for all observations respectively.

Second algorithm is the *weighted* method that gives weights according to measurement errors so that observations with small errors will have greater effect in misfit calculation and therefore in the extracted final model. This method is proper for the observations that have solitary points with small errors that are in critical part of the model diagram and therefore, it is important that these points have more effect on the final calculated model (formula *II*). According to the formula, each part is normalized by its own error. The errors are the half of the difference of minimum and maximum values of that parameter (i.e. –errPhiXX and +errPhiXX and –

errdtXX and +errdtXX where XX stands for the method which used for splitting parameter estimation, SC, RC or EV) for that observation, in other words they are the average of differences between given value from its minimum and maximum (see *II*).

$$misfit_w = \sum_{i=1}^{n} \left[\frac{\left(\emptyset_{obs,i} - \emptyset_{calc,i}\right)^2}{\left(E_{\emptyset,i}\right)^2} + \frac{\left(\delta t_{obs,i} - \delta t_{calc,i}\right)^2}{\left(E_{\delta t,i}\right)^2} \right] \qquad (II)$$

$$E_{\emptyset,i} = \left(\emptyset_{max,i} - \emptyset_{min,i}\right)/2$$

$$E_{\delta t,i} = \left(\delta t_{max,i} - \delta t_{min,i}\right)/2$$

In which, $\emptyset_{obs,i}$,$\emptyset_{calc,i}$, $\delta t_{obs,i}$ and $\delta t_{calc,i}$are i'th observed and calculated fast polarization direction and observed and calculated delay times respectively. $E_{\emptyset,i}$and$E_{\delta t,i}$ are errors on fast polarization direction and delay time for i'th observation.

And finally the third method is Band-Fit method that is developed to reduce the effect of individual observations with small errors that dominate the final model. This method is proper for the input with the individual observations that have negative effect on the extracted model. As declared in formula (*III*), a difference function has been defined so that if the difference between observed and calculated values is smaller than the error range, then the difference function will be set to zero, otherwise, it will be the difference between the difference function and error function.

$$misfit_{bf} = \sum_{i=1}^{n} \left[\frac{\left(\emptyset_{dif,i}\right)^2}{(mean_{\emptyset})^2} + \frac{\left(\delta t_{dif,i}\right)^2}{(mean_{\delta t})^2} \right] \qquad (III)$$

$$\emptyset_{dif,i} = \begin{cases} 0 & if\left(\emptyset_{obs,i} - \emptyset_{calc,i}\right) \leq E_{\emptyset,i} \\ \left(\emptyset_{obs,i} - \emptyset_{calc,i}\right) - E_{\emptyset,i} & if\left(\emptyset_{obs,i} - \emptyset_{calc,i}\right) > E_{\emptyset,i} \end{cases}$$

$$\delta t_{dif,i} = \begin{cases} 0 & if\left(\left(\delta t_{obs,i} - \delta t_{calc,i}\right) \leq E_{\delta t,i} \right. \\ \left(\delta t_{obs,i} - \delta t_{calc,i}\right) - E_{\delta t,i} & if\left(\delta t_{obs,i} - \delta t_{calc,i}\right) > E_{\delta t,i} \end{cases}$$

In which, $\emptyset_{obs,i}$, $\emptyset_{calc,i}$, $\delta t_{obs,i}$ and $\delta t_{calc,i}$are *i'*th observed and calculated fast polarization direction and observed and calculated delay times respectively. $E_{\emptyset,i}$and$E_{\delta t,i}$ are errors on fast polarization direction and delay time for *i'*th observation. $mean_{\emptyset}$and$mean_{\delta t}$ are mean values of fast polarization direction and delay time for all observations respectively.

There are also two additional options to reduce the effects of possible back azimuthal errors. Normally, there is no back azimuthal correction but considering the possibility of back azimuthal error containing in observations, using tolerance on back azimuth can lead to better solutions. Also if number of observations in one back azimuthal range comparing to others are too high, then back azimuthal normalization can improve the final result.

In addition, the residual calculation algorithm proposed by Kaviyani et al. (2013) is also included in the program. Unlike others, this algorithm is based on calculation of the penalty function and provides an alternative approach for misfit assessment. It is worth to note that implementing such a variety in to M-Split give us the opportunity to compare results from various algorithms especially in the sensitivity analysis stage.

4-3- Program modules

The M-Split workflow is shown in Figure 4-1. It can be seen that this program composed of three major steps, data preparation, grid search and finally sensitivity analysis. In this program there are a few points that should be considered. First of all, the main assumption is that input data have 90 degrees of back azimuthal periodicity, hence, this program plots the data in mod 90 form. Therefore, all back azimuths are initially converted to mod 90. Secondly, applied grid search and misfit calculations for simple anisotropy with one-layered model are exactly the same as two layer models. Thus, quantitative comparison of best fitting model misfits for one and two-layer models aid user to decide about the number of anisotropic layers that should be used.

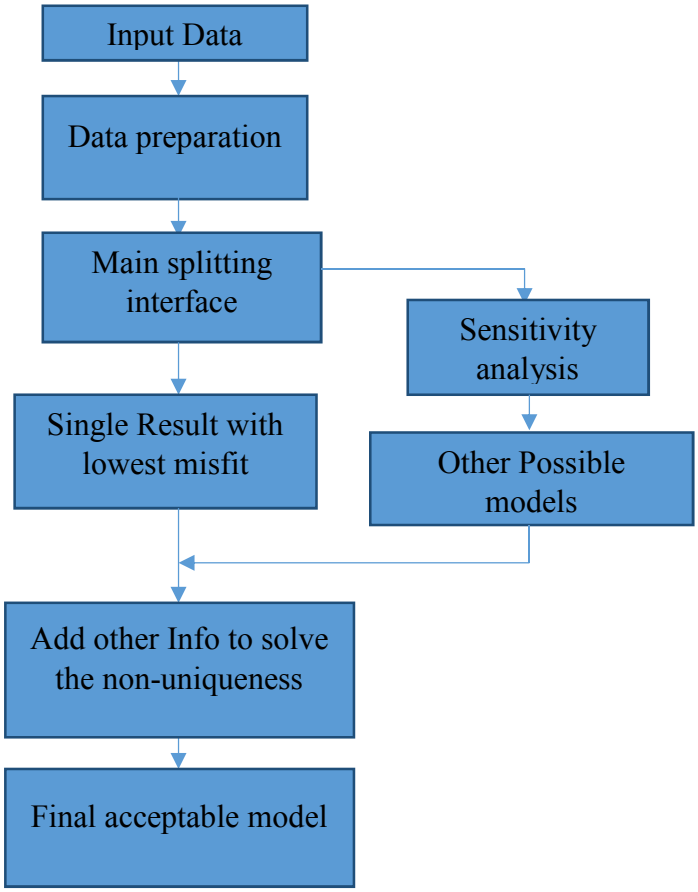

Figure 4-1: Workflow of the M-Split program

4-3-1- Data Conversion

As shown in Figure 4-2a, the start window of the program consists of two options, with and without data conversion. If data conversion is needed, then the conversion window will open (Figure 4-2b). Input of this program is compatible with the output of SPLITLAB program which is in tab delimited text format. M-Split generates two set of data formatted for different type of algorithms that user may use within the program. The program is adapted for three different shear wave splitting analysis

techniques which are minimum energy method (Silver and Chan, 1991), rotation correlation method (Bowman and Ando, 1987) and eigenvector method (Silver and Chan, 1991) and hence any of these methods can be used to generate the input files.

As mentioned before, the null observations can be detected using Splitlab program and can be included to the analysis in M-split without weighting since the large error ranges given for null observations will lead to minimal weights in weighted and band-fit approaches causing null data to have no effect on the final model. Therefore, the input of weighted and band-fit algorithms arranged so that they cannot contain the null observations. It is also important to note that, including null observations might lead to systematic error and deviate the final result from true model parameters. As an example, in the rotation correlation RC method, null observations are always 45 degrees off from the correct direction (Wüstefeld and Bokelmann 2006), thus including null data will lead to wrong solutions. On the other hand, if minimum energy SC (Silver and Chan, 1991) method is selected, null directions are expected to be parallel or perpendicular to fast polarization direction, so ones which are perpendicular will still contaminate the input data. In this respect, including null observations in the analyses is not recommended by the authors but not taken out entirely from the program for testing purposes. Therefore, including null data should be done with caution.

Figure 4-2: a) Program start window and b) Data conversion interface

4-3-2- Grid Search

Having data prepared in proper format, the next step is the comprehensive grid search to identify the best-fitting model. As shown in figure 4-3, the inversion window consists of 4 steps. First step is the data quality selection that user will decide about the quality of the observations that will be used in the misfit calculation and model extraction. It must be noticed that in most of the cases the number of the good quality data for a reliable estimation is not enough therefore using the fair quality observations will be necessary.

Next step is back azimuthal correction options that user can add a tolerance to the back azimuth so that program will calculate the misfit for the back azimuth range that can be defined as back azimuth plus minus the tolerance with the increments of step size. Finally, the minimum of the calculated misfits for the selected tolerance range will be considered as the misfit. It is necessary to mention that adding tolerance will drastically increase the process time, because, instead of a single point, misfit will be calculated for a vector. As another option in this part, back azimuthal normalization also can be selected. By using this option, the observations will be divided into 9 clusters of 10 degrees of back azimuthal range and each cluster will be normalized by the number of observation in that cluster. During adjustment of grid search parameters, the maximum and minimum values and their increments of the splitting parameters for both layers will be set. Like the tolerance, if increments set to a small value the processing time will increase because of increasing in the number of the models that should be tested.

The final step is the misfit calculation selection that user can choose one of the formerly mentioned methods to be used as the misfit calculation formula. The advantage of this program is that all models with corresponding calculated parameters (i.e. misfit, R2, etc.) will be written into a text file for future use. Also all models with positive R2 values will be written in another text file to use as an input

file for the sensitivity analysis program. The final model will be displayed on the results displaying screen (Figure 4-4). In some cases, two layered anisotropy parameters resulted from different algorithms can be very different but their resultant splitting may be very similar. Therefore, to visualize and compare the competing models, a model plotting console which plots splitting parameters of multiple models along with the observations, is established (Figure 4-5).

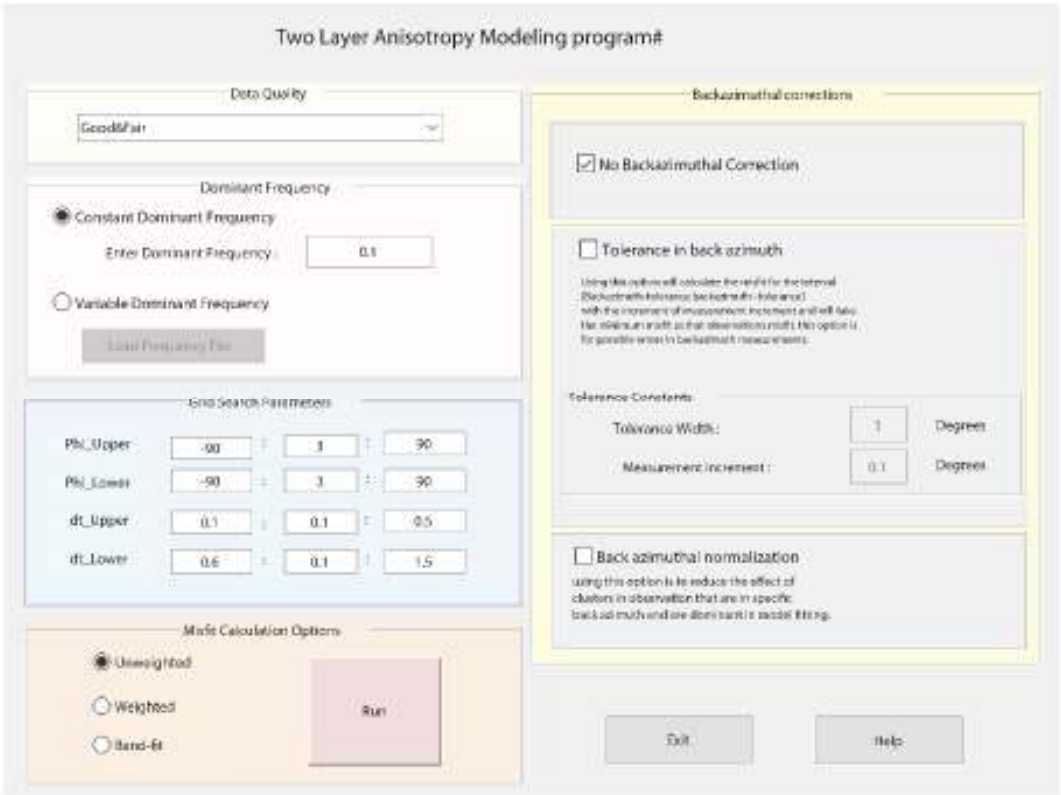

Figure 4-3: misfit calculation interface, this window includes the grid search and dominant frequency options and also provides choices for back-azimuthal corrections

Figure 4-4: Results interface that also provides options for sensitivity analysis and model comparison modules

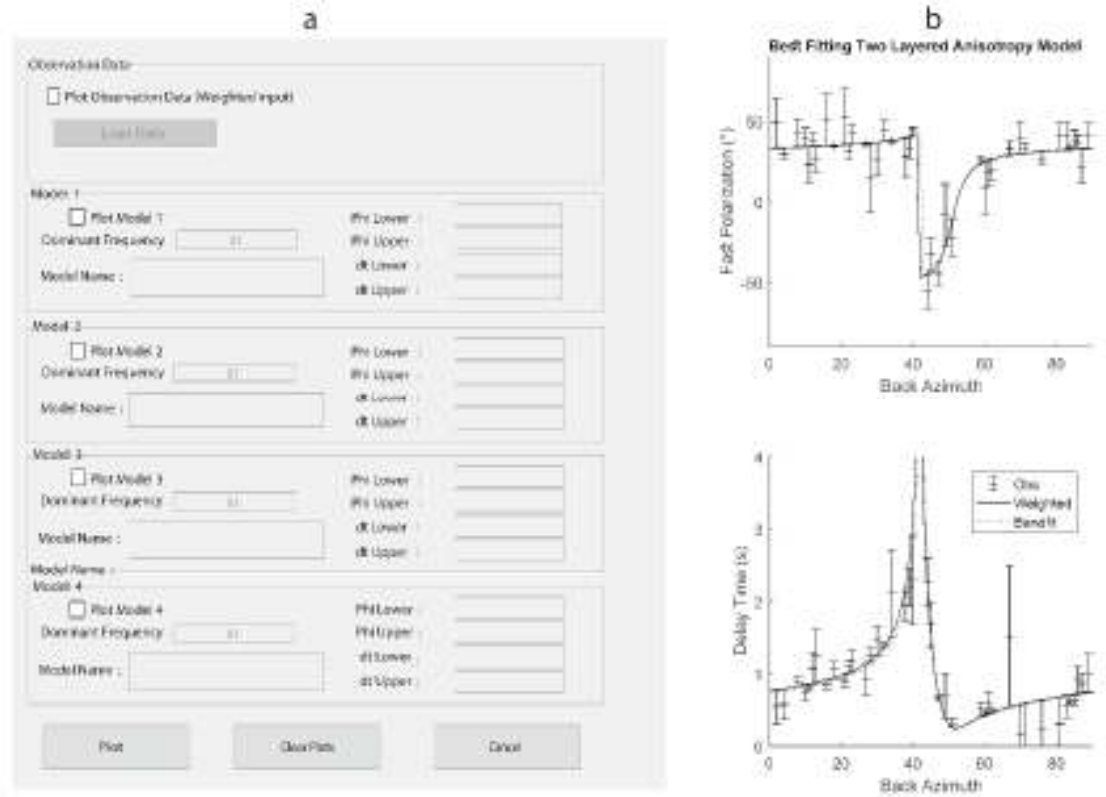

Figure 4-5: a) Interface to compare various models with different splitting parameters and also different dominant frequencies b) Resultant model plots of splitting parameters as a function of backazimuth along with observations.

4-3-3- Sensitivity analysis

Non-uniqueness of the resultant models is common in such grid search applications involving multiple variables. In many cases, the quantified misfits between set of models can be very close outlining the inherited non-uniqueness in identification of complex anisotropy and vitality of sensitivity analysis. To handle this issue a sensitivity analysis program has been developed (Figure 4-6). For this purpose, program uses all models with positive R2 values and generates contour plots to identify present local maxima (or minima) in the model parameters space for various misfit functions. The best fitting model parameters associated with each

local maximum are also plotted with their standard deviations. Eventually, if misfits calculated for multiple local maxima are similar, then the data can be represented equally well with multiple models and thus other independent data from geology, geodesy, tectonics etc. is needed to choose among these models.

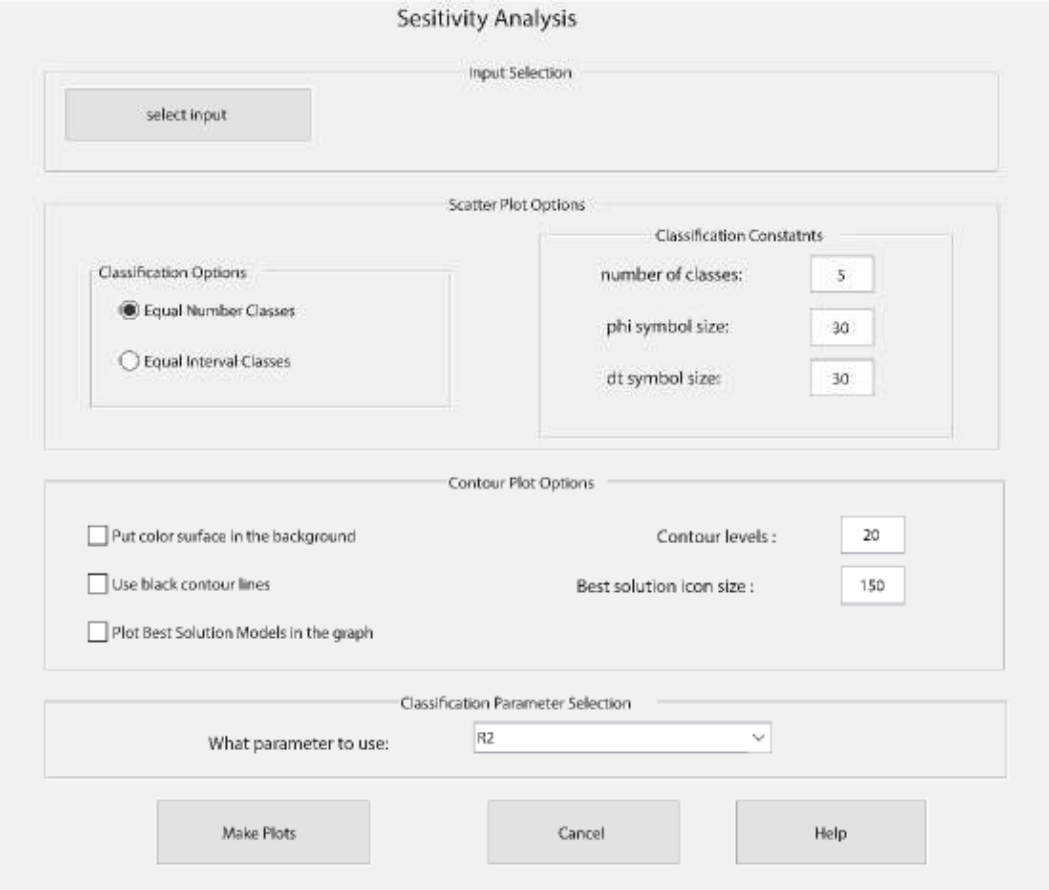

Figure 4-6: Sensitivity analysis interface which generates scatter and contour plots of best solutions in model space using the selecte parameter vaues

4-4- Synthetic test

To evaluate the program, formulas for apparent splitting parameters introduced by Silver and Savage (1994) are used to generate a discrete synthetic data correspond to defined model parameters. The dominant frequency of 0.1 Hz is used during the data generation phase and also in real and synthetic data tests. Consequently, forty points are randomly selected and used as synthetic observations to test the program. In first step, the synthetic data are used without noise and all three algorithms recovered the parameters correctly. In the second step, Gaussian white noise is included to the synthetic data. At this stage three signal to noise ratios are used (i.e. 5, 10 and 20). The error bonds for synthetic data are assigned by multiplying the differences between noiseless and noisy data with 0.5, 1 and 1.5 which produced 9 different synthetic datasets to test the program.

During synthetic tests using unweighted method with high noise rates or low signal to noise ratios (i.e. 5 and 10), the recovered model showed noticeable deviations from input model (Table 4-1; Figure 4-7). In contrast, both band-fit and weighted methods performed well even for noisy data (Table 4-1; Figure 4-5b) and in most of the cases, led to the correct model.

Table 4-1: Input and output model parameters extracted using different misfit calculation procedures and signal to noise ratios (SNR)

	Model Parameters			
	phi_lower	**phi_upper**	**dt_lower**	**dt_upper**
Input Model	50	-20	0.9	0.3
Unweighted SNR20	50	-20	0.9	0.3
Unweighted SNR10	54	18	0.6	0.3
Unweighted SNR5	50	-5	0.7	0.2
Weighted SNR20	50	-20	0.9	0.3
Weighted SNR10	50	-20	0.9	0.3
Weighted SNR5	50	-20	0.9	0.3
BandFit SNR20	50	-20	0.9	0.3
BandFit SNR10	55	-22	0.6	0.3
BandFit SNR5	50	-20	0.9	0.3

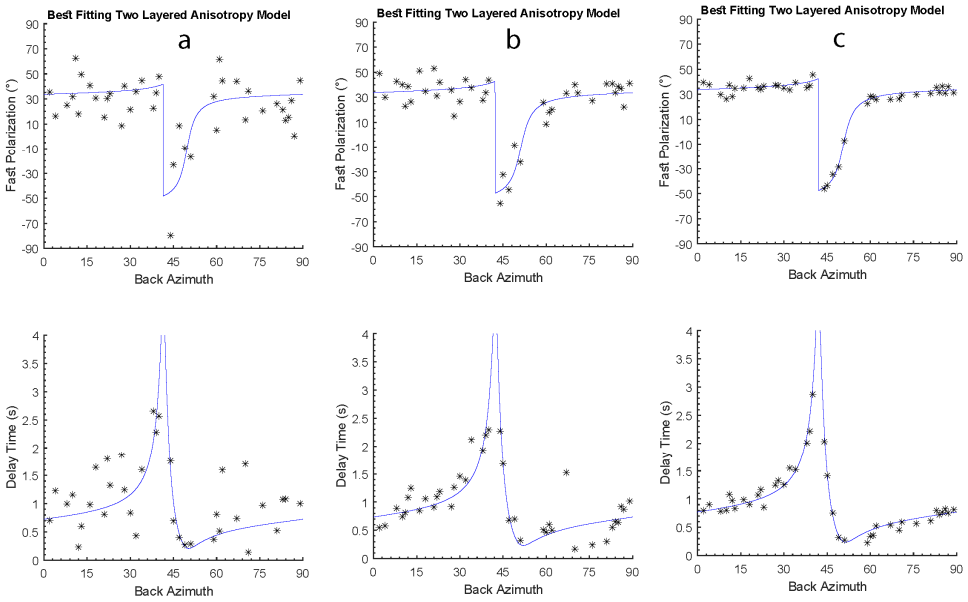

Figure 4-7: Unweighted synthetic test for noisy data with signal to noise ratios (SNR) of a) 5, b) 10 and c) 20

4-5- Analysis of Real Data

During the final step of the testing process, splitting measurements made for station BKS by Bonnin et.al (2010) are used. This data set is ideal for this purpose because it has a good back azimuthal coverage and had already been studied for complex anisotropy. Grid searches conducted using weighted and band-fit approaches led to results similar to Bonin et al. (2010). The used data displays highly variable error bonds which are ignored in the unweighted approach causing noticeable deviations from published model. In this respect, unweighting is not optimal for high quality data sets including well-defined error bonds.

In this data set, penalty function algorithm also selected a best-fitting model different than the minimum misfit, R2 and R2 adjusted which are intrinsically linked (Figure 4-8). During sensitivity analysis, contour plots of both given in Figure (4-9) reveal that for all parameters there are two model clusters characterized by equally low misfits. First cluster corresponds to model parameters given in the Bonnin et.al. (2010) and second cluster is the one picked by penalty function. The misfit distribution within model parameter space is nearly identical indicating that the data can be reproduced by both models. At this stage, non-uniqueness may be avoided only by incorporating data from independent sources such as assuming known plate motion to be parallel /sub-parallel to the upper layer fast axis direction.

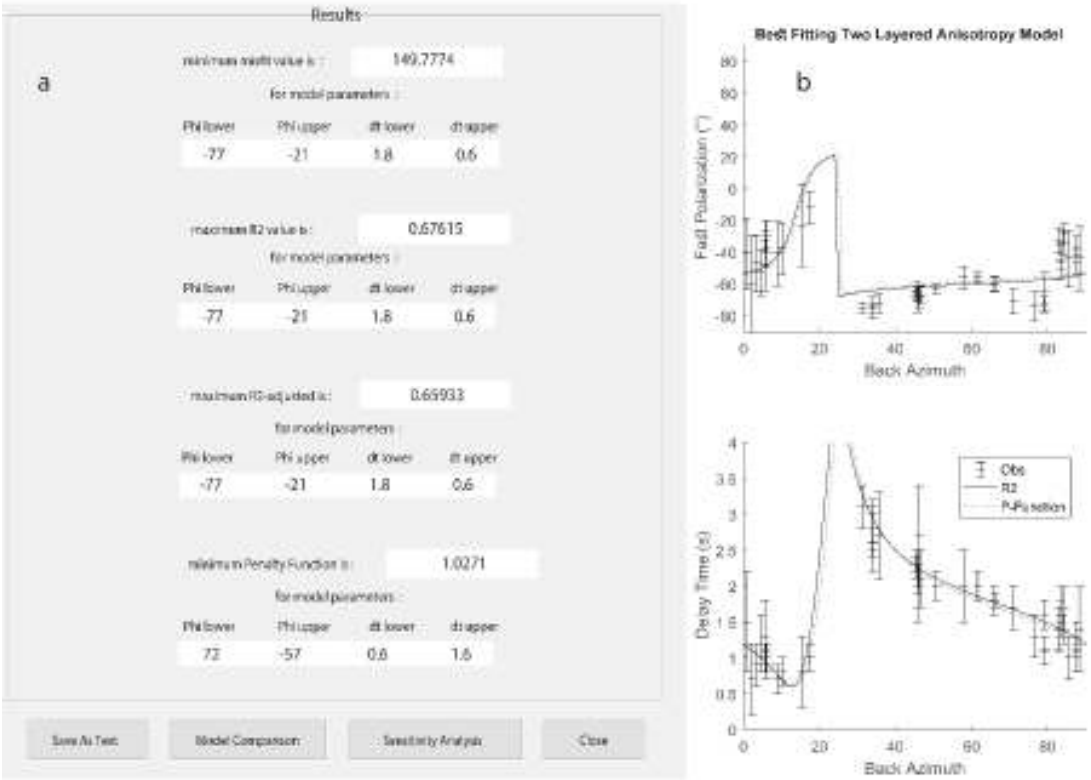

Figure 4-8: a) Multilayered anisotropy models obtained for station BKS using weighted approach b) Resultant model plots of splitting parameters as a function of backazimuth along with observations. Note that the best-fitting model identified by penalty function is remarkably different.

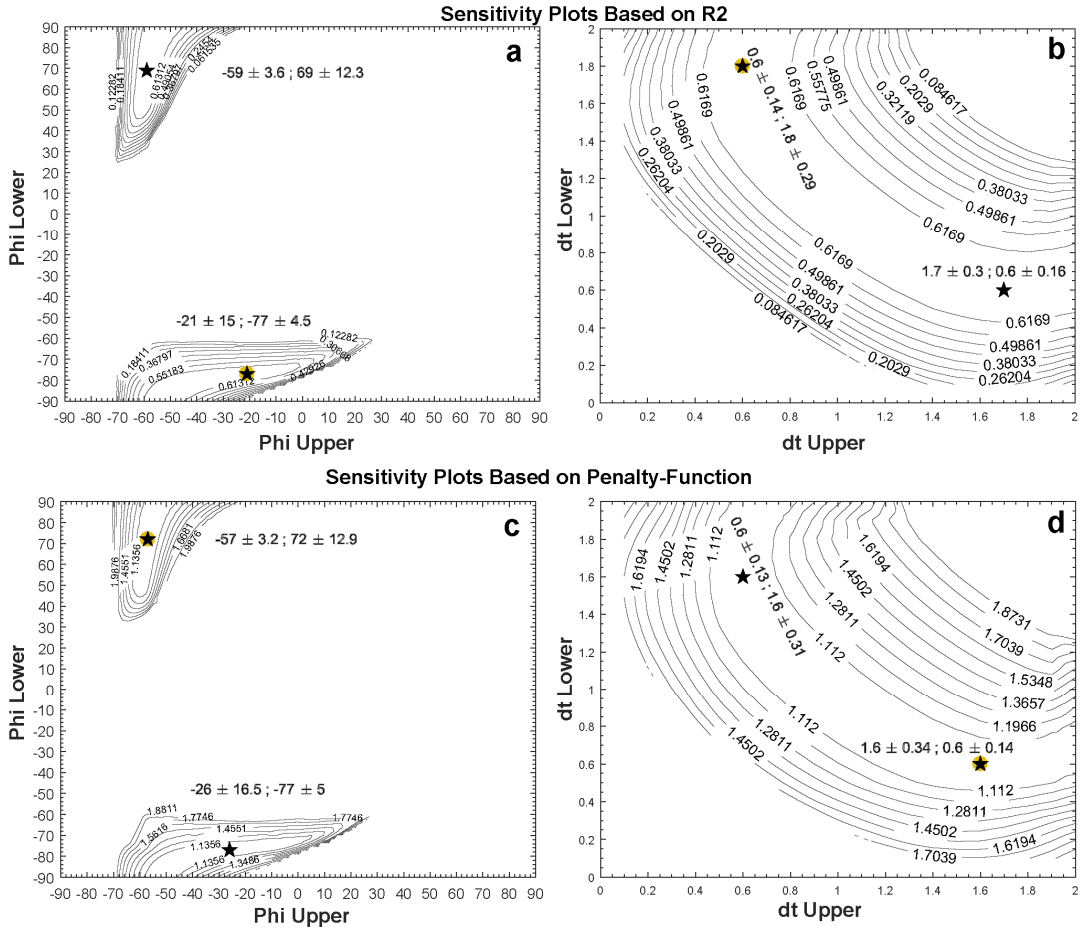

Figure 4-9: Contour plots of model space for both fast polarization directions (a and c) and delay times (b and d) based on two different calculated parameters using weighted approach for the splitting observations of station BKS. (a and b) are based on R^2 parameter and (c and d) are based on penalty function . Black stars show the local extremums and filled circle represents the best solution of used algorithm. The errors of parameters are shown on each extremum

4-6- Conclusion

We have presented a program that analyze shear wave splitting observations to find the best fitting multilayered anisotropy. M-Split can perform data preparation, model

fitting and sensitivity analysis for given data input. Program's interface provides a user friendly environment that automatically performs the calculations and produce visual outputs. In order to reduce the model ambiguity and test robustness, multiple misfit calculation procedures are embedded to the program and each has been subjected to rigorous testing. After successful tests conducted on both synthetic and real data, the reliability of the designed software is established. M-Split runs in MATLAB platform independent of operating system and successfully tested on Windows and Linux based computers.

4-7- Data and resources

All data used in this paper came from published sources listed in the references. The source codes of the program can be obtained from the following link:

www.m-split-code.com

Acknowledgement

We thank Mickael Bonnin for providing us the data that we used in our tests and validation process. We also are grateful to Eric Sandvol, Jonathan Robert Delph, Katrina Burch and Colton Lynn for their helpful comments.

CHAPTER 5

DISCUSSION

In this dissertation teleseismic P Wave receiver function has been benefited to help in better understanding the uncertainties in Anatolian plate. During this study, two different datasets from two different regions have been assessed to image the crustal structures and discontinuities. These data sets in general comprise the broadband seismic events which classify in the teleseismic category considering the epicentral distances. The data sets have been recorded by two temporary seismic network plus stations from the national seismic network of Turkey. The temporary networks comprise the CD-CAT experiment which deployed in central Anatolia with our collaboration and NAF experiment.

During our studies, to assess the receiver functions and use them in imaging the discontinuities, several different techniques are benefitted. These techniques are generally employed in calculating the crustal thickness and Vp/Vs ratio with different approaches. As a result, various computer programs in receiver function have been developed including SWA and bin picking methods. The general results obtained in this study are discussed separately in the following sections.

1. Depth extent of major strike slip faults:

Our findings in both CAT and NAF experiment reveals that the major faults including the NAF, EAF which are transform plate boundaries show considerable

amount of Moho offset. This indicates a lithospheric scale faulting across the boundaries of the Anatolian plate (Figure 5-1a). In addition, Central Anatolian Fault Zone (CAFZ) displays sharp changes at Moho discontinuity suggesting presence of a lithospheric scale structure. This may imply that due to extrusion of the Anatolian plate, some of the stress can possibly localized in this zone accommodating strain and hence, this fault zone might become boundary of the Anatolian plate in the future.

On other hand Tuz Gölü fault zone is another major structure which has been focused on in this study. In this fault zone we observe offset in subcrustal structures (low velocity layer at depths about 15-20 km) but no offset is deteched on the Moho discontinuity which may indicate that the fault is not cutting the entire crust (Figure 5-1b).

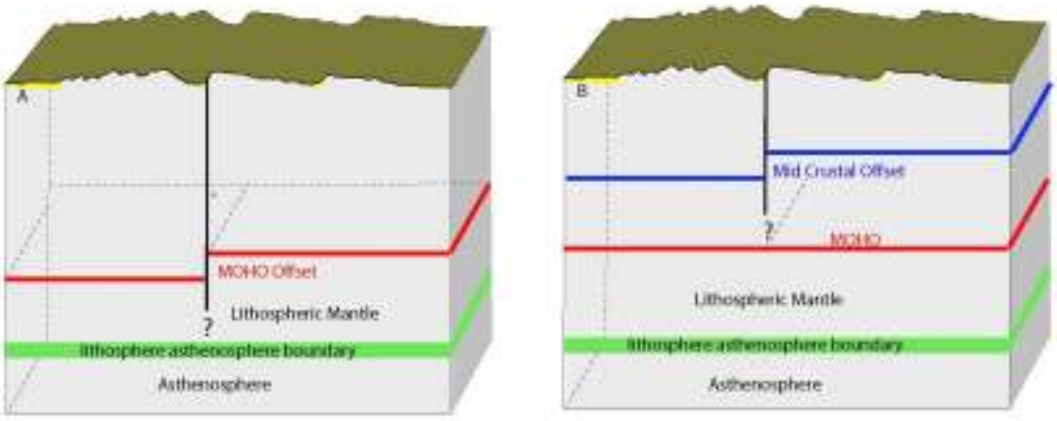

Figure 5-1: The general diagram of major strike slip fault zones along the study area. A) Lithospheric scale fault zones with offset in Moho and B) Crustal scale Fault zones with offset in mid crustal features.

2. Slab break off vs delamination:

Another phenomena which is discussed in this desertation is the rapid uplift in southern margin of the Anatolian plate. This phenomenon has been discovered recently in central Taurus Mountains as well as in Cyprus (Schilgen et al. 2014, Moreg et al. 2017). During our assessments of receiver function we observed an anomaly at depths around 80 km which is in a good agreement with previous studies (i.e. Bakirci et al. 2009). With benefitting from previous studies especially the body wave tomography images (Biryol et al. 2011, Portner et al. 2018), we interpreted this anomaly as the sub-horizontal African slab that is broken at depth. According to the geodynamic modelings (Piper et al. 2002, Duretz et al. 2012), the slab break off can generate considerable amount of surface uplift in short period of time and also the wave length of the uplift with respect to the depth of break off shows good correlation with surface observation. Hence our interpretation was in favor of relating some part of the surface uplift and other surficial effects to the slab break off. This phenomena, also can create asthonespher upwelling and explain the volcanic activities along the region.

On the other hand, there is another alternative model which is based on delamination and can create similar surficial effects. The conditions which are necessary to initiate delamination are existence of weak (aseismic) lower crust between strong mantle and upper crust and also negative buoyancy of the sinking slab (Göğüş et al. 2018). However the need for negative buoyancy might be fulfilled by the subducting oceanic lithosphere. In this model we will expect to see high heat transfer in Moho due to removal of the lithospheric mantle (or lower crust) and also thinning of the crust. However, in our results we observe very thick crust underneath the uplifted zone and also there is no evidences of high heat flow in this region. Thus we prefer the slab break off scenario.

3. Terrane boundaries present in the subsurface

The crustal thickness maps and constructed cross-sections in the entire region reveal the overall Moho topography. There are thick crusts which can be followed along the trend of the Taurus Mountains and also in southeastern zone of NAF main strand and also anomalously thin crust in the southeast and northeast of the study area and CAVP. In most of the cases the transition between these different crustal thicknesses occurs in places which show good spatial correlation with known structures and sutures. These boundaries can be followed along NAFZ, EAFZ, CAFZ and Bitlis-Zagros suture zone. However there are anomalous changes in the crustal thickness which apparently show no correlation with any known structures. One example of such an anomaly is the sharp change of the crustal thickness north of the main strand of NAF northern Turkey. This transition shows NNE-SSW trend and is almost perpendicular to the main strand of NAF. This boundary is interpreted as an unknown wrench fault which is named by Nikishin et al. (2015) as the Abana fault and basically is the boundary between Central and Eastern Pontides.

4. Complex tectonic settings and multi-layered anisotropy

In general, the two major transform faults bounding Anatolian plate (NAFZ and EAFZ) and CAFZ located within the plate cut through the crust and generate Moho offsets. The motion along these lithospheric scale faults can cause alignment of the minerals and therefore seismic anisotropy. On the other hand the possible slab break off in the southern margin of the region and possibly the northern margin as well can cause astenospheric upwelling along edges of the slab which would produce significant and spatially complex seismic anisotropy. Looking at the absolute and

relative plate motion directions reveals that the system is likely decoupled and crustal movements are significantly different from mantle flow. These two diferent directions as well add up to the complexity of the seismic anisotropy of this system. Therefore, analyzing of the seismic anisotropy as a single horizontal layer will be an over simplification of the system and may lead to unreal conclusions.

Hence there was a need for analyzing the complex anisotropy and the lack of a program which can assess multi-layered seismic anisotropy was evident. Thus, the M-Split program which is a comprehensive MATLAB based Graphical toolbox facilitating the analysis of complex seismic anisotropy, is developed. The program provides variety of tools which improves the model recovery and aids in solving the non-uniqueness problem of the solution. This program is tested with real data and also utilized successfully in a parallel study to image the complex seismic anisotropy along southern Turkey where it is believed that the slab break off and mantle flow at the edge of the slab will affect the seismic anisotropy (Pamir et al. 2014).

REFERRENCES

Abgarmi, B., Özacar A.A., 2017, M-Split: A Graphical User Interface to Analyze Multilayered Anisotropy from Shear-Wave Splitting, Seismological Research Letters Volume 88, Number 4, doi: 10.1785/0220170020

Abgarmi, B., Delph, J.R., Ozacar, A.A., Beck, S.L., Zandt, G., Sandvol, E., Turkelli, N., and Biryol, C.B., 2017, Structure of the crust and African slab beneath the central Anatolian plateau from receiver functions: New insights on isostatic compensation and slab dynamics: Geosphere, v. 13, no. 6, p. 1–14, doi:10.1130/GES01509.1.

Akdogan R., Okay A.I., Sunal, G., Tari, G., Meinhold, G., Kylander-Clark, A.R.C., 2017. Provenance of a large Lower Cretaceous turbidite submarine fan complex on the active Laurasian margin: Central Pontides, northern Turkey. Journal of Asian Earth Sciences, 134, 309-329.

Aksu A. E., Hall J. & Yaltirak C., 2005, Miocene to Recent tectonic evolution of the eastern Mediterranean: new pieces of the old Mediterranean puzzle. Mar. Geol., 221, 1–13.

Aksu A. E., Walsh-Kennedy S., Hall J., Hiscott R. N., Yaltırak C., Akhun S. D., *and* Çifçi G. 2014, The Pliocene–Quaternary tectonic evolution of the Cilicia and Adana basins, eastern Mediterranean: Special reference to the development of the Kozan fault zone, Tectonophysics, 622, 22–43.

ALSINA, D., and SNIEDER, R., Small-scale Sublithospheric Continental Mantle Deformation: Constraints from SKS Splitting Obser6ations, 1995. Geophysical Journal International 123(2):431 - 448 · DOI: 10.1111/j.1365-246X.1995.tb06864.x

Ammon, C.J., 1997. An overview of receiver function analysis. http://eqseis.geosc.psu.edu/~cammon/HTML/RftnDocs/rftn01.htm

Ambraseys, N.N., 2002. The seismic activity of the Marmara Sea region over the last 2000 years, Bull. seism. Soc. Am., 92, 1–18.Barka 1996

Ates A., Kearey P., Tufan S., 1999, New gravity and magnetic anomaly maps of Turkey, Geophys. J. Int. 136, 499–502.

Aydar E., Schmitt A. K., Çubukçu H. E., Akin L., Ersoy O., Sen E., Duncan R. A., Atici G., 2012, Correlation of ignimbrites in the central Anatolian volcanic province using zircon and plagioclase ages and zircon compositions, Journal of Volcanology and Geothermal Research 213-214, 83–97, doi:10.1016/j.jvolgeores.2011.11.005

Aydın F., Siebel W., Uysal I., Ersoy Y., Schmitt A., Sönmez M., Duncan R., 2012, Geochemical, isotopic (Sr–Nd–Pb) and geochronological (Ar–Ar and U–Pb) constraints on quaternary bimodal volcanism of the Niğde Volcanic Complex (Central Anatolia, Turkey). In: EGU conference, geophysical research abstracts, vol 14, pp 14300–14302.

Aydın F., Schmitt A.K., Siebel W., Sönmez M., Ersoy Y., Lermi A., Dirik K., Duncan R., 2014, Quaternary bimodal volcanism in the Niğde Volcanic Complex (Cappadocia, central Anatolia, Turkey): age, petrogenesis and geodynamic implications Contributions to Mineralogy and Petrology, 168, pp. 1–24.

Babuška, V., J. Plomerová, and J. Šílený ,1984, Large-scale oriented structures in the subcrustal lithosphere of central Europe, Ann. Geophys. 2, 649–662.

Babuška, V., J. Plomerová, and J. Šílený ,1993, Models of seismic anisotropy in the deep continental lithosphere, Phys. Earth Planet. In. 78, nos. 3/4, 167–191, doi: 10.1016/0031-9201(93)90154-2.

Bakırcı T., Yoshizawa K., and Ozer M. F., 2012, Three-dimensional S-wave structure of the upper mantle beneath Turkey from surface wave tomography, Geophys. J. Int. 190, 1058–1076.

Bartol J., Govers R., 2014. A single cause for uplift of the Central and Eastern Anatolian plateau. Tectonophysics 637 116–136.

Beck S. L., Zandt G., 2005, Continental lithospheric deformation along a major strike-slip fault zone: the central North Anatolian Fault Zone, Turkey. International Federation of Digital Seismograph Networks. Other/Seismic Network. doi:10.7914/SN/YL_2005.

Birsoy S., 2018, Earthquake focal mechanism analysis of central Anatolia, (Unpublished master's thesis), Middle Easte Technical University, Ankara, Turkey

Biryol, C.B., Zandt, G., Beck, S.L., Özacar, A., Adiyaman, H.E., Gans, C.R., 2010. Shear wave splitting along a nascent plate boundary: the North Anatolian Fault Zone. Geophys. J. Int. 1, 1201–1213. http://dx.doi.org/10.1111/j.1365-246X.2010. 04576.x.

Biryol C.B., Beck S. L., Zandt G., Ozacar A.A., 2011. Segmented African lithosphere beneath the Anatolian region inferred from teleseismic P-wave tomography. Geophys. J. Int. 184, 1037–1057.

Bonnin, M., Barruol, G., Bokelmann, G. H. R., Upper mantle deformation beneath the North American–Pacific plate boundary in California from SKS splitting, 2010, JOURNAL OF GEOPHYSICAL RESEARCH, VOL. 115, B04306, doi:10.1029/2009JB006438,

Bowman, J.R., Ando, M., Shear-wave splitting in the upper-mantle wedge above the Tonga subduction zone, 1987. Geophys J Int (1987) 88 (1): 25-41. DOI: 10.1111/j.1365-246X.1987.tb01367.x

Bozkurt E., 2001. Neotectonics of Turkey- a synthesis. Geodinamica Acta 14 , 3-30.

Brechner S., Klingel K., Krüger F., Plenefisch T., Backazimuthal Variations of Splitting Parameters of Teleseismic SKS Phases Observed at the Broadband Stations in Germany, 1998, Pure appl. geophys. (1998) 151: 305. DOI:10.1007/s000240050116

Buiter S.J.H., Govers R., Wortel M.J.R., 2002, Two-dimensional simulations of surface deformation caused by slab detachment, Tectonophysics 354, 195–210.

Bulut F., Bohnhoff M., Eken T., Janssen C., Kılıç T. and Dresen G., 2012, The East Anatolian Fault Zone: Seismotectonic setting and spatiotemporal characteristics of seismicity based on precise earthquake locations, Journal of Geophysical Research, VOL. 117, B07304, doi:10.1029/2011JB008966

Cemen I., Göncüoglu M. C., and Dirik K., 1999, Structural evolution of the Tuz Gölü basin in Central Anatolia, Turkey, J. Geol., 107, 693–706.

Christensen N.I., 1996, Elasticity of ultrabasic rocks, J. Geophys. Res., 71, 5921–5931.

Cosentino D., Schildgen F.T., Cipollari P., Faranda C., Gliozzi E., Hudáčková N., Lucifora S., Strecker M.R., 2012. Late Miocene surface uplift of the southern margin of the Central Anatolian Plateau, Central Taurides, Turkey. Geological Society of America Bulletin, DOI: 10.1130/B30466.1.

Crampin, S., 1981. A review of wave motion in anisotropic and cracked elastic-media. Wave Motion 3, 343–391.

Delph J.R., Porter R.C., 2015, Crustal structure beneath southern Africa: insight into how tectonic events affect the Mohorovicic discontinuity, Geophys. J. Int. 200, 254–264.

Delph, J.R., Biryol, C.B., Beck. S.L., Zandt, G., and Ward, K.M. (2015) Shear wave velocity structure of the Anatolian Plate: anomalously slow crust in SW Turkey. Geophysical Journal International 202, 261-276, doi: 10.1093/gji/ggv141.

Delph J.R., Zandt G., Beck S.L., 2015, A new approach to obtaining a 3D shear wave velocity model of the crust and upper mantle: An application to eastern Turkey, Tectonophysics, http://dx.doi.org/10.1016/j.tecto.2015.09.031.

Dueker K.G., Sheehan A.F., 1997, Mantle discontinuity structure from midpoint stacks of converted P to S waves across the Yellowstone hotspot track, Journal Of Geophysical Research, VOL. 102, NO. B4, Pages 8313-8327.

Duretz T., Gerya T.V., May D.A., 2011, Numerical modelling of spontaneous slab breakoff and subsequent topographic response, Tectonophysics 502 , 244–256.

Eagar K. C., Fouch M. J., 2012. FuncLab: A MATLAB Interactive Toolbox for Handling Receiver Function Datasets. Seismological Research Letters Volume 83, Number 3 doi: 10.1785/gssrl.83.3.596.

Eagar K. C., Fouch M. J., and James D. E., 2010. Receiver function imaging of upper mantle complexity beneath the Pacific Northwest, United States. Earth and Planetary Science Letters; doi:10.1016/j.epsl.2010.1006.1015.

Fayon A. K., Whitney D. L., 2006, Interpretation of tectonic versus magmatic processes for resetting apatite fission track ages in the Niğde Massif, Turkey, Tectonophysics 434 1–13, doi:10.1016/j.tecto.2007.01.003

Fichtner A., Saygin E., Taymaz T., Cupillard P., Capdeville Y., Trampert J., 2013, The deep structure of the North Anatolian Fault Zone, Earth and Planetary Science Letters 373 109–117, http://dx.doi.org/10.1016/j.epsl.2013.04.027

Fontaine, R. F., Barruol, G., Tommasi, A., Bokelmann, G. H. R., Upper-mantle flow beneath French Polynesia from shearwave splitting, 2007, Geophys J Int (2007) 170 (3): 1262-1288. DOI: 10.1111/j.1365-246X.2007.03475.x

Frassetto A.M., Zandt G., Gilbert H., Owens T.J. and Jones C.H., 2011, Structure of the Sierra Nevada from receiver functions and implications for lithospheric foundering, Geosphere; v. 7; no. 4; p. 898–921; doi: 10.1130/GES00570.1.

Gans C.R., Beck S.L., Zandt G., Biryol C.B. and Ozacar A.A., 2009, detecting the limit of slab break-off in central Turkey: new high-resolution Pn tomography results, Geophys. J. Int. 179, 1566–1572, doi: 10.1111/j.1365-246X.2009.04389.x

Govers R., Fichtner A., 2016, Signature of slab fragmentation beneath Anatolia from full-waveform tomography, 2016, Earth and Planetary Science Letters 450, 10–19, http://dx.doi.org/10.1016/j.epsl.2016.06.014

Göncüoğlu M. C., Toprak V., Kuscu I., Erler A., and Olgun E., 1991, Geology of the western part of the Central Anatolian Massif, part 1: Southern section [in Turkish], Turkish Petroleum Corporation (TPAO) Rep., 2909, 1–140.

Göğüş O.H., Ueda K., 2018, Peeling back the lithosphere: Controlling parameters, surface expressions and the future directions in delamination modeling,

Journal of geodynamics 117 (2018) 21-40
https://doi.org/10.1016/j.jog.2018.03.003

Gürer D., van Hinsbergen D. J. J., Matenco L., Corfu F. and Cascella A., 2016, Kinematics of a former oceanic plate of the Neotethys revealed by deformation in the Ulukışla basin (Turkey), Tectonics, 35, 2385–2416, doi:10.1002/2016TC004206.

Higgins M., Schoenbohm L. M., Brocard G., Kaymakci N., Gosse J. C., and Cosca M. A., 2015, New kinematic and geochronologic evidence for the Quaternary evolution of the Central Anatolian fault zone (CAFZ), Tectonics, 34, 2118– 2141, doi:10.1002/ 2015TC003864.

Innocenti F., Mazzuoli R., Pasquare G., Radicati Di Brozolo F., & Villari L., 1975, The Neogene calcalkaline volcanism of Central Anatolia: geochronological data on Kayseri-Nigde area, Geol. Mag. 112 (4), pp. 349-360.

Karasözen, E., Özacarö A.A., Biryol, C.B. and Beck S.L., 2014, Seismicity, focal mechanisms and active stress field around the central segment of the North Anatolian Fault in Turkey, Geophys. J. Int. (2014) 196, 405–42, doi: 10.1093/gji/ggt367

Kaviani, A., Hofstetter, R., Rümpker, G., Weber M., Investigation of seismic anisotropy beneath the Dead Sea fault using dense networks of broadband stations, 2013, JOURNAL OF GEOPHYSICAL RESEARCH: SOLID EARTH, VOL. 118, 3476–3491, doi:10.1002/jgrb.50250, 2013

Kaymakci N., Inceöz M., Ertepinar P., Koç A., 2010, Late Cretaceous to Recent kinematics of SE Anatolia (Turkey) Geol. Soc. Lond. Spec. Publ., 340, pp. 409-435.

Koçyığıt A., Beyhan A., 1998, A new intracontinental transcurrent structure: The Central Anatolian Fault Zone, Turkey, Tectonophysics 284, 317-336.

Le Pennec J. L., Bourdier J. L., Froger J. L., Temel A., Camus G., Gourgaud A., 1994, Neogene ignimbrites of the Nevsehir plateau (central Turkey): stratigraphy, distribution and source constraints, Journal of Volcanology and Geothermal Research 63 59-87, SSDI 0377-0273 (94) 00014-8

Le Pichon, X., Kreemer, C., Chamot-Rooke, N., 2005. Asymmetry in elastic properties and the evolution of large continental strike-slip faults. J. Geophys. Res. 110. http://dx.doi.org/10.1029/2004JB003343.

Lefebvre C., Meijers M. J. M., Kaymakci N., Peynircioğlu A., Langereis C. G., and van Hinsbergen D. J. J., 2013, Reconstructing the geometry of central Anatolia during the late Cretaceous: Large-scale Cenozoic rotations and deformation between the Pontides and Taurides, Earth Planet. Sci. Lett., 366, 83–98.

Licciardi A., Eken T., Taymaz T., Agostinetti N.P., Yolsal-Ç.S., 2018, Seismic anisotropy in central North Anatolian Fault Zone and its implications on crustal deformation, Physics of the Earth and Planetary Interiors 277 (2018) 99–112, https://doi.org/10.1016/j.pepi.2018.01.012

Ligorria J.P. & Ammon C.J., 1999, Iterative deconvolution and receiver function estimation, Bull. Seism. Soc. Am., 89(5), 1395–1400.

McClusky, S., et al., 2000. Global positioning system constraints on plate kinematics and dynamics in the eastern Mediterranean and Caucasus. J. Geophys. Res. 105, 5695–5719. http://dx.doi.org/10.1029/1999JB900351.

Molnar, P., H. J. Anderson, E. Audoine, D. Eberhart-Phillips, K. R.Gledhill, E. R. Klosko, T. V. McEvilly, D. Okaya, M. K. Savage, T. Stern, and F. T. Wu ,1999, Continuous deformation versus faulting through the continental lithosphere of New Zealand, Science, 286, 516–519.

Morag N., Haviv I., Katzir Y., 2016, From ocean depths to mountain tops: Uplift of the Troodos ophiolite (Cyprus) constrained by low-temperature thermochronology and geomorphic analysis, Tectonics Volume 35, Issue 3, pages 622–637

Muehlberger W.R. and Gordon M.B., 1987, Observations on the complexity of the East Anatolian Fault, Turkey, Journal of Structural Geology, Vol. 9, No. 7, pp. 899 to 903, 0191--8141/87

Mutlu A.K., and Karabulut H., 2011, Anisotropic Pn tomography of Turkey and adjacent regions, Geophys. J. Int., doi: 10.1111/j.1365-246X.2011.05235.x

Nikishin, A.M., Okay, A., Tüysüz, O., Demirer, A., Wannier, M., Amelin, N., Petrov, E., 2015. The Black Sea basins structure and history: New model based on new deep penetration regional seismic data. Part 2: tectonic history and paleogeography. Mar. Pet. Geol. 59, 656–670.

Okay A. I.,1984, Distribution and Characteristics of the North-west Turkish Blueschists, Geol. Soc. Spec. Publ., vol. 17, edited by A. I. Okay, pp. 455–466.

Okay, A.I., Şengör, A.M.C., Gorur, N., 1994. Kinematic history of the opening of the Black Sea and its effect on the surrounding regions. Geology 22 (3), 267-270.

Okay A.I. & Tuysuz O., 1999, Tethyan sutures of northern Turkey, In: DURAND. B., JOLIVET, L., HORVATH, E & SERANNE, M. (eds) The Mediterranean Basins: Tertiary Extension within the Alpine Orogen. Geological Society, London, Special Publications, J56o 475-515.

Özacar A. A., Zandt G., Gilbert H. & Beck S. L., 2010, Seismic images of crustal variations beneath the East Anatolian Plateau (Turkey) from teleseismic receiver functions, London, Special Publications, 340, 485–496. DOI: 10.1144/SP340.21 0305-8719/10/$15.00 The Geological Society of London

Özacar, A.A., Biryol, C.B., Zandt, G. and Beck, S.L., 2010. Deep Structure of Continental Strike-slip Faults Imaged by Receiver Functions, European Geophysical Union General Assembly 2010; 02–07 May 2010, Vienna, Austria.

Özacar, A.A., Abgarmi, B., Delph, J.R., Beck, S.L., Sandvol, E., Turkelli, N., Kalafat, D., Kahraman, M., & Teoman, U., 2015, “Central Anatolian Seismic Network: Initial Analysis of Seismicity and Earth Structure”. EGU General Assembly Conference Abstracts 17, 9024.

Özacar, A.A. and Abgarmi, B., 2017, Subsurface signature of North Anatolian Fault Zone and its relation with old sutures: New insight from receiver function

analysis, Geophysical Research Abstracts Vol. 19, EGU2017-14630, 2017 EGU General Assembly 2017

Özsayın E., Çiner A., Dirik K., Rojay B., Fernandez-Blanco D., Melnick D., Garcin Y., Bertotti G., Strecker M., Schildgen T., Sudo M., 2013, Plio-Quaternary extensional tectonics of the Central Anatolian Plateau: a case study from the Tuz Gölü Basin, Turkey. Attila Çiner, Manfred Strecker, Giovanni Bertotti (Eds.), T. Journal of Earth Sciences, 22, pp. 691-714, 10.3906/yer-1210-5.

Piper J.D.A., Gursoy H., Tatar O., 2002, Palaeomagnetism and magnetic properties of the Cappadocian ignimbrite succession, central Turkey and Neogene tectonics of the Anatolian collage, Journal of Volcanology and Geothermal Research 117, 237-262

Plomerová, J., J. Šílený, and V. Babuška (1996). Joint interpretation of upper mantle anisotropy based on teleseismic P-travel time delays and 3-D inversion of shear-wave splitting parameters, Phys. Earth Planet. In. 95, 293–309.

Portner, D.E., Delph, J.R., Biryol, C.B., Beck, S.L., Zandt, G., Ozacar, A.A., Sandvol, E., and Turkelli, N. (2018) Subduction termination through progressive slab deformation across Eastern Mediterranean subduction zones from updated P-wave tomography beneath Anatolia. Geosphere, 14(3), doi:10.1130/GES01617.1.

Radeff G., Schildgen T.F., Cosentino D., Strecker M.R., Cipollari P., Darbas G. and Gurbuz K., 2015, Sedimentary evidence for late Messinian uplift of the SE margin of the Central Anatolian Plateau: Adana Basin, southern Turkey, Basin Research 1–27, doi: 10.1111/bre.12159

Reid M. R., Schleiffarth W. K., Cosca M. A., Delph J. R., Blichert-Toft J. and Cooper K. M., 2017, Shallow melting of MORB-like mantle under hot continental lithosphere, Central Anatolia, Geochem. Geophys. Geosyst., 18, 1866–1888, doi:10.1002/ 2016GC006772.

Reilinger R., McClusky S., Vernant P., Lawrence S, Ergintav S., Cakmak R., Ozener H., Kadirov F., Guliev I., Stepanyan R., Nadariya M., Hahubia G., Mahmoud S., Sakr K., ArRajehi A., Paradissis D., Al-Aydrus A., Prilepin

M., Guseva T., Evren E., Dmitrotsa A., Filikov S.V., Gomez F., Al-Ghazzi R., and Karam G., 2006, GPS constraints on continental deformation in the Africa-Arabia- Eurasia continental collision zone and implications for the dynamics of plate interactions, Journal Of Geophysical Research, VOL. 111, B05411, doi:10.1029/2005JB004051

Ring U., Glodny J., Will T. and Thomson S., 2010, The Hellenic Subduction System: High-Pressure Metamorphism, Exhumation, Normal Faulting, and Large-Scale Extension, Annu. Rev. Earth Planet. Sci. 2010.38:45-76.

Rojay B., Heimann A., Toprak V., 2001, Neotectonic and volcanic characteristics of the Karasu fault zone (Anatolia, Turkey): The transition zone between the Dead Sea transform and the East Anatolian fault zone, Geodinamica Acta 14 197- 212, S0985311100010536/FLA

Salaun G., Pedersen H.A., Paul A., Farra V., Karabulut H., Hatzfeld D., Papazachos C., Childs D.M., Pequegnat C., and SIMBAAD Team, 2012, High-resolution surface wave tomography beneath the Aegean-Anatolia region: constraints on upper-mantle structure, Geophys. J. Int. 190, 406–420, doi: 10.1111/j.1365-246X.2012.05483.x

Sandvol E., Turkelli N., Barazangi M., 2003, The Eastern Turkey Seismic Experiment: The study of a young continent-continent collision, Geophysical Research Letters, Vol. 30, NO. 24, 8038, doi:10.1029/2003GL018912

Savage, M. K., and Silver, P. G., Mantle Deformation and Tectonics: Constraints from Seismic Anisotropy in the Western United States, 1993. Physics of the Earth and Planetary Interiors Volume 78, Issues 3–4, July 1993, Pages 207–227, doi: 10.1016/0031-9201(93)90156-4

Schildgen T.F., Yıldırım C., Cosentino D. and Strecker M.R., 2014, Linking slab break-off, Hellenic trench retreat, and uplift of the Central and Eastern Anatolian plateaus, Earth-Science Reviews 128, 147–168

Schildgen T. F., Cosentino D., Caruso A., Buchwaldt R., Yıldırım C., Bowring S. A., Rojay B., Echtler H., and Strecker M. R., 2012b, Surface expression of eastern Mediterranean slab dynamics: Neogene topographic and structural

evolution of the southwest margin of the Central Anatolian Plateau, Turkey, Tectonics, 31, TC2005, doi:10.1029/2011TC003021.

Schildgen, T.F., Cosentino D., Bookhagen B., Niedermann S., Yıldırım C., Echtler H., Wittmann H., Strecker M. R., 2012a, Multi-phased uplift of the southern margin of the Central Anatolian plateau, Turkey: A record of tectonic and upper mantle processes, Earth and Planetary Science Letters, Volumes 317–318, Pages 85–95, doi:10.1016/j.epsl.2011.12.003

Schleiffarth W.K., Reid M.R., and Cosca M.A., 2015, Ages, Distribution, and Evolution of Miocene Basalts, East-Central Anatolia: American Geophysical Union, Fall Meeting 2015, abstract #T22B-08Şengör A.M.C. & Yılmaz Y., 1981 Tethyan evolution of Turkey, a plate tectonic approach. Tectonophysics, 75, 181-241.

SILENY, J., and PLOMEROVA´, J., Inversion of Shear-wave Splitting Parameters to Retrieve Three-dimensional Orientation of Anisotropy in Continental Lithosphere, 1996, Physics of the Earth and Planetary Interiors Volume 95, Issues 3–4, June 1996, Pages 277-292, doi: 10.1016/0031-9201(95)03121-9

Silver, P. G., Savage, M. K., The interpretation of shear-wave splitting parameters in the presence of two anisotropic layers, 1994, geophysical journal international Volume 119, Issue 3, December 1994 Pages 949–963, DOI: 10.1111/j.1365-246X.1994.tb04027.x

Silver, P.G., Chan, W.W., Shear wave splitting and subcontinental mantle deformation. 1991, J. Geophys. Res., 96(B10), 16429–16454, doi:10.1029/91JB00899.

Soysal H., Sipahioglu S., Kolcak D. and Altinok Y., (1981) Turkye ve Cevresinin Tarihsel deprem Katalogu. TUBITAK, Proje no. TBAG 341, Istanbul

Stein R.S., Barka A.A. and Dieterich J.H.,1997, Progressive failure on the North Anatolian fault since 1939 by earthquake stress triggering, Geophys. J. Int. (1997) 128, 594-604

Şengör, A.M.C., Yilmaz, Y., 1981. Tethyan evolution of turkey: a plate tectonic approach. Tectonophysics 75, 181–241.

Şengör, A.M.C., 1984. The Cimmeride Orogenic System and the Tectonics of Euroasia. Geological Society of America Special Papers, 195.

Şengör A.M.C., Gorur N., Şaroğlu F., 1985, Strike Slip Faulting and Related Basin Formation In Zones Of Tectonic Escape Turkey As a Case Study, The Society of Economic Paleontologists and Mineralogists

Şengör, A.M.C., 1987. Tectonics of the Tethysides: Orogenic collage development in a collisional setting. Annual Reviews of Earth and Planetary Science, 15, 213-244.

Şengör, A.M.C., 1990. A new model for the late Paleozoic-Mesozoic tectonic evolution of Iran and implications for Oman. In: ROBERTSON, A. H. E, SEARLE, M. R & RIES, A. C. (eds) The Geology and Tectonics of the Oman Region. Geological Society, London, Special Publications, 49, 797-831.Şengör & Natal'in 1996

Şengör A.M.C., Tüysüz O., İmren C., Sakınç M., Eyidoğan H., Görür N., Le Pichon X. and Rangin C., 2005, The North Anatolian Fault: A New Look, Annu. Rev. Earth Planet. Sci. 2005. 33:37–112, doi: 10.1146/annurev.earth.32.101802.120415

Şengör A.M.C., Özeren M.S., Keskin M., Sakınç M., Özbakır A.D., Kayan İ., 2008, Eastern Turkish high plateau as a small Turkic-type orogen: Implications for post-collisional crust-forming processes in Turkic-type orogens, Earth-Science Reviews 90, doi:10.1016/j.earscirev.2008.05.002

Toprak V., 1998, Vent distribution and its relation to regional tectonics, Cappadocian Volcanics, Turkey, Journal of Volcanology and Geothermal Research 85 1998. 55–67

Toprak V., Göncüoğlu M.C., 1993. Tectonic control on the development of the Neogene-Quaternary Central Anatolian volcanic province Turkey. Geological J. 28, 357–369.

Turkelli N., Kahraman M., Teoman M.U., Polat G., Polat R., Kalafat D., Ozer M., and Cok O., 2015, Initial Results from the Central Anatolian Seismic Experiment: Local Seismicity and Shear Wave Splitting, 8th Congress of the Balkan Geophysical Society, DOI: 10.3997/2214-4609.201414238.

van Hinsbergen D. J. J., Maffione M., Plunder A., Kaymakcı N., Ganerod M., Hendriks B. W. H., Corfu F., Gürer D., de Gelder G. I. N. O., Peters K., 2016, Tectonic evolution and paleogeography of the Kırşehir Block and the Central Anatolian Ophiolites, Turkey, Tectonics, 35, 983–1014, doi:10.1002/2015TC004018.

Vanacore E.A., Taymaz T. and Saygin E., 2013. MOHO structure of the Anatolian Plate from receiver function analysis. Geophys. J. Int. 193, 329–337.

Vinnik, L., Oreshin, S., Erduran, M., 2016. Melt in the mantle and seismic azimuthal anisotropy: evidence from Anatolia. Geoph. J. Int. 205, 523–530. http://dx.doi.org/10.1093/gji/ggw021.

Walker, K.T., Nyblade, A.A., Klemperer, S.L., Bokelmann, G.H.R. & Owens, T.J., 2004. On the relationship between extension and anisotropy: constraints from shear wave splitting across the East African Plateau, J. Geophys. Res., 109, doi:10.1029/2003JB002866.

Walker, K.T., Bokelmann, G.H.R., Klemperer, S.L. & Bock, G., 2005a. Shear-wave splitting around the Eifel hotspot: evidence for a mantle upwelling, Geophys. J. Int., 163, doi: 10.1111/j.1365–246X.2005.02636.x.

Wang X.-Q., Schubnel A., Fortin J., David E.C., Guéguen Y. and Ge H.-K., 2012, High Vp/Vs ratio: Saturated cracks or anisotropy effects?, Geophysical Research Letters, VOL. 39, L11307, doi:10.1029/2012GL051742.

Warren M. L., Beck S.L., Biryol C.B., Zandt G., Ozacar A.A., And Yang Y., 2013, Crustal velocity structure of Central and Eastern Turkey from ambient noise tomography, Geophys. J. Int. 194:1941-1954.

Wessel, P. and Smith, W.H.F., 1991, Free Software Helps Map and Display Data, Eos, Vol. 72, No. 41.

Whitney D. L. & Davis P.B., 2006, Why is lawsonite eclogite so rare? Metamorphism and preservation of lawsonite eclogite, Sivrihisar, Turkey, Geological Society of America; v. 34; no. 6; p. 473–476; doi: 10.1130/G22259.1; 3

Whitney D.L. and Hamilton M., 2004, Timing of high-grade metamorphism in central Turkey and the assembly of Anatolia. Journal of the Geological Society of London, 161 (5), 823-828.

Whitney, D.L., Teyssier, C., Fayon, A.K., Hamilton, M.A., and Heizler, M. (2003) Tectonic controls on metamorphism, partial melting, and intrusion: timing of regional metamorphism and magmatism of the Niğde Massif, Turkey. Tectonophysics, 376, 37-60.

Whitney D.L., and Dilek Y., 1997, Core complex development in central Anatolia. Geology, 25, 1023-1026.

Wüstefeld, A., Bokelmann, G., Zaroli, C., Barruol, G., SplitLab: A shear-wave splitting environment in Matlab, 2007, Computers & Geosciences 34(5):515-528 · May 2008 DOI: 10.1016/j.cageo.2007.08.002

Wüstefeld, A., Bokelmann, G., Null Detection in Shear-Wave Splitting Measurements, 2006, Bulletin of the Seismological Society of America August 2007 vol. 97 no. 4 1204-1211 doi: 10.1785/0120060190

Yang, B.B., Gao, S.S., Liu, K.H., Elsheikh, A.A., Lemnifi, A.A., Refayee, H.A. and Yu, Y., Seismic anisotropy and mantle flow beneath the northern Great Plains of North America, J. Geophys. Res. Solid Earth, 119, 1971–1985, doi:10.1002/2013JB010561.

Yılmaz Y., Tüysüz O., Yiğitbaş E., Genç C.Ş., Şengör A.M.C., 1997, Geology and tectonic evolution of the Pontides, in A.G.Robinson, ed., Regional and Petroleum geology of the Black sea and surrounding region: AAPG Memoir 68 p. 183-226.

Yolsal-Ç.S, Biryol C.B., Beck S., Zandt G., Taymaz T., Adıyaman H.E., and Özacar A. A., 2012, 3-D crustal structure along the North Anatolian Fault Zone in

north-central Anatolia revealed by local earthquake tomography, Geophys. J. Int. (2012) 188, 819–849, doi: 10.1111/j.1365-246X.2011.05313.x

Zandt G., Ammon C. J., 1995, Continental crust composition constrained by measurements of crustal Poisson's ratio, Nature, VOL 374

Zhu L., Kanamori H., 2000, Moho depth variation in southern California from teleseismic receiver functions, journal of geophysical research, VOL. 105, NO. B2, pages 2969-2980

CURRICULUM VITAE

PERSONAL INFORMATION

Surname, Name: Bizhan Abgarmi
Nationality: Iranian
Date and Place of Birth: 8 August 1980, Iran
Marital Status: Single
Phone: +90 538 732 57 20
email: bizhan.abgarmi@metu.edu.tr

EDUCATION

Degree	Institution	Year of Graduation
MS	Tehran University, Mining Engineering, Mine exploration	2006
BS	Tehran University, Mining Engineering, Mine exploration	2003
High School	Iran	1998

WORK EXPERIENCE

Year	Place	Enrollment
2018-Present	ENVY Energy and Environmental Investments Inc.	Geological/geophysical Eng.
2017-2018	Tubitak	Project Assistant
2012-2014	Tubitak	Project Assistant
2013-2015	NSF	Project Assistant
2008-2010	Payamenoor University of Naghadeh, Iran	Lecturer

FOREIGN LANGUAGES

Advanced English, Fluent Persian, Turkish, Azerbaijani (Mother Thoung)

PUBLICATIONS

1. Abgarmi, B., Delph, J.R., Ozacar, A.A., Beck, S.L., Zandt, G., Sandvol, E., & Turkelli, N., Biryol, C.B., "Structure of the crust and African slab beneath the Central Anatolian Plateau from receiver functions: new insights on isostatic compensation and slab dynamics", Geosphere. V. 13 no. 6 doi: 10.1130/GES1509.1.

2. Abgarmi, B., Ozacar, A.A., "M-Split: A Graphical User Interface to Analyze Multilayered Anisotropy from Shear Wave Splitting", Seismological Research Letters Volume 88, Number 4 July/August 2017, doi: 10.1785/0220170020

3. Delph, J., R., Abgarmi, B., Ward, K. M., Beck, S. L., Ozacar, A. A., Zandt, G.,Sandvol E., Turkelli, N. and Kalafat D.,The effects of subduction termination on the continental lithosphere: Linking volcanism, deformation, surface uplift, and slab tearing in central Anatolia, Geosphere, v. 13, no. 6,p. 1–18, doi:10.1130/GES01478.1.

4. Karasözen E., Nissen E., Büyükakpınar P., Cambaz M.D., Kahraman M., Ertan E.K., Abgarmi B., Bergman E., Ghods A., Özacar A.A., 2018, The 2017 july 20 Mw 6.6 Bodrum-Kos earthquake illuminates active faulting in the gulf of Gökova, SW Turkey., Geophys. J. Int (2018) 214, 185-199, doi: 10.1093/gji/ggy114

5. Crustal structure across the central segment of the north Anatolian fault zone and its relation with old sutures: new constraints from receiver functions, in prep

6. Pamir, D., Abgarmi, B., Özacar, A.A., "Analysis of Seismic Anisotropy Across Central Anatolia by Shear Wave Splitting" , in prep

Conference Abstracts

1. Abgarmi, B., Ozacar, A.A., Delph, J.R., Beck, S.L., Sandvol, E., Turkelli, N., Kalafat, D., Kahraman, M., Teoman, U., (2014), "Structure of the Crust beneath Central Anatolia: Preliminary Analysis of Teleseismic Receiver Functions". 8th International Symposium on Eastern Mediterranean Geology.

2. Abgarmi, B., Ozacar, A.A., Delph, J.R., Beck, S.L., Sandvol, E., Turkelli, N., Kalafat, D., Kahraman, M., Teoman, U., (2016), The Nature of Central Anatolian Crust and Uppermost Mantle from Teleseismic Receiver Functions: The Role of

Slab Dynamics on Rapid Uplift, AGU Fall meeting, T51A Making the Mediterranean: From Mantle to Surface Processes I Posters

3. Abgarmi, B., Ozacar, A.A., M-Split: A Graphical User Interface to Analyze Multilayered Anisotropy from Shear Wave Splitting, EGU General Assembly, Vienna, Austria, 2017- 11955

4. Abgarmi, B., Delph, J.R., Ozacar, A.A., Beck, S.L., Zandt, G., Crustal structure of the central Anatolia from receiver function analysis, GeoDaze 2016, The University of Arizona, oral presentations, Geophysics session

5. Ozacar, A.A., Abgarmi, B., Delph, J.R., Beck, S.L., Sandvol, E., Turkelli, N., Kalafat, D., Kahraman, M., & Teoman, U., (2015), "Central Anatolian Seismic Network: Initial Analysis of Seismicity and Earth Structure". EGU General Assembly Conference Abstracts 17, 9024.

6. Ozacar, A.A., Abgarmi, B., Delph, J.R., Beck, S.L., Sandvol, E., Turkelli, N., Kalafat, D., Kahraman, M., Teoman, U., & Polat, G., (2014), "CAT Seismic Network: Preliminary Results & Implication on Central Anatolian Tectonics". 8th International Symposium on Eastern Mediterranean Geology.

7. Pamir, Dilekcan; Abgarmi, Bizhan; Arda Özacar, A., "Analysis of Seismic Anisotropy Across Central Anatolia by Shear Wave Splitting" EGU General Assembly 2014, held 27 April - 2 May, 2014 in Vienna, Austria, id.15868

8. Ozacar, A.A., Abgarmi, B., Subsurface signature of North Anatolian Fault Zone and its relation with old sutures: New insight from receiver function analysis. EGU General Assembly, Vienna, Austria, 2017-14630

9. Delph, J., R., Abgarmi, B., Ward, K. M., Beck, S. L., Ozacar, A. A., Zandt, G.,Sandvol E., Turkelli, N. and Kalafat D.,The effects of subduction termination on the continental lithosphere: Linking volcanism, deformation, surface uplift, and slab tearing in central Anatolia, EGU General Assembly, Vienna, Austria, 2017- 1086

10. Tank, S. B., Ozaydin, S., Uslular G., Delph J. R., Abgarmi B., Karas M. and Sandvol E., Preliminary Results of Three-Dimensional Magnetotelluric Imaging at the Vicinity of Nigde Massif, EGU General Assembly, Vienna, Austria, 2017- 6411

11. Darin M., et al., 2017, Geodynamic Evolution of Subduction to Collision to Escape in Central Anatolia From Surface to Mantle - Results From the CD-CAT Project, Geophysical Research Abstracts Vol. 19, EGU2017-18120, EGU General Assembly 2017

12. Akyurek, Z., Binley, A. M., Demir, G., Abgarmi, B., 2017, Water content estimated from point scale to plot scale, American Geophysical Union, Fall Meeting 2017, abstract #H43K-1791

HOBBIES

Computer Technologies, Movies,